

Energy transfer in erbium doped optical waveguides based on silicon

Energy transfer in erbium doped optical waveguides based on silicon
Pieter Geert Kik

ISBN 90-393-2491-3

A digital version of this thesis can be downloaded from <http://www.amolf.nl>
Printed copies can be obtained by request via e-mail to library@amolf.nl or
by addressing the FOM-Institute for Atomic and Molecular Physics,
Kruislaan 407, 1098 SJ Amsterdam, The Netherlands.

Energy transfer in erbium doped optical waveguides based on silicon

Energie overdracht in erbium gedoteerde lichtgeleiders gebaseerd op silicium

(met een samenvatting in het Nederlands)

Proefschrift

Ter verkrijging van de graad van doctor aan de Universiteit Utrecht op gezag van de Rector Magnificus, Prof. Dr. H. O. Voorma, ingevolge het besluit van het College voor Promoties in het openbaar te verdedigen op maandag 18 september 2000 des middags te 12.45 uur

door

Pieter Geert Kik

Geboren op 7 mei 1972 te Zuidelijke IJsselmeerpolders

Promotor: Prof. Dr. A. Polman
Faculteit der Natuur- en Sterrenkunde, Universiteit Utrecht
FOM-Instituut voor Atoom- en Molecuulfysica, Amsterdam



The work described in this thesis was performed at the FOM-Institute for Atomic and Molecular Physics, Kruislaan 407, 1098 SJ Amsterdam, The Netherlands. It is part of the research program of the Foundation for Fundamental Research on Matter (FOM), and was made possible by financial support from the Dutch Organization for the Advancement of Research (NWO), the Dutch Technology Foundation (STW), the Innovative Research Program (IOP) of the Ministry of Economic Affairs, and the SCOOP program of the European Union.

Table of contents

1 General introduction	9
1.1 Fiber optics	9
1.2 Integrated optics	9
1.3 Erbium	10
1.4 This thesis	11
<i>1.4.1 Energy transfer in Er doped Al₂O₃ planar waveguide amplifiers</i>	11
<i>1.4.2 Energy transfer in Er doped silicon</i>	12
<i>1.4.3 Energy transfer in Er and Si nanocrystal doped SiO₂</i>	13

Part I

2 Er doped optical waveguide amplifiers on silicon	17
2.1 Introduction	17
2.2 Principle of operation	18
2.3 Waveguide fabrication	19
2.4 Gain limiting processes and parameters	20
<i>2.4.1 Erbium concentration and solubility</i>	20
<i>2.4.2 Waveguide loss</i>	20
<i>2.4.3 Mode overlap</i>	21
<i>2.4.4 Pump wavelength</i>	21
<i>2.4.5 Pump absorption</i>	21
<i>2.4.6 Co-operative upconversion</i>	22
<i>2.4.7 Excitation migration and non-radiative quenching</i>	22
<i>2.4.8 Excited state absorption</i>	23
2.5 The state of the art in Er doped planar amplifiers	24
2.6 Outlook	27

3 Co-operative upconversion as the gain limiting factor in Er doped miniature Al₂O₃ optical waveguide amplifiers	31
3.1 Introduction	31
3.2 Experiment	32
3.3 Results and discussion	35
3.4 Conclusions	41

Part II

4 Excitation and de-excitation of Er³⁺ in crystalline silicon	45
4.1 Introduction	45
4.2 Experiment	47
4.3 Results and discussion	48
4.4 Conclusions	52
5 Energy backtransfer and infrared photoresponse in Er doped silicon <i>p-n</i> diodes	55
5.1 Introduction	56
5.2 Experiment	58
5.3 Results	59
5.4 Energy transfer processes	60
5.4.1 <i>Optical absorption and emission ($\sigma_{1.535}$)</i>	60
5.4.2 <i>Auger quenching ($W_{A,e}$, $W_{A,h}$)</i>	62
5.4.3 <i>Er excitation and backtransfer (W_E, W_{BT})</i>	62
5.4.4 <i>Electron-hole pair trapping and dissociation (W_D, W_T)</i>	63
5.4.5 <i>Carrier recombination at the Er related trap level</i>	63
5.5 Comparison between model and experiment	64
5.5.1 <i>Photoluminescence rate equations</i>	64
5.5.2 <i>Photoresponse rate equations</i>	64
5.5.3 <i>Model calculations</i>	64
5.6 Implications for solar cell and infrared detector design	67
5.7 Conclusions	67

6 Quantum efficiency of an Er doped waveguide detector in silicon operating at 1.54 μm	69
6.1 Introduction	69
6.2 Device layout	70
6.3 Contributions to the external quantum efficiency	71
6.3.1 <i>Absorption by the metal contacts</i>	71
6.3.2 <i>Optical absorption by Er</i>	72
6.3.3 <i>Free carrier absorption</i>	73
6.4 Numerical calculations	73
6.5 Preliminary measurements	75
6.6 Device optimization	77
6.7 Conclusions	78

Part III

7 Strong exciton-erbium coupling in Si nanocrystal doped SiO₂	81
7.1 Introduction	81
7.2 Experiment	83
7.3 Results and discussion	83
7.4 Conclusions	87
8 Exciton-erbium interactions in Si nanocrystal doped SiO₂	89
8.1 Introduction	89
8.2 Experiment	90
8.3 Results and discussion	92
8.3.1 <i>Photoluminescence vs. Er concentration</i>	92
8.3.2 <i>Internal quantum efficiency vs. Er concentration</i>	93
8.3.3 <i>Nanocrystal luminescence lifetime vs. Er concentration</i>	94
8.3.4 <i>Er luminescence intensity vs. pump power</i>	97
8.3.5 <i>The Er excitation and decay rate vs. Er concentration</i>	98
8.3.6 <i>Models describing the Er concentration limit</i>	100
8.3.7 <i>The Er local environment</i>	101

8.3.8 <i>Device implications</i>	102
8.4 Conclusions	103
9 Gain limiting processes in Er doped Si nanocrystal waveguides in SiO₂	105
9.1 Introduction	105
9.2 Experiment	106
9.3 Results and discussion	108
9.4 Conclusions	111
Summary	113
Samenvatting	115
Dankwoord	117
Curriculum Vitae	118
List of publications	119

Chapter 1

General introduction

1.1 Fiber optics

The rapid growth in the use of distributed information systems such as the Internet stimulates the demand for high data transmission rates. Currently, the highest data rates are achieved using silica glass fiber. The information is transmitted as a series of light pulses that travel through the fiber at approximately 200,000 km/s. Due to the high frequency of light, the amount of data that can be transmitted is tremendous: the 2nd generation transatlantic fiber transmission link that is being installed supports transmission of 4×500 gigabits per second over four glass fiber pairs.¹ This is still far from the fundamental limit to the transfer rate, and future systems are expected to reach data transfer rates of several terabits (10^{12} bits) per second in a single fiber.

Glass fiber contains a high refractive index core, surrounded by a lower refractive index cladding layer. This structure functions as an optical waveguide: light is confined in the fiber core by total internal reflection, allowing the transmission of optical signals over large distances. Long distance data transfer also requires high transparency. In the wavelength region of optimum transmission of glass fiber, occurring around 1.5 μm , modern fibers exhibit losses as low as 5% per kilometer (0.2 dB/km). Nevertheless, for transmission over large distances the optical signal needs to be amplified at regular intervals in order to maintain sufficient light intensity. This is done using erbium doped fiber amplifiers² (EDFAs), that operate at a wavelength of 1.5 μm . This wavelength is currently one of the standard wavelengths used in optical telecommunication.

1.2 Integrated optics

Fiber optic networks contain several optical components, such as lasers, modulators, multiplexers, splitters, amplifiers, and detectors, connected by glass fiber. A significant reduction in system size and cost can be achieved by the development of integrated optics, in which several optical functions are performed on a single

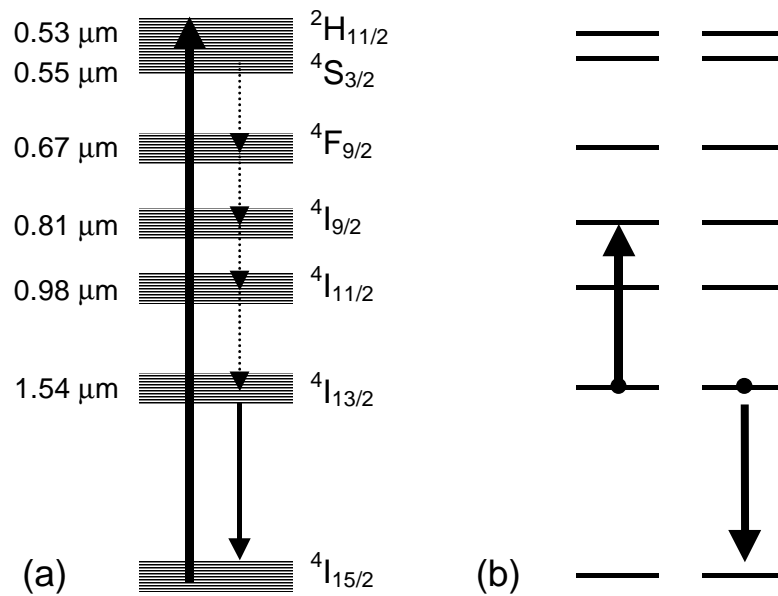


Figure 1.1 (a) Schematic representation of the Stark-split Er^{3+} energy levels, showing excitation at $0.514 \mu\text{m}$, followed by rapid non-radiative relaxation and emission at $1.54 \mu\text{m}$. (b) Co-operative upconversion from the Er^{3+} first excited state, bringing one ion in the ${}^4\text{I}_{9/2}$ state. This effect has a strong influence on the amplification performance of highly Er doped planar waveguide amplifiers (Chapters 2 and 3).

substrate. In integrated optical circuits, light is directed to different optical components through planar optical waveguides. These waveguides can be fabricated in a thin layer of a high refractive index material using lithographic techniques, allowing for mass production of compact optical circuits. Silicon is an ideal substrate for integrated optical circuits, because of the availability of low cost silicon wafers with excellent surface quality. Ultimately, one would like to combine the functionality of silicon electronics with optical data transmission, to yield silicon opto-electronic integrated circuits (OEICs) operating at $1.5 \mu\text{m}$. There are two approaches to achieve such silicon OEICs, namely *hybrid* and *monolithic* integration. The hybrid approach involves the growth optically active materials such as III-V semiconductors on a silicon surface. Monolithic silicon OEICs can be fabricated by doping silicon waveguides with optically active elements, such as erbium.

1.3 Erbium

Erbium is a rare earth element belonging to the group of the Lanthanides. When embedded in a solid, erbium generally assumes the trivalent Er^{3+} state, which has an

electronic configuration $[\text{Xe}]-4f^{11}$. The Er^{3+} ion has an incompletely filled 4f-shell, allowing for different electronic configurations with different energies due to spin-spin and spin-orbit interactions.³ Radiative transitions between most of these energy levels are parity forbidden for free Er^{3+} ions. When Er is incorporated in a solid however, the surrounding material perturbs the 4f wave functions. This has two important consequences. Firstly, the host material can introduce odd-parity character in the Er 4f wave functions, making radiative transitions weakly allowed. Secondly, the host material causes Stark-splitting of the different energy levels, which results in a broadening of the optical transitions. Figure 1.1(a) shows a schematic level diagram of the Stark-split Er^{3+} energy levels, labeled using Russell-Saunders notation.

Since radiative transitions in Er^{3+} are only weakly allowed, the cross sections for optical excitation and stimulated emission are quite small, typically on the order of 10^{-21} cm^2 , and the radiative lifetimes of the excited states are long, up to several milliseconds. When Er is excited in one of its higher lying levels (see Fig. 1.1(a)) it rapidly relaxes to lower energy levels via multi-phonon emission. This results in typical excited state lifetimes ranging from 1 ns to 100 μs . The transition from the first excited state ($^4\text{I}_{13/2}$) to the ground state ($^4\text{I}_{15/2}$) is an exception to this rule. Due to the large transition energy (0.8 eV) multi-phonon emission is unlikely, resulting in lifetimes up to ~ 20 ms depending on host material, and efficient emission at 1.54 μm .

1.4 This thesis

1.4.1 Energy transfer in Er doped Al_2O_3 planar waveguide amplifiers

The first part of this thesis describes energy transfer processes that take place in Er doped planar waveguide amplifiers operating at 1.54 μm . Optical amplification can be achieved in an Er doped optical waveguide by exciting the Er into the first excited state, for example by optical pumping at 1.48 μm or 0.98 μm . If population inversion is reached, optical amplification can be achieved by stimulated emission at 1.54 μm .

Chapter 2 describes the processes that determine the performance of Er doped waveguide amplifiers. Firstly, due to the small optical absorption cross sections of Er^{3+} , large pump fluxes are required to achieve population inversion. In miniature waveguides with a high refractive index, these large fluxes can be achieved at relatively low pump power. Secondly, due the small emission cross section of Er at 1.54 μm , high Er concentrations on the order of 10^{19} - 10^{20} Er/cm^3 are required to achieve appreciable gain over a waveguide length of a few cm. At these concentrations excited Er ions can exchange energy, leading to several undesirable processes. One of these is co-operative upconversion, in which one ion is excited into a higher energy state, while a neighboring ion returns to the ground state (Fig. 1.1(b)). This decreases the population in the first excited state, and consequently

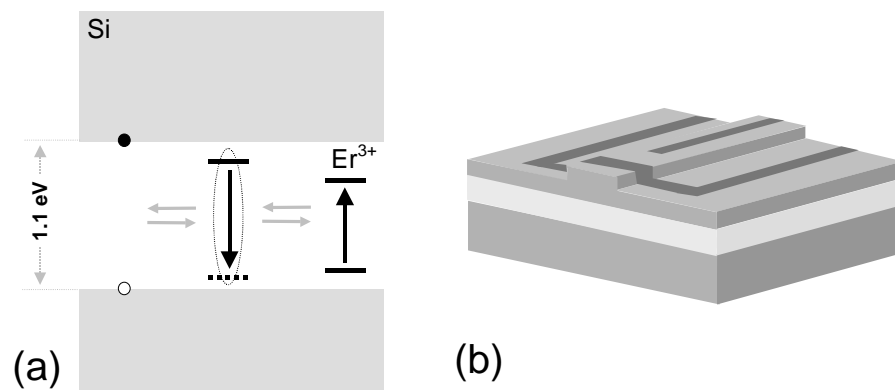


Figure 1.2 (a) A simplified Si band structure diagram, showing the 1.1 eV Si bandgap, the lowest two Er³⁺ energy levels, and energy transfer between the Si electronic system and Er³⁺ via an Er related defect level in the Si bandgap (Chapters 4 and 5). (b) Sketch of an Er doped waveguide detector in Si, that is based on optical Er excitation at 1.54 μm followed by energy transfer to the silicon electronic system (Chapter 6).

lowers the gain that can be achieved at a given pump power. To compensate for non-radiative effects occurring at high Er concentration, Er doped planar waveguide amplifiers are operated at a relatively high pump flux. In Chapter 2 it is shown that this induces excited state absorption, *i.e.* the absorption of pump photons by excited Er. This effect sets a limit to the waveguide length that can be used. Finally, a review of the most successful waveguide amplifiers and their characteristics is presented.

One of the more successful waveguide amplifier materials is Er doped Al₂O₃. Aluminum oxide has been thoroughly studied as a waveguide material, and miniature planar waveguides can be fabricated with low optical loss at 1.54 μm . By doping Al₂O₃ waveguides with Er using ion implantation, an optical waveguide amplifier has been fabricated, with a net optical gain of 2.3 dB at 1.54 μm in a 4 cm long waveguide.⁴ Ion implantation however is a rather costly and time-consuming process. In Chapter 3, an Er implanted Al₂O₃ waveguide amplifier is compared with a similar amplifier fabricated by the more economical co-sputtering process. It is shown that co-sputtering generates a highly inhomogeneous atomic scale distribution of the Er ions, resulting in strong co-operative upconversion at relatively low Er concentration.

1.4.2 Energy transfer in Er doped silicon

The second part of this thesis describes energy transfer processes occurring in Er doped silicon. In silicon, Er can be excited by energy transfer from electron-hole pairs trapped at an Er related defect level in the Si bandgap (Fig 1.2(a)). It is observed that the Er luminescence intensity decreases strongly as the temperature is

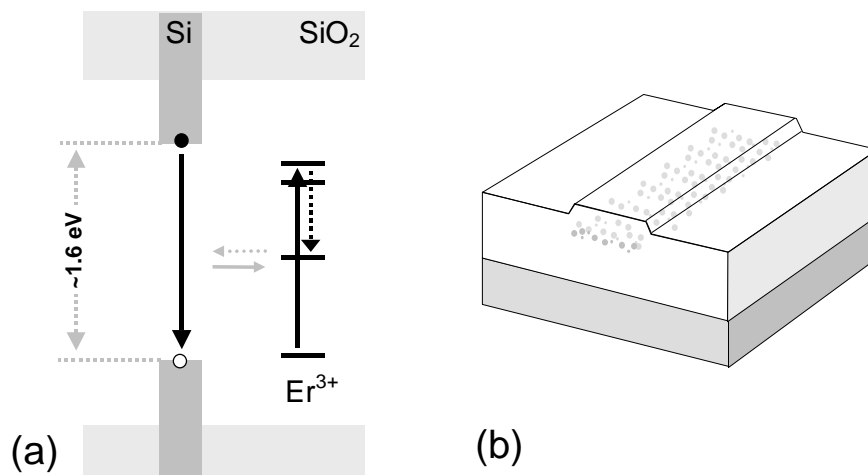


Figure 1.3 (a) Schematic band structure of Er^{3+} and Si nanocrystal doped SiO_2 , showing the recombination of a quantum confined electron-hole pair and simultaneous Er excitation (Chapters 7 and 8). This process can be used in an Er doped Si nanocrystal sensitized waveguide amplifier. (b) Sketch of an Er doped Si nanocrystal waveguide. The index contrast required for optical mode confinement is induced by the Si nanocrystals (Chapter 9).

increased. By analyzing temperature dependent measurements of the Er luminescence intensity and lifetime, it is shown in Chapter 4 that the intensity decrease is mainly due to a non-radiative energy backtransfer process, in which an excited Er ion generates a trapped electron-hole pair.

When the Er is located in a Si p - n junction, the energy backtransfer process can generate a photocurrent under illumination with $1.54 \mu\text{m}$ light. In Chapter 5 the temperature dependent photocurrent and photoluminescence of an Er doped p - n junction are investigated. It is shown that at room temperature energy backtransfer followed by electron-hole pair dissociation occurs with a quantum efficiency of 70%. This enables the fabrication of an Er doped photo-detector sensitive at $1.54 \mu\text{m}$ in a Si waveguide. Chapter 6 discusses the efficiency of an Er doped p - n junction waveguide detector in Si operating at $1.54 \mu\text{m}$. An example of such a waveguide detector is shown in Fig. 1.2(b). Using optical mode calculations and the parameters determined in Chapter 5 it is shown that such a 4 cm long waveguide detector in Si can reach an external quantum efficiency of 10^{-3} , and several approaches for further improvement are discussed.

1.4.3 Energy transfer in Er and Si nanocrystal doped SiO_2

The final part of this thesis investigates the energy transfer processes that occur in an Er doped Si/ SiO_2 nanocomposite material. It consists of small Si crystallites in an SiO_2 matrix. Silicon nanocrystals have a larger bandgap than bulk Si due to

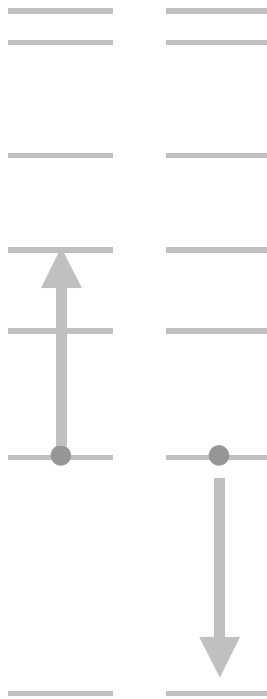
quantum confinement, and can efficiently absorb visible light, resulting in the generation of quantum confined electron-hole pairs. In Chapter 7 it is shown that optically generated electron-hole pairs in Si nanocrystals can recombine and transfer energy to Er (see Fig. 1.3(a)). The transfer is found occur within 1 μ s, and the transfer quantum efficiency is found to be larger than 55%. It is shown that the resulting effective Er absorption cross section can be five orders of magnitude larger than that for direct optical excitation. Furthermore, no temperature quenching of the Er luminescence occurs in Si nanocrystal doped SiO₂.

The efficient excitation and the absence of backtransfer make Si nanocrystals an interesting candidate for an Er sensitizer that can reduce the pump power needed to achieve population inversion in a waveguide amplifier. Chapter 8 evaluates the possibility of fabricating a Si nanocrystal sensitized waveguide amplifier in SiO₂, and focuses on the energy transfer processes occurring at high Er concentration and high pump power. It is shown that a single nanocrystal can excite only \sim 1 Er ion, and that an optical gain of 0.6 dB/cm may be achieved in a nanocrystal sensitized waveguide amplifier. An example of such a waveguide amplifier is shown in Fig. 1.3(b). The refractive index increase induced by the Si nanocrystals generates the index contrast necessary for optical confinement. Additionally, the broad absorption band of the Si nanocrystals enables the use of a broad band light source as a pump for an Er doped nanocrystal waveguide amplifier. In Chapter 9 transmission measurements on such a nanocrystal waveguide structure are presented, and it is concluded that optical gain at 1.54 μ m may be achieved in a 1 cm long waveguide amplifier using a pump power as low as 1 mW.

References

- ¹ N. S. Bergano, *Opt. Photon. News* **11**, 21 (2000)
- ² E. Desurvire, *Erbium-Doped Fiber Amplifiers: Principles and Applications* (John Wiley & Sons, 1994)
- ³ S. Hufner, *Optical Spectra of Transparent Rare-Earth Compounds* (Academic, New York, 1978)
- ⁴ G. N. van den Hoven, *Erbium-doped photonic materials*, PhD thesis, Utrecht University, The Netherlands (1996)

Part I



Chapter 2

Er doped optical waveguide amplifiers on silicon

2.1 Introduction

Thin film integrated optics is becoming more and more important in optical communications technology. The technology for the fabrication of passive devices such as planar optical waveguides, splitters, and multiplexers is now quite well developed, and devices based on this technology are now commercially available. One next step to further improve this technology is to develop optical amplifiers that can be integrated with these devices.^{1,2} Such amplifiers can serve to compensate for the losses in e.g. splitters or other components, and can also serve as preamplifiers for active devices such as detectors.

In optical fiber technology, erbium doped fiber amplifiers^{3,4} are now used in long distance fiber communications links. They use an optical transition in Er^{3+} at a wavelength of 1.54 μm for signal amplification, and their success has set a standard of optical communication at this wavelength. Using the same concept of Er doping, planar waveguide amplifiers are now being developed. For these devices silicon is often used as a substrate, so that opto-electronic integration with other devices in or on Si (electrical devices, or Si based light sources, detectors, modulators) may become possible.

At first sight, it may seem straightforward to translate the concept of a fiber amplifier to that of an integrated planar waveguide. However, in scaling down the device dimensions from the long fiber length (typically 40 m) to the small device dimensions of an opto-electronic integrated circuit, the Er concentration has to be increased to achieve the same amount of optical gain. As it turns out, physical processes that were unimportant in fiber technology become important in planar amplifiers.

In the past few years, several Er doped planar optical waveguide materials have been explored, and in some cases optical gain has been achieved. The challenge today is to understand the processes that limit the gain, and to find materials and structures in which these processes have a minimum effect. This

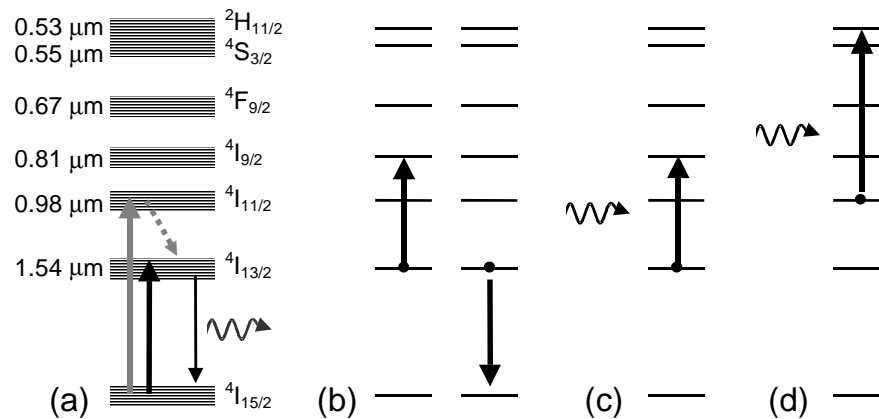


Figure 2.1. Schematic representation of the Er³⁺ intra 4f energy levels. Figure (a) shows the 1.54 μm transition, and the upward arrows indicate excitation using 1.48 μm pump light and 0.98 μm pump light respectively. Figure (b) show the process of co-operative upconversion, where interaction between two excited Er³⁺ ions leads to the population of higher lying energy levels. Figure (c) and (d) show the process of excited state absorption of a 1.48 μm or a 0.98 μm pump photon respectively.

chapter discusses the most important of these processes, and gives an overview of the planar optical amplifiers obtained on silicon to date.

2.2 Principle of operation

In most materials, erbium assumes the trivalent charge state (Er³⁺) with an electronic configuration of [Xe]·4f¹¹. Spin-spin and spin-orbit coupling in the incompletely filled 4f shell give rise to a number of energy levels as depicted in Fig. 2.1. Each degenerate level is Stark-split into a manifold of levels, due to the presence of the host material. The transition from the first excited state (4I_{13/2}) to the ground state (4I_{15/2}) occurs at a wavelength of approximately 1.54 μm. The emission wavelength is relatively insensitive to the host material, because the 4f shell is shielded from its surroundings by the filled 5s and 5p shells.

In an optical amplifier, erbium is incorporated in the core of an optical waveguide. Using an external laser, the Er is excited into one of its higher lying energy levels. Erbium can be pumped directly into the first excited manifold using a 1.48 μm diode laser, or via one of the higher lying absorption lines, for example using a 0.98 μm diode laser. In the latter case, the Er relaxes rapidly into the first excited state. When sufficient pump power is applied, this leads to population inversion between the first excited state and the ground state. A 1.54 μm signal travelling through the Er doped waveguide will then induce stimulated emission from the first excited state to the ground state, resulting in signal amplification.

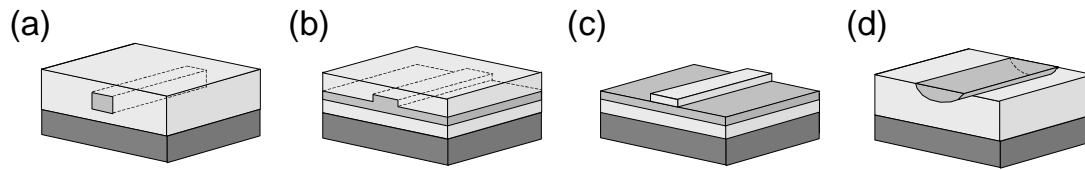


Figure 2.2. Schematic representation of waveguide structures that may be used to fabricate a planar optical waveguide amplifier. Light is confined in the high refractive index waveguide core (dark grey) by total internal reflection. The Er doped core material is embedded in a low refractive index cladding layer (light grey). The device rests on a silicon substrate (dark grey). Indicated are (a) a channel waveguide, (b) a ridge waveguide, (c) a strip loaded waveguide, and (d) a diffused waveguide.

2.3 Waveguide fabrication

In order to fabricate an Er doped planar waveguide amplifier on Si, one needs to use a material that a) is transparent to the wavelength used to excite the Er, and to the signal wavelength, b) can dissolve large amounts of Er that is optically active (i.e. luminescent at high quantum efficiency), and, c) can be made into a channel waveguide using a technology that is compatible with standard Si processing. A number of waveguide structures can be used to realize a planar optical waveguide amplifier, each with their own specific advantages. In all of these structures, light is guided in a high refractive index material (the waveguide core), surrounded by a lower index material (the cladding).

Figure 2.2 schematically shows cross sections of different waveguide structures that can be used. A channel waveguide (Fig. 2.2(a)) can be formed by depositing a high index layer on a low index cladding, followed by standard lithography to define a line. The lithography is usually followed by the deposition of a low index top cladding. Another way of forming such a channel waveguide is by ion implantation. In this case the refractive index contrast is achieved by a change in chemical composition (see e.g. Chapter 9 of this thesis), or by ion irradiation induced damage.⁵ A variation on the channel waveguide is the ridge waveguide (Fig. 2.2(b)), in which the high refractive index core layer is not fully etched back. This lowers the in-plane index contrast, and therefore in general decreases the scattering loss. Optical mode confinement can also be obtained by putting a strip of cladding material on a planar core layer, resulting in a strip loaded waveguide (Fig. 2.2(c)). This type of structure requires no etching of the Er doped core layer, thus leaving the Er unaffected by the waveguide fabrication process. Another structure is the diffused waveguide, formed by in-diffusing an element that

raises the refractive index (Fig. 2.2(d)). Similarly, index contrast can be achieved using an ion exchange process,⁶ in which ions in the core material are exchanged for ions from the salt melt in which the waveguide is immersed. The resulting low index contrast waveguides have low losses, due to the smoothly graded refractive index profiles.

As the light guiding in all these structures relies on total internal reflection, waveguide bends cannot be made infinitely sharp. The index contrast between core and cladding layers determines the minimum bending radius of a waveguide. For example, silica waveguides with a small refractive index contrast ($\Delta n \approx 0.01$) have a minimum bending radius in the centimeter range. Therefore long silica based waveguide amplifiers sometimes require a 4" wafer as a substrate.⁷ For a high contrast waveguide, e.g. an Al_2O_3 core with an SiO_2 cladding ($\Delta n \approx 0.20$), the bending radius can be as low as $50 \mu\text{m}$.⁸ For such a system, it has been shown⁹ that a 3 cm long waveguide can be 'rolled-up' on an area of only 1 mm^2 . Consequently, if high integration densities are required, the core material must have a high refractive index. This high index contrast also results in smaller optical mode dimensions. Therefore, high pump intensities can be achieved at relatively low pump powers, decreasing the pump threshold for amplification.

2.4 Gain limiting processes and parameters

2.4.1 Erbium concentration and solubility

The most important parameter for amplification is the concentration of Er^{3+} ions that are optically active (i.e. that have high quantum efficiency). The maximum gain per unit length is determined by the product of the cross section for stimulated emission σ_{em} and the active Er concentration. Since typical values for σ_{em} are in the 10^{-21} - 10^{-20} cm^2 range, concentrations of 10^{19} - 10^{20} Er/cm^3 are required to achieve a reasonable gain over a length of a few centimeters. Therefore, the host material must have a high Er solubility.

Silica based glasses have turned out to be a practical host material, as the composition can be tuned continuously for optimum Er solubility using various available network modifiers. It has been shown that by incorporating for example phosphorous in the glass matrix, the solubility of Er may be increased.¹⁰ Aside from glasses, ceramic materials with a high refractive index, such as Al_2O_3 and Y_2O_3 , are interesting hosts. As their crystal structure is similar to that of Er_2O_3 , they show a high Er solubility.¹¹⁻¹³

2.4.2 Waveguide loss

A next important parameter is the waveguide loss, determined by absorption and scattering of guided light. To achieve net amplification, the signal loss due to these intrinsic waveguide losses first has to be compensated for by stimulated emission. Moreover, at the Er concentrations needed to compensate for a typical waveguide

loss of 0.1-1 dB/cm, Er-Er interactions reduce the gain, as will be discussed below. Pump light is also scattered as it travels through the waveguide, lowering the pumping efficiency. Thus, minimizing waveguide loss is crucial for good amplifier performance.

Scattering can be induced by irregularities in the refractive index on a length scale of the order of the wavelength. One notorious origin of scattering is waveguide roughness, caused for example by an etching step in the fabrication process. This effect becomes more pronounced when high index contrast structures are used.

2.4.3 Mode overlap

For optimum gain, both signal light and pump light should be confined in such a way that optimum overlap between the optical modes and the Er concentration profile is achieved. For low refractive index contrast materials, a significant fraction of the optical mode travels through the undoped cladding material, resulting in a lower gain per unit length.

2.4.4 Pump wavelength

Erbium doped waveguide amplifiers are either pumped at 0.98 μm ($^4\text{I}_{11/2}$ level) or 1.48 μm ($^4\text{I}_{13/2}$ level). Pumping high into the first excited state of Er using a 1.48 μm laser results in a quasi three-level system, with a good overlap of the signal mode at 1.54 μm with the pump mode, due to similar mode sizes at these wavelengths. Furthermore, scattering losses of waveguides usually increase for shorter wavelengths, favoring a long wavelength pump laser. However, due to the overlap of the 1.48 μm pump wavelength with the $^4\text{I}_{13/2} \rightarrow ^4\text{I}_{15/2}$ emission spectrum, the pump also induces stimulated emission at 1.48 μm . This effect puts an upper limit to the degree of population inversion that can be obtained.

Stimulated emission by the pump is much weaker when a pump wavelength of 0.98 μm is used. In this case the excited Er rapidly relaxes non-radiatively into the first excited state, precluding stimulated emission by the pump from the 0.98 μm level. However, the internal relaxation also reduces the pumping efficiency, as the relaxation energy (about 0.45 eV per excitation event) is transformed into heat. In general, the absorption cross section for the 0.98 μm level is smaller than that of the 1.48 μm level, resulting in an increased threshold power.

2.4.5 Pump absorption

Due to the relatively small absorption cross section of the Er energy levels, rather high pump intensities are required to achieve population inversion. This problem can be overcome by introducing a species with a large optical absorption cross section that can transfer energy to the Er. One example of such a sensitizer is the rare earth ion Yb^{3+} . Ytterbium has a large absorption cross section around 0.98 μm ,

and can transfer its energy non-radiatively to an Er ion that is then excited into the $^4I_{11/2}$ level.¹⁴ As the Yb absorption band extends all the way from 0.85 μm to 1.02 μm , it can be pumped over a broad spectral range. In polymer waveguides, Er can be incorporated in an organic complex. This complex absorbs in a broad spectral range, and can transfer its energy to Er.¹⁵ Additionally, specially designed sensitizer molecules can be attached to the complex to further increase the absorption efficiency.

A new approach is to use Si nanocrystals as sensitizer. Optical excitation of Si nanocrystals in Er doped SiO_2 has been shown to result in efficient Er excitation (see Chapters 7-9 of this thesis). The broad absorption band of the Si nanocrystals makes it possible to excite Er in a waveguide amplifier using a broad band light source.

2.4.6 Co-operative upconversion

At high Er concentrations, interaction between Er ions is an important gain limiting effect. One of such processes is co-operative upconversion.^{1,16,17} In this process, an excited Er ion de-excites by transferring its energy to a neighboring excited ion, promoting it into the $^4I_{9/2}$ level (Fig. 2.1(b)). This lowers the amount of excited Er, or conversely, increases the pump power needed to obtain a certain degree of inversion. Co-operative upconversion is possible due to the presence of a resonant level at twice the energy of the first excited state. The co-operative upconversion coefficient depends on the host material, as it is related to the exact energy level positions, cross sections, the dielectric constant, and the typical phonon energy of the host material. In practice, co-operative upconversion is an important gain limiting effect for Er concentrations above 10^{19} - 10^{20} Er/cm^3 .

The effect of co-operative upconversion not only depends on the average Er concentration, but also on the microscopic distribution of the Er ions in the host material. The upconversion coefficient can vary by orders of magnitude in the same host material, as will be shown in Chapter 3. In order to fabricate an efficient amplifier, the fabrication method should be optimized to obtain an homogeneous distribution of Er ions. Although upconversion is an unwanted effect for 1.54 μm signal amplifiers, it may be used advantageously for the fabrication of upconversion lasers, operating in e.g. the green.

2.4.7 Excitation migration and non-radiative quenching

An excited Er ion can transfer its energy to a nearby, unexcited Er ion. This excitation migration¹⁸ does not necessarily reduce the Er population density, but can become detrimental to the gain if some Er ions are strongly coupled to non-radiative quenching sites. For example, the second overtone of the OH stretch vibration is resonant with the transition from the first excited state to the ground state of Er. Indeed, it has been shown that the Er luminescence lifetime correlates with the water content in silica glasses.^{19,20} The effect of quenching sites becomes more

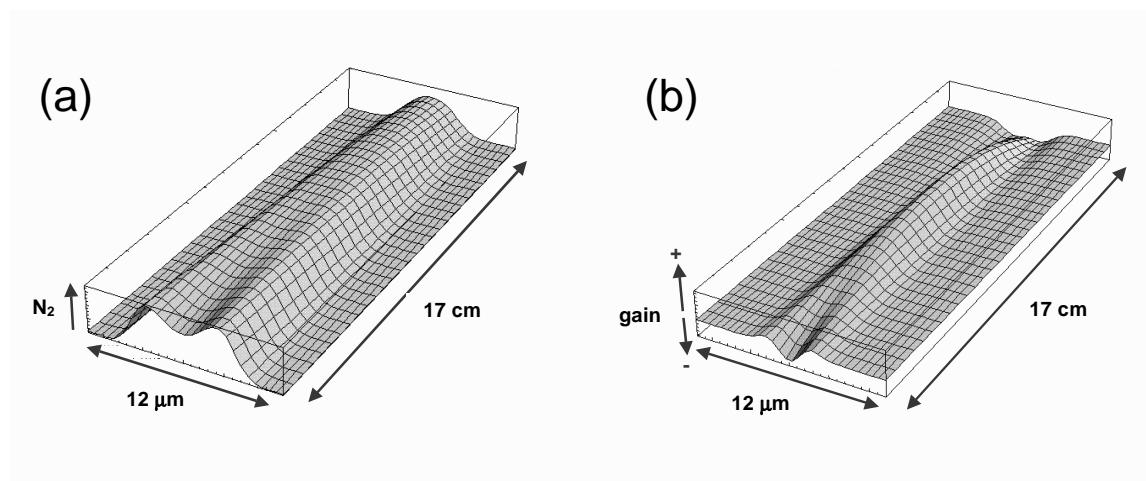


Figure 2.3. (a) Fraction of Er in the first excited state along a $2\ \mu\text{m}$ wide, $17\ \text{cm}$ long ridge waveguide, calculated in the plane of the waveguide. The waveguide is pumped with $100\ \text{mW}$ at $1.48\ \mu\text{m}$. The maximum fraction of excited Er that is reached is 68% . The dip near the front facet is caused by excited state absorption. (b) Differential gain calculated from the excited Er distribution and the optical mode of the signal.

pronounced at high Er concentrations, resulting in a reduced pumping efficiency. Therefore, care must be taken to synthesize Er doped materials that are free of impurities or defects that couple to Er.

2.4.8 Excited state absorption

Another gain limiting effect is formed by excited state absorption (ESA). In this process, an excited Er ion absorbs a signal photon (Fig. 2.1(c)), or a pump photon (Fig. 2.1(c) and Fig. 2.1(d)), bringing it in a higher excited state. As this effect involves both signal and pump photons, it affects both the maximum gain and the pump efficiency. The effect becomes important for the gain when the higher lying states have an appreciable lifetime, leading to the buildup of significant steady state population in the higher lying energy levels, which do not take part in the amplification. As ESA depends on the pump intensity, it becomes important when high pump powers are required, for example to compensate for co-operative upconversion processes, or de-excitation of the Er by strong signals.

The effect of ESA on amplifier performance is illustrated in Fig. 2.3(a). It shows the fraction of excited Er ions in a $17\ \text{cm}$ long Er doped Al_2O_3 waveguide, calculated in the plane of the waveguide as the structure is pumped with $100\ \text{mW}$ at $1.48\ \mu\text{m}$. The Er doped waveguide core consists of a $2\ \mu\text{m}$ wide, $520\ \text{nm}$ thick ridge, with a remaining thickness on the sides of $260\ \text{nm}$ (see Fig. 2.2(b)). The optical modes are centered in the ridge, but also extend into the Er doped sides,

causing excitation outside of the waveguide core. The calculation takes into account the measured upconversion coefficient¹⁶ and Er absorption and emission cross sections,²¹ as well as the three dimensional 1.48 μm pump and 1.54 μm signal mode distributions. The effect of ESA is seen as a dip in the fraction of Er in the first excited state in the region where the pump power is highest (in the center of the guide near the entrance facet). The effect on the differential signal gain across the guide is shown in Fig. 2.3(b). It shows that at a pump power of 100 mW, ESA causes net signal loss. As the pump power decreases along the waveguide, the effect of ESA decreases, and initially the differential gain along the length of the waveguide increases. Absorption (by Er and the waveguide structure) and scattering lead to a gradual decrease of pump power along the waveguide, and near the end of the waveguide the pump power becomes too low to obtain a positive differential gain. The existence of an upper limit on the pump power shows that ESA puts a maximum to the length that can be used for a single-end pumped waveguide.

2.5 The state of the art in Er doped planar amplifiers

Although many research groups are studying Er doped optical waveguide materials, only a very limited number of groups has fabricated actual devices. Table I lists the most successful Er doped waveguide amplifiers on silicon that have been fabricated to date. In all cases, the waveguide materials were deposited on an oxidized silicon substrate.

A 43 cm long planar waveguide amplifier on silicon developed by Hattori *et al.* at *NTT Opto-electronics Laboratories* (Japan), contains a phosphorous doped silica based glass as a core material.^{7,22} The waveguides were fabricated by flame hydrolysis deposition, followed by reactive ion etching to form the ridge or channel waveguide. The amplifier shows an internal gain of 27 dB using a 0.98 μm pump power of 268 mW. A low Er concentration²³ of $\sim 4 \times 10^{19}$ Er/cm³ (0.45 wt.%) was used, and was sufficient to achieve net gain, because the waveguide loss in this material is very low (0.15 dB/cm). As a result of this low waveguide loss, it is relatively easy to keep the pump intensity above threshold over a large distance along the waveguide, thus allowing for a large total gain. The combination of the large length and the low index contrast however, cause that a large surface area is needed to support the device.

At *Lucent Technologies / Bell Labs* (USA), Shmulovitz *et al.* fabricated a 6 cm long Er doped soda lime silicate glass based waveguide amplifier using radio frequency sputtering.^{24,25} A ridge or channel waveguide was formed using ion beam etching. A fiber-to-fiber gain of 4.5 dB was measured at 80 mW of 0.98 μm pump light. The low background loss in this glass (0.1 dB/cm) allows for the use of a relatively low Er concentration (7×10^{19} Er/cm³), reducing the effect of co-operative upconversion.

A 4 cm long Er doped Al₂O₃ waveguide amplifier on Si was developed by van den Hoven *et al.*⁹ The Al₂O₃ was deposited using RF sputtering, and doped with Er

using ion implantation. Argon beam etching was applied to create a ridge waveguide. A total internal gain of 2.3 dB was measured at a coupled pump power of 9 mW at 1.48 μm .⁹ The pump threshold of this device is only 3 mW, which is due to the high mode confinement in the high index Al_2O_3 core ($n=1.64$). As a result of this high index contrast, 3 cm interaction length could be fitted on an area of only 1 mm^2 . Up to now, this is the only demonstration of a miniature planar optical waveguide amplifier on Si.

Due to the high Er solubility in Al_2O_3 , concentrations of optically active Er up to 3×10^{21} Er/cm^3 (3 at.%) could be incorporated in this material.¹¹ However, at such high concentrations, excitation migration and co-operative upconversion strongly decrease the steady state Er population. It was found that optimum amplifier performance was achieved at 2.7×10^{20} Er/cm^3 .

At *GeeO* (France), Barbier *et al.* developed a waveguide amplifier on Si showing a fiber-to-fiber gain of 16.5 dB over a length of 9 cm when pumped with 200 mW at 0.98 μm .^{26,27} This was measured in an Er-Yb codoped phosphate glass, in which a channel waveguide was formed using a two step ion exchange process. The high gain is due to the high concentration²³ of $\sim 1.6 \times 10^{21}$ Er/cm^3 (2 wt.%) that was dissolved in the phosphate glass. Pumping of the Er is achieved via Yb^{3+} , resulting in a threshold pump power around 25 mW. Net gain was measured for wavelengths ranging from 1.52 μm to 1.57 μm , showing the potential of Er doped planar waveguide amplifiers as broadband optical amplifiers.

Ref. (<i>et. al</i>)	Hattori ²²	Shmulovitz ²⁴	van den Hoven ⁹	Barbier ²⁶	van Weerden ²⁸	Yan ²⁹
date published	5-94	4-96	4-96	2-97	4-97	11-97
waveguide core composition	P-doped SiO_2	soda-lime silicate glass	Al_2O_3	Yb co-doped phosphate glass	Y_2O_3	$\text{P}_2\text{O}_5/\text{Al}_2\text{O}_3$ Na_2O La_2O_3
internal gain (dB)	27	~ 6.5	2.3	> 16.5	6.0	4.1
Er concentration (10^{20} cm^{-3})	~ 0.4 ²³	0.7	2.7	~ 16 ²³	1.3	5.3
length (cm)	47.7	6	4	9	4.3	1
gain / length (dB/cm)	0.6	1.1	0.6	> 1.8	1.4	4.1
pump power (mW) *=inside waveguide	264	80	9*	200	12*	21*
pump wavelength (μm)	0.980	0.980	1.480	0.983	1.480	0.980
waveguide geometry	ridge or channel	ridge or channel	ridge	channel	ridge	strip
core index of refraction	~ 1.46	~ 1.49	1.64	-	1.9	1.53
waveguide loss (dB/cm)	0.15 ⁷	0.1	0.35	~ 0.1	0.8	0.9

Table 2.1. Characteristics of Er doped planar optical waveguide amplifiers operating at 1.54 μm that have been fabricated on silicon to date.

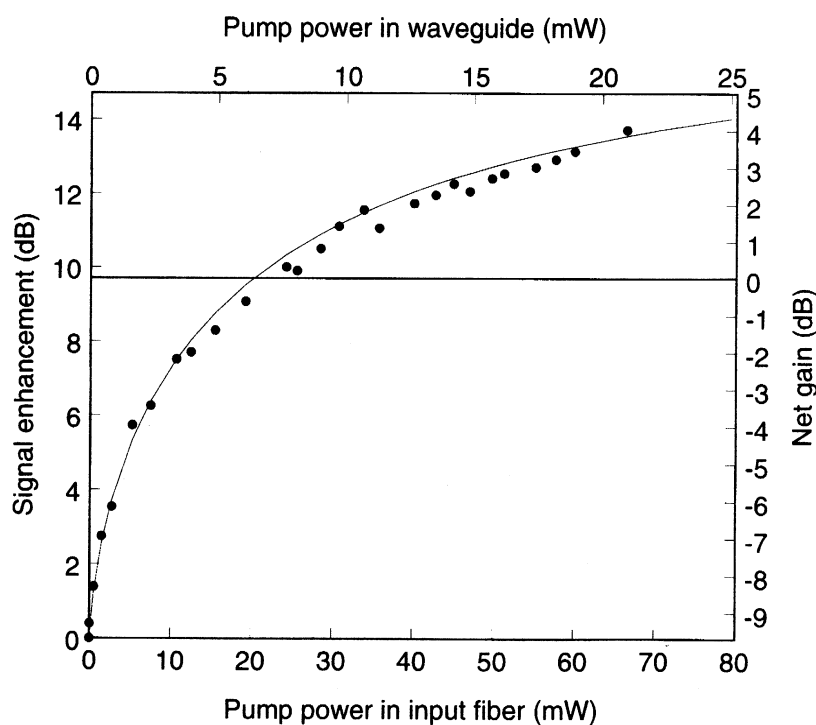


Figure 2.4. Small signal gain measurement on a 1 cm long Er doped phosphate glass waveguide amplifier on Si, taken from Ref. 29. When no pump power is applied, about -10 dB (10%) of the 1.54 μm signal is transmitted, due to waveguide losses and absorption by unexcited Er. At about 7 mW of 0.98 μm pump power in the waveguide (20 mW in the tapered input fiber), these losses are overcome by stimulated emission from the Er. At 21 mW pump power in the guide, a net gain of 4.1 dB is reached. The drawn line is a calculation taking into account the effect of co-operative upconversion.

Another high index waveguide amplifier on Si was developed by van Weerden *et al.* at the *Twente University of Technology* (the Netherlands).²⁸ Their Er doped polycrystalline Y_2O_3 waveguide amplifier shows 6 dB internal gain at only 12 mW pump power in the waveguide. The core material was sputter deposited, and a ridge structure was defined by Ar ion beam etching. The relatively high waveguide loss of 0.8 dB/cm is compensated for by the high concentration of Er that can be incorporated in Y_2O_3 .

The highest gain per unit length at low pump power was achieved by Yan *et al.*²⁹ The waveguide film was deposited by RF sputtering from an Er doped multi-component phosphate glass. Strip loaded waveguides were formed by etching of the SiO_2 top cladding layer. A net gain of 4.1 dB is achieved over a 1 cm waveguide, at a coupled pump power of 21 mW at 0.98 μm . A gain measurement on this waveguide amplifier is shown in Fig. 2.4. The high gain is a result of the high Er concentration in the glass (5.3×10^{20} Er/cm³), and the low co-operative upconversion

coefficient, which is a result of the homogeneous Er distribution in this multi-component glass. Due to the relatively high index of the phosphate glass ($n=1.56$), a low pump threshold of only 7 mW could be achieved.

As becomes clear from the overview given above, at present two classes of materials have been successfully used to develop efficient planar Er doped optical amplifiers. In silica based glasses, waveguides have been made with very low losses, in the 0.1 dB/cm range. High optical gains (up to 27 dB) can be achieved, often only using relatively long waveguide structures. Silica based waveguide amplifiers will be most useful in areas of integrated optics where size is less important than efficiency. Co-doping the silica with P_2O_5 leads to an increased refractive index, and hence better mode confinement. This, in combination with a low co-operative upconversion coefficient, has led to the development of an amplifier with a gain of 4.1 dB over 1 cm at 21 mW pump power, the highest reported gain per unit length at low pump power. Ceramic thin films such as polycrystalline Al_2O_3 and Y_2O_3 have an even higher refractive index, allowing miniature devices (typical area 1 mm^2) to be made. Minimizing waveguide losses, and optimizing the local Er distribution in these materials in order to minimize co-operative upconversion is essential to further increase the achievable gain.

2.6 Outlook

Future research in Er doped planar optical amplifiers will focus on further optimization of materials composition and device geometries in order to increase the net gain and reduce the pump power and device dimensions. Aside from research on glasses and ceramic materials, two other materials that can be integrated with Si are of great interest at this stage.

Polymers are interesting materials to use as optical waveguide materials. Their synthesis and processing is quite well developed. They can be deposited at relatively low temperatures ($\sim 200\text{ }^\circ\text{C}$) using the low cost spin-coating process. Polymer based passive devices such as splitters, and thermo-optic switches are now commercially available. As a result of their relatively low index, polymer waveguides are easily coupled to standard silica glass fiber. Doping these polymer waveguide films with Er is not an easy task, as the commonly used rare earth salts are poorly soluble in a polymer matrix. To overcome this problem, Er ions can be incorporated in an organic complex,¹⁵ that does dissolve in a polymer matrix. Research today³⁰ focuses on studying the intra-molecular energy transfer in these complexes, and reducing the non-radiative processes that reduce the Er luminescence quantum efficiency.

Silicon itself would of course be the ideal host for integrated optical amplifiers in Si-based opto-electronics. Si waveguides have extremely well confined optical modes due to their high refractive index, and consequently a bending radius as small as $1\text{ }\mu\text{m}$ can be achieved, enabling the fabrication of miniature optical devices.³¹ It has been shown that Si can be doped with optically active Er, using e.g.

ion implantation³²⁻³⁶ or molecular beam epitaxy techniques.^{37,38} Erbium in Si can be excited not only optically, but also electrically, through an impurity Auger process in which electrical carriers transfer their recombination energy to Er (see Chapters 4-6 of this thesis). In principle, the latter would allow for electrical pumping of an Er doped Si planar waveguide amplifier. However, several limitations have become clear in the past few years. First of all, the maximum optically active Er concentration that can be dissolved in single crystal Si of high optical and electrical quality is limited to roughly 10^{20} Er/cm³. Second, free carrier absorption in an (electrically pumped) Si waveguide will cause high waveguide losses. Thirdly, non-radiative quenching processes reduce the Er luminescence efficiency at room temperature. These problems can be solved by the development of Si/SiO₂ nanocomposite waveguides (see Chapters 7-9 of this thesis), which combine the advantages of the high refractive index of Si with the high Er solubility and reduced non-radiative quenching of SiO₂.

References

- ¹ W. J. Miniscalco, J. Lightwave Technol. **9**, 234 (1991)
- ² A. Polman, J. Appl. Phys. **82**, 1 (1997)
- ³ P. J. Mears, L. Reekie, I. M. Jauncey, and D. N. Payne, Electron. Lett. **23**, 1026 (1987)
- ⁴ E. Desurvire, *Erbium-Doped Fiber Amplifiers: Principles and Applications*, John Wiley & Sons (1994)
- ⁵ See for example, P. D. Townsend, *Optical Effects of Ion Implantation*, Cambridge University Press, Cambridge (1994)
- ⁶ R. V. Ramaswamy, and R. Srivastava, J. Lightwave Technol. **6**, 984 (1988)
- ⁷ K. Hattori, T. Kitagawa, M. Oguma, M. Wada, J. Temmyo, and M. Horiguchi, Electron. Lett. **29**, 357 (1993)
- ⁸ M. Smit, *Integrated Optics in Silicon-Based Aluminum Oxide*, PhD thesis, Delft University of Technology, The Netherlands (1991)
- ⁹ G. N. van den Hoven, R. J. I. M Koper, A. Polman, C. van Dam, J. W. M. van Uffelen, and M. K. Smit, Appl. Phys. Lett. **68**, 1886 (1996)
- ¹⁰ K. Arai, H. Namikawa, K. Kumata, T. Honda, Y. Ishii, and T. Handa, J. Appl. Phys. **59**, 3430 (1986)
- ¹¹ G. N. van den Hoven, E. Snoeks, A. Polman, J. W. M. van Uffelen, Y. S. Oei, and M. K. Smit, Appl. Phys. Lett. **62**, 3065 (1993)
- ¹² G. N. van den Hoven, A. Polman, E. Alves, M. F. da Silva, A. A. Melo, and J. C. Soares, J. Mat. Res. **12**, 1401 (1997)
- ¹³ T. Hoekstra, *Erbium-Doped Y₂O₃ Integrated Optical Amplifiers*, PhD thesis, Twente University of Technology, The Netherlands (1994)
- ¹⁴ M. P. Hehlen, N. J. Cockroft, T. R. Gosnell, and A. J. Bruce, Phys. Rev. B **56**, 9302 (1997)
- ¹⁵ L. H. Slooff, A. Polman, M. P. Oude Wolbers, F. C. J. M. van Veggel, D. N. Reinhoudt, and J. W. Hofstraat, J. Appl. Phys. **83**, 497 (1998)

- ¹⁶ G. N. van den Hoven, E. Snoeks, A. Polman, C. van Dam, J. W. M. van Uffelen, and M. K. Smit, *J. Appl. Phys.* **79**, 1258 (1996)
- ¹⁷ E. Snoeks, G. N. van den Hoven, A. Polman, B. Hendriksen, M. B. J. Diemeer, and F. Priolo, *J. Opt. Soc. Am. B* **23**, 1468 (1995)
- ¹⁸ F. Auzel, *Radiationless processes*, B. DiBartolo, Ed. (Plenum Press, New York, 1980)
- ¹⁹ E. Snoeks, P. G. Kik, and A. Polman, *Opt. Mat.* **5**, 159 (1996)
- ²⁰ Y. Yan, A. J. Faber, and H. de Waal, *J. Non-Cryst. Sol.* **181**, 283 (1995)
- ²¹ G. N. van den Hoven, J. A. van der Elsken, A. Polman, C. van Dam, J. W. M. van Uffelen, and M. K. Smit, *Appl. Optics* **36**, 3338 (1997)
- ²² K. Hattori, T. Kitagawa, M. Oguma, Y. Ohmori and M. Horiguchi, *Electron. Lett.* **30**, 856 (1994)
- ²³ Calculated from a weight percentage, assuming the glass density to be that of silica (2.27 g/cm^3)
- ²⁴ R. N. Ghosh, J. Shmulovich, C. F. Kane, M. R. X. de Barros, G. Nykolak, A. J. Bruce, and P. C. Becker, *IEEE Photon. Technol. Lett.* **8**, 518 (1996)
- ²⁵ J. Shmulovich, A. Wong, Y. H. Wong, P. C. Becker, A. J. Bruce, and R. Adar, *Electron. Lett.* **28**, 1181 (1992)
- ²⁶ D. Barbier, J. -M. P. Delavaux, A. Kevorkian, P. Gastaldo, and J. M. Jouanno, *Proc. OFC'95*, San Diego, CA, (1995)
- ²⁷ J. -M. P. Delavaux, S. Granlund, O. Mizuhara, L. D. Tzeng, D. Barbier, M. Rattay, F. Saint André, and A. Kevorkian, *IEEE Photon. Technol. Lett.* **9**, 247 (1997)
- ²⁸ H. J. van Weerden, T. H. Hoekstra, P. V. Lambeck, and Th. J. A. Popma, *Proc. 8th European conference on integrated optics*, Stockholm, Abstract EThA4, 169 (1997)
- ²⁹ Y. C. Yan, A. J. Faber, H. de Waal, A. Polman and P. G. Kik, *Appl. Phys. Lett.* **71**, 2922 (1997)
- ³⁰ L. H. Slooff, *Rare-earth doped polymer waveguides and LEDs*, PhD thesis, Utrecht University, The Netherlands (2000)
- ³¹ A. M. Agarwal, L. Liao, J. S. Foresi, M. R. Black, X. Duan, and L. C. Kimerling, *J. Appl. Phys.* **80**, 6120 (1996)
- ³² A. Polman, G. N. van den Hoven, J. S. Custer, J. H. Shin, R. Serna, and P. F. A. Alkemade, *J. Appl. Phys.* **77**, 1256 (1995)
- ³³ G. Franzò, S. Coffa, F. Priolo, and C. Spinella, *J. Appl. Phys.* **81**, 2784 (1997)
- ³⁴ B. Zheng, J. Michel, F. Y. G. Ren, L. C. Kimerling, D. C. Jacobson, and J. M. Poate, *Appl. Phys. Lett.* **64**, 2842 (1994)
- ³⁵ S. Coffa, G. Franzò, and F. Priolo, *Appl. Phys. Lett.* **69**, 2077 (1996)
- ³⁶ J. Palm, F. Gan, B. Zheng, J. Michel, and L. C. Kimerling, *Phys. Rev. B* **54**, 17603 (1996)
- ³⁷ R. Serna, Jung H. Shin, M. Lohmeier, E. Vlieg, A. Polman, and P. F. A. Alkemade. *J. Appl. Phys.* **79**, 2658 (1996)
- ³⁸ A. Reittinger, J. Stimmer, and G. Abstreiter, *Appl. Phys. Lett.* **70**, 2431 (1997)

Chapter 3

Co-operative upconversion as the gain limiting factor in Er doped miniature Al₂O₃ optical waveguide amplifiers

Erbium doped Al₂O₃ waveguide amplifiers were fabricated using two different doping methods, namely Er ion implantation into sputter deposited Al₂O₃, and co-sputtering from an Er₂O₃/Al₂O₃ target. Although the Er concentration in both materials is almost identical (0.28 at.% and 0.31 at.%), the amplifiers show a completely different behavior. Upon pumping with 1.48 μm, the co-sputtered waveguide shows a strong green luminescence from the ⁴S_{3/2} level, indicating efficient co-operative upconversion in this material. This is confirmed by pump power dependent measurements of the optical transmission at 1.53 μm and the spontaneous emission at 1.53 μm and 0.98 μm. All measurements can be accurately modeled using a set of rate equations that include first order and second order co-operative upconversion. The first order co-operative upconversion coefficient C₂₄ is found to be 3.5×10⁻¹⁶ cm³s⁻¹ in the co-sputtered material, two orders of magnitude higher than the value obtained in Er implanted Al₂O₃ of 4.1×10⁻¹⁸ cm³s⁻¹. It is concluded that the co-sputtering process results in a strongly inhomogeneous atomic scale spatial distribution of the Er ions.

3.1 Introduction

Erbium doped waveguide amplifiers can be used in optical integrated circuits to compensate for signal losses, e.g. absorption loss, scattering loss, or coupling loss. Such waveguide amplifiers use stimulated emission from the first excited state (⁴I_{13/2}) to the ground state (⁴I_{15/2}) of Er³⁺ at 1.54 μm (see Fig. 3.1(a)). The intra-4*f* transition is parity forbidden, and as a result the emission cross section is quite small (~10⁻²¹ cm²). Consequently, high Er concentrations (0.1-1 at.%) are required to achieve significant amplification in waveguide structures on a cm length scale. At these high Er concentrations the closely spaced Er³⁺ ions can interact. This

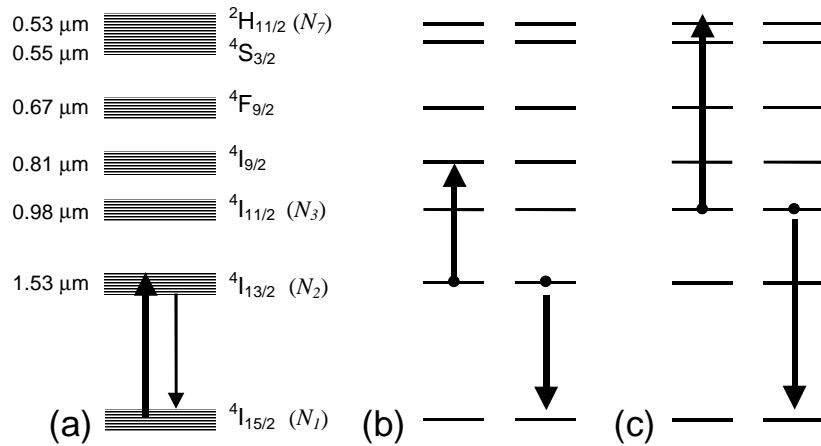


Figure 3.1. (a) Schematic representation of the Stark-split Er^{3+} energy levels, showing excitation at 1.48 μm and emission at 1.53 μm . The energy levels are indexed using Russell-Saunders notation, and the corresponding populations N_i are indicated. The emission wavelength due to radiative relaxation to the ground state is also included. (b) Co-operative upconversion from the Er^{3+} first excited state, bringing one ion in the $4I_{9/2}$ state. This is followed by rapid relaxation to the $4I_{11/2}$ level, causing luminescence at 0.98 μm . (c) Co-operative upconversion from the Er^{3+} second excited state, bringing one ion in the $2H_{11/2}$ state that luminesces in the green.

causes several effects, such as energy migration,¹ in which an excited Er ion excites a neighboring unexcited Er ion (which may in turn be coupled to a non-radiative quenching site), and co-operative upconversion,^{2,3} in which an excited Er ion promotes a neighboring excited Er ion into a higher lying state. Both processes are detrimental to the optical gain, as they reduce the population in the first excited state.

In this chapter we compare the optical gain characteristics of two different optical waveguide amplifiers on silicon that have been fabricated either by $\text{Er}_2\text{O}_3/\text{Al}_2\text{O}_3$ co-sputtering or by Er ion implantation into Al_2O_3 . We will show that although the Er concentrations in the two amplifiers are almost identical, the gain characteristics are entirely different due to a difference in the atomic scale spatial distribution of the Er ions.

3.2 Experiment

One waveguide structure was fabricated using radio-frequency Ar sputtering of a powder-pressed $\text{Er}_2\text{O}_3/\text{Al}_2\text{O}_3$ sputter target onto an oxidized Si substrate (oxide thickness 5 μm). The target contained 2.8 wt.% Er_2O_3 , corresponding to 0.31 at.% Er. The composition of the deposited film was measured by Rutherford

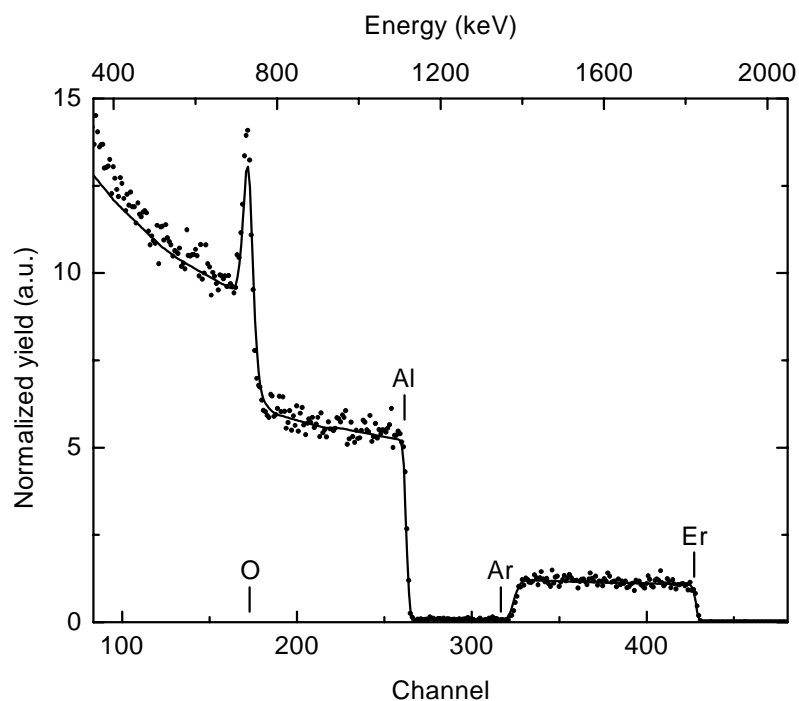


Figure 3.2. Rutherford backscattering spectrometry measurement at a scattering angle of 165° of a 570 nm thick Er doped Al_2O_3 film on SiO_2 made by $\text{Er}_2\text{O}_3/\text{Al}_2\text{O}_3$ co-sputtering. The surface channels of the various elements are indicated. The solid line represents a fit assuming a constant Er concentration of 0.31 at.% over the full film thickness. The peak around channel 170 is the result of overlapping signals from aluminum in the top Al_2O_3 layer and silicon in the lower SiO_2 layer.

backscattering spectrometry (RBS) using 2 MeV He^+ ions at a scattering angle of 165° (Fig. 3.2). The film thickness and the sample composition were determined from a fit to the data (solid line). The film thickness is found to be 570 nm, assuming an atomic density of $9.64 \times 10^{22} \text{ cm}^{-3}$. The Er concentration is constant over the full film thickness, and amounts to 0.31 at.%. The Al concentration is found to be 38 at.%, close to the stoichiometric composition of Al_2O_3 . The film also contains a small amount of Ar (0.25 at.%) which is incorporated during the sputtering process. This material was annealed at 900°C for one hour in vacuum at a base pressure of 2×10^{-7} mbar to optimize the Er luminescence intensity and lifetime.⁴

Ridge waveguides were formed in a 520 nm thick layer using standard photolithography and Ar beam etching to a depth of 260 nm. The etch mask contained straight waveguides of ~ 1 cm length, as well as spiral waveguides that confine a 3 cm long waveguide on an area of 1 mm^2 . Subsequently, a $1 \mu\text{m}$ thick SiO_2 top cladding was deposited to reduce scattering losses. Figure 3.3 shows a scanning electron microscopy image of a $2 \mu\text{m}$ wide Al_2O_3 ridge waveguide, after removal of

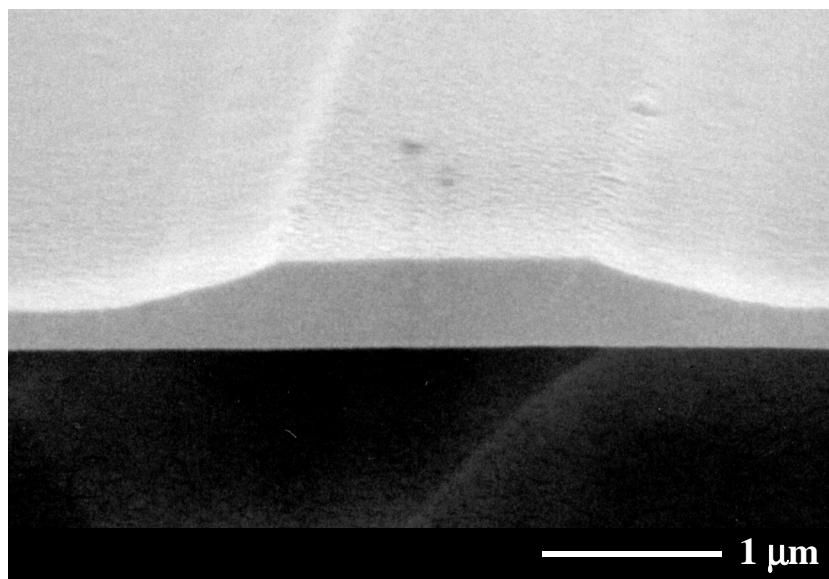


Figure 3.3. Scanning electron microscopy image of an Er doped Al_2O_3 ridge waveguide, fabricated by means of $\text{Er}_2\text{O}_3/\text{Al}_2\text{O}_3$ co-sputtering. The SiO_2 cladding layers have been removed.

the SiO_2 cladding layers. Before waveguide fabrication the Er photoluminescence lifetime at $1.535 \mu\text{m}$ in annealed co-sputtered films was found to be 6.2 ms. The waveguide fabrication reduces the lifetime to 1.7 ms, possibly due to the introduction of defects or impurities such as OH that are known to reduce the Er lifetime.

A second type of amplifier structure was fabricated by sputter deposition of a 600 nm thick layer of Al_2O_3 from a pure Al_2O_3 sputter target, followed by Er ion implantation. An almost constant Er concentration of 0.28 at.% was achieved from 25 to 450 nm below the Al_2O_3 surface using multiple implants at energies in the range 100 keV - 1.5 MeV. Waveguides were fabricated by etching to a depth of 300 nm. This material was previously shown to exhibit a net optical gain of 2.3 dB at $1.53 \mu\text{m}$ in a 4 cm long waveguide amplifier, at a coupled pump power of only 9 mW.⁵ A detailed characterization of the optical properties of this material can be found in Refs. 4 and 6.

To compare the optical gain characteristics of the co-sputtered and ion implanted waveguides, all measurements on the two sample types were performed under identical conditions. The waveguides were pumped using a fiber coupled $1.49 \mu\text{m}$ laser diode with a maximum power of 60 mW in the fiber. The pump light was butt-coupled to the waveguides using a single mode tapered fiber. Optical images of the waveguides were taken using a CCD camera in combination with an optical microscope. Photoluminescence (PL) measurements were done by collecting the spontaneous emission from the waveguides normal to the sample using a multimode

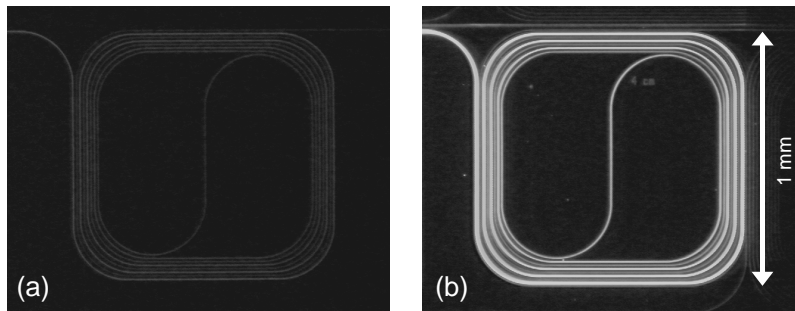


Figure 3.4. (a) Optical image of a spiral waveguide amplifier doped with 0.28 at.% Er using ion implantation into Al_2O_3 . The waveguide is pumped at $1.49 \mu\text{m}$ at a pump power of 60 mW in the input fiber. The waveguide emits green light as a result of two subsequent co-operative upconversion interactions. (b) Optical image of a similar waveguide doped with 0.31 at.% Er using $\text{Er}_2\text{O}_3/\text{Al}_2\text{O}_3$ co-sputtering. The intense upconversion luminescence is ascribed to a strongly inhomogeneous atomic scale Er distribution.

fiber placed approximately 1 mm above the sample surface. The collected luminescence was sent to a grating monochromator and detected using a liquid nitrogen cooled Ge detector, in combination with standard lock-in techniques. Optical gain measurements were performed by adding a $1.530 \mu\text{m}$ signal from a low power tunable laser to the input fiber, and monitoring the transmitted signal power as a function of applied pump power. The signal power in the input fiber was kept below 0.1 mW. The transmitted signal was collected by imaging the waveguide end facet onto a multimode fiber using a $40\times$ microscope objective, and detected as in the PL measurements. A band-pass filter in the range $1.51\text{-}1.56 \mu\text{m}$ was placed in front of the monochromator entrance slit in order to suppress any pump related background signal.

3.3 Results and discussion

Figure 3.4(a) shows an optical image of an Er implanted Al_2O_3 spiral waveguide. The waveguide is pumped at $1.49 \mu\text{m}$ at a power of 60 mW in the input fiber. At this pump power the waveguide emits a faint green luminescence (the dark gray spiral in Fig. 3.4(a)). Photoluminescence measurements of the visible emission (not shown) indicate that the green emission originates from the $^2\text{H}_{11/2}$ and $^4\text{S}_{3/2}$ levels of Er^{3+} . The luminescence seen in Fig. 3.4 also contains red emission from the $^4\text{F}_{9/2}$ level at 670 nm. These higher lying levels are populated via a two-step co-operative upconversion process, as depicted in Figs. 3.1(b) and 3.1(c). First, two Er ions in the $^4\text{I}_{13/2}$ state interact to yield an ion in the $^4\text{I}_{9/2}$ state (Fig. 3.1(b)), which is followed by a non-radiative relaxation to the $^4\text{I}_{11/2}$ level. Secondly, two ions in the $^4\text{I}_{11/2}$ level interact to yield an ion in the $^2\text{H}_{11/2}$ level (Fig. 3.1(c)), which relaxes to

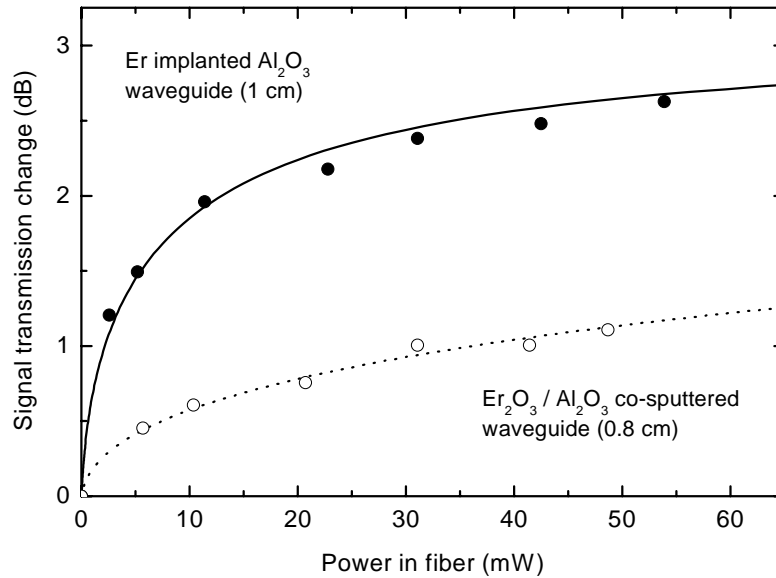


Figure 3.5. Measured transmission change at $1.53 \mu\text{m}$ as a function of $1.49 \mu\text{m}$ pump power in a 1 cm long Er doped Al_2O_3 waveguide made by ion implantation (\bullet) and in a 0.8 cm long Er doped Al_2O_3 waveguide made by $\text{Er}_2\text{O}_3/\text{Al}_2\text{O}_3$ co-sputtering (\circ). The drawn lines are based on population calculations using the parameters in Table 3.1. The $\text{Er}_2\text{O}_3/\text{Al}_2\text{O}_3$ co-sputtered waveguide shows a lower signal change due to strong co-operative upconversion.

the $^4\text{S}_{3/2}$ level. Figure 3.4(b) shows an image of the $\text{Er}_2\text{O}_3/\text{Al}_2\text{O}_3$ co-sputtered waveguide taken under the same pumping conditions. This waveguide shows a very intense upconversion luminescence, even though the Er concentration is only slightly higher than in the ion implanted sample (0.31 at.% vs. 0.28 at.%).

The amount of optically active Er^{3+} in the co-sputtered waveguide was determined from transmission measurements in the range $1.4\text{--}1.7 \mu\text{m}$ (not shown). The Er related peak absorption in the co-sputtered waveguide was found to be 3.1 dB/cm . Using the calculated overlap Γ of the optical mode with the Er depth profile ($\Gamma=49\%$), and the Er peak absorption cross section σ_{12}^s of $5.8 \times 10^{-21} \text{ cm}^2$ taken from Ref. 6, the concentration of optically active Er in the waveguide is found to be $2.5 \times 10^{20} \text{ cm}^{-3}$, 17% less than the total Er concentration determined by RBS. This suggests that 83% of the Er is in the optically active 3+ valence state. The Er related peak absorption in the ion implanted waveguide is only 2.5 dB/cm , due to the lower mode overlap with the Er implantation profile.

Figure 3.5 shows the measured signal transmission change at $1.530 \mu\text{m}$ as a function of applied pump power at $1.49 \mu\text{m}$ for a 1 cm long straight waveguide made by ion implantation, and a 0.8 cm long straight waveguide made by co-sputtering. A maximum signal transmission change of 2.5 dB is observed in the Er

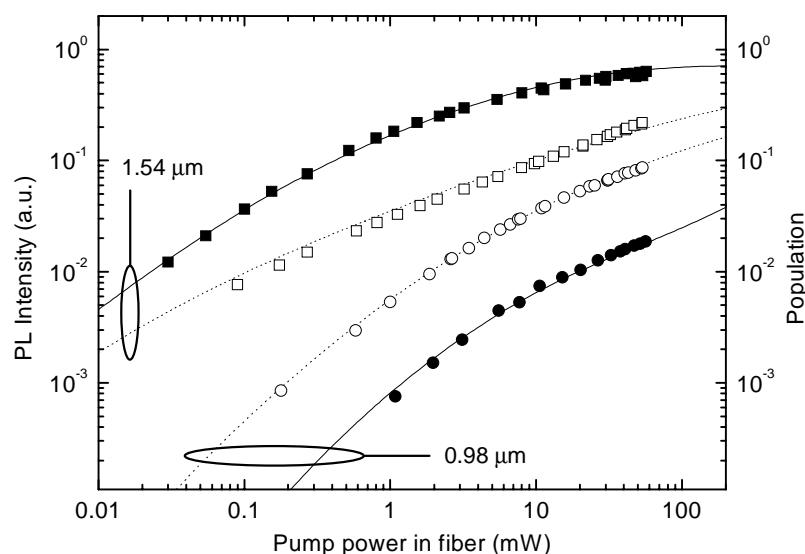


Figure 3.6. Photoluminescence from Er doped Al_2O_3 waveguides pumped at $1.49 \mu\text{m}$. Solid symbols refer to ion implanted material, open symbols to $\text{Er}_2\text{O}_3/\text{Al}_2\text{O}_3$ co-sputtered material. The drawn lines are calculations of the fraction of excited Er^{3+} obtained using the parameters listed in Table 3.1.

implanted waveguide, corresponding to the onset of Er related gain. At the same pump power, the signal transmission in the co-sputtered waveguide has changed by only 1.2 dB, and consequently no Er related gain is obtained. Note that the shape of the two curves in Fig. 3.5 is quite different, the ion implanted waveguide showing a stronger curvature. This is a consequence of the strong upconversion in the co-sputtered sample, as will be shown below.

To investigate the upconversion in the waveguides quantitatively, we have measured the spontaneous emission at $1.53 \mu\text{m}$ and $0.98 \mu\text{m}$ normal to the waveguide as a function of pump power. The luminescence was collected from the middle of the sample to avoid collection of pump light scattered from the input and output facets. The luminescence intensities found in both sample types are plotted in Fig. 3.6. At low pump power, the $1.53 \mu\text{m}$ luminescence from the ion implanted waveguide increases linearly with pump power. At pump powers above 1 mW in the fiber the intensity starts to show significant saturation, as was observed before.⁷ An entirely different pump power dependence is seen in the co-sputtered waveguide. Within the full range of applied pump powers, the $1.53 \mu\text{m}$ luminescence exhibits an almost perfect square-root dependence on pump power. Furthermore, the maximum $1.53 \mu\text{m}$ luminescence intensity in the co-sputtered waveguide is found to be significantly lower than in the ion implanted waveguide. This is consistent with the gain measurements in Fig. 3.5, which showed that the maximum achieved signal transmission change in the co-sputtered waveguide is lower than in the ion implanted waveguide. Both sample types show a similar pump power dependence of the $0.98 \mu\text{m}$ luminescence from the $^4\text{I}_{11/2}$ state, but the co-sputtered waveguide

shows a much higher luminescence intensity at 0.98 μm . This clearly shows that the co-sputtered sample exhibits stronger upconversion than the ion implanted sample. These findings are consistent with the intense green luminescence emitted by the co-sputtered waveguide (Fig. 3.4(b)), which is the result of upconversion from Er ions that are in the $^4\text{I}_{11/2}$ state.

In order to analyze the data in Figs. 3.5 and 3.6, we model the Er^{3+} as a three-level system. This generally yields good results for the populations in the lower lying levels, because the population build-up in the levels above the $^4\text{I}_{11/2}$ level is small as a result of their low ($< 1 \mu\text{s}$) lifetimes.⁸ The rate equations that determine the Er populations are:

$$\frac{dN_3}{dt} = -(W_3 + C_{37}N_3)N_3 + (R_{24} + C_{24}N_2)N_2 \quad (1)$$

$$\frac{dN_2}{dt} = -(W_2 + R_{24} + R_{21} + 2C_{24}N_2)N_2 + W_3N_3 + R_{12}N_1 \quad (2)$$

$$\frac{dN_1}{dt} = +(W_2 + R_{21} + C_{24}N_2)N_2 - R_{12}N_1 + C_{37}N_3 \quad (3)$$

with N_i (cm^{-3}) the concentration of Er in level i (see Fig. 3.1(a)), $W_i = \tau_i^{-1}$ (s^{-1}) the measured spontaneous decay rate from level i , R_{ij} (s^{-1}) a pump induced transition from level i to level j , and C_{ij} (cm^3s^{-1}) the co-operative upconversion coefficient from level i , producing one ion in the ground state and one ion in level j . We have assumed that spontaneous decay from level 3 is dominated by non-radiative relaxation to level 2. The pump rates R_{ij} are related to the photon flux φ ($\text{cm}^{-2}\text{s}^{-1}$) in the waveguide and the cross section σ_{ij}^p (cm^2) for a pump induced transition from $i \rightarrow j$ according to $R_{ij} = \sigma_{ij}^p \times \varphi$. Note that stimulated emission and excited state absorption by the pump are included. The mean photon flux φ is given by $\varphi = \eta \times P_{fib} / (E_{phot} \times A)$ with η the coupling efficiency between the fiber and the waveguide, P_{fib} (W) the power in the input fiber, E_{phot} (J) the photon energy, and A (cm^2) the effective optical mode area. The sum of all populations is equal to N_0 , the concentration of optically active Er in the waveguide. Note that an Er ion excited to the N_7 level by second order upconversion from the N_3 level is assumed to relax back to the N_3 state immediately via multi-phonon emission, and hence a single C_{37} term appears in Eq. 1 (compared to a $2C_{24}N_2$ term in Eq. 2). The solutions of Eqs. 1-3 can be used to calculate the Er related signal change G at 1.530 μm according to

$$G(\text{dB}/\text{cm}) = 10 \times \log(e) \times (\sigma_{21}^s N_2 - \sigma_{12}^s N_1 - \sigma_{24}^s N_2) \times f_{Er^{3+}} \times \Gamma, \quad (4)$$

with σ_{ij}^s the cross section for a signal induced transition $i \rightarrow j$, $f_{Er^{3+}}$ the fraction of Er in the optically active 3+ state, and Γ the overlap of the optical mode with the Er doped core of the waveguide.

The rate equations 1-3 were first solved numerically for steady state using the parameters as determined for ion implanted Al_2O_3 from Refs. 6 and 7. Upconversion from the second excited state (coefficient C_{37}) is assumed to be negligible in this case, since the green upconversion luminescence is very faint. The obtained populations N_2 and N_3 were then multiplied by a scaling factor to match the measured $1.53 \mu\text{m}$ and $0.98 \mu\text{m}$ PL intensities for the ion implanted waveguides, and the coupling efficiency was used as a fitting parameter. Optimum agreement between the calculations and the measurements is obtained for $\eta=0.03$. Using these parameters, the $1.53 \mu\text{m}$ luminescence is described very well. The $0.98 \mu\text{m}$ luminescence at high power however is overestimated, suggesting that the used cross section for excited state absorption (taken from Ref. 6) is too high for this sample. A good fit is obtained using $\sigma_{24}^p=0.25 \times 10^{-21} \text{ cm}^2$. Using these parameters the gain measurement for the ion implanted sample can be fitted assuming an optically active Er fraction of 83%. All parameters used are summarized in Table 3.1. The calculations are included in Figs. 3.5 and 3.6 (drawn lines). All three data sets are well reproduced for all applied pump powers.

A similar analysis was done for the co-sputtered waveguide. The luminescence intensity curves in Fig. 3.6 were calculated using the cross sections found for the ion implanted sample and the luminescence lifetimes τ_2 and τ_3 as measured in the co-sputtered waveguide (see Table 3.1). The upconversion coefficients C_{24} and C_{37} , and the coupling efficiency η were used as fit parameters. Using the values listed in Table

	<i>ion implanted</i>	<i>co-sputtered</i>
$C_{Er} \text{ (cm}^{-3}\text{)}$	2.7×10^{20}	3.0×10^{20}
$f_{Er^{3+}} \text{ (%)}$	83	83
$\tau_2 \text{ (ms)}$	7.8	1.7
$\tau_3 \text{ (}\mu\text{s)}$	30	55
$C_{24} \text{ (cm}^3\text{s}^{-1}\text{)}$	4.1×10^{-18}	3.5×10^{-16}
$C_{37} \text{ (cm}^3\text{s}^{-1}\text{)}$	-	8×10^{-16}
$\sigma_{12}^p \text{ (cm}^2\text{)}$	2.7×10^{-21}	id.
$\sigma_{21}^p \text{ (cm}^2\text{)}$	0.77×10^{-21}	id.
$\sigma_{24}^p \text{ (cm}^2\text{)}$	0.25×10^{-21}	id.
$\sigma_{12}^s \text{ (cm}^2\text{)}$	5.8×10^{-21}	id.
$\sigma_{21}^s \text{ (cm}^2\text{)}$	6.1×10^{-21}	id.
$\sigma_{24}^s \text{ (cm}^2\text{)}$	0.25×10^{-21}	id.
$L \text{ (cm)}$	1	0.8
$\eta \text{ (%)}$	3	7
$\Gamma \text{ (%)}$	36	49

Table 3.1. Parameter values used in the gain calculations in Fig. 3.5 and the calculations of the pump power dependent photoluminescence intensities in Fig. 3.6.

3.1, the experimental data are reproduced quite well. In order to achieve the square root-like behavior over the full range of pump powers, a high upconversion coefficient C_{24} of $3.5 \times 10^{-16} \text{ cm}^3/\text{s}$ is required. The square root-like behavior can be understood as follows: in case of strong upconversion, the population in the first excited state will remain low at most applied pump powers, and the Er decay rate will be dominated by the term $2C_{24}N_2$ in Eq. 2. In the low population limit, we have $N_2 \propto R_{12}\tau_2 \approx R_{12}/(2C_{24}N_2)$. This gives $N_2 \propto (R_{12})^{1/2}$, which indeed produces the observed square root-like dependence of N_2 on pump power.

The upconversion coefficient C_{24} found for the co-sputtered sample ($3.5 \times 10^{-16} \text{ cm}^3\text{s}^{-1}$) is two orders of magnitude higher than the value measured in ion implanted waveguides ($4.1 \times 10^{-18} \text{ cm}^3\text{s}^{-1}$). This strong Er-Er interaction at low Er concentration suggests that the Er in the co-sputtered material is not distributed homogeneously. Regions with a high local Er concentration could form in different ways. The use of an $\text{Er}_2\text{O}_3/\text{Al}_2\text{O}_3$ powder-mixed sputter target could for example result in the deposition of Er_2O_3 molecules, which yields a small Er-Er separation at low average Er concentration. Alternatively, during sputter deposition the Er ions may migrate over the sample surface, and form regions of high Er concentration. Such mechanism would be favored by the large difference in ionic radius of Al^{3+} and Er^{3+} (0.68 and 1.03 Å respectively), making incorporation of an Er ion onto an Al lattice site unlikely.

To distinguish between the presence of 'molecular' aggregates or more extended regions with high Er concentration we performed ion beam mixing experiments, in which a co-sputtered film was irradiated with 2 MeV Xe ions to a fluence of $2.5 \times 10^{15} \text{ cm}^{-2}$. Under these conditions each atom in the film will be displaced >5 times, as was calculated using the simulation program TRIM. If the high upconversion coefficient is caused by the presence of separate Er_2O_3 molecules, the ion beam mixing should substantially reduce C_{24} . However, no influence of ion beam mixing on the gain characteristics or the pump power dependent luminescence was observed. It is therefore more likely that the co-sputtered film contains regions of relatively high Er concentration, possibly due to surface migration during the sputtering process. Such regions were not observed in high resolution transmission electron microscopy nor in X-ray diffraction measurements. A technique more sensitive to the local atomic environment of the Er ions, such as extended X-ray absorption fine structure spectroscopy (EXAFS) may resolve this issue.

The success of ion implantation in this comparison lies in the non-equilibrium nature of the implantation process, allowing for a relatively homogeneous Er distribution. Ion implantation however is a rather slow and costly fabrication method. For commercial applications of miniature optical amplifiers, different growth methods and different materials compositions should be further investigated. A low upconversion coefficient may for example be obtained by increasing the Er solubility by varying the waveguide composition. Alternatively, depositing at low temperature or at a high deposition rate will minimize effects as surface diffusion, and may also reduce the effect of upconversion.

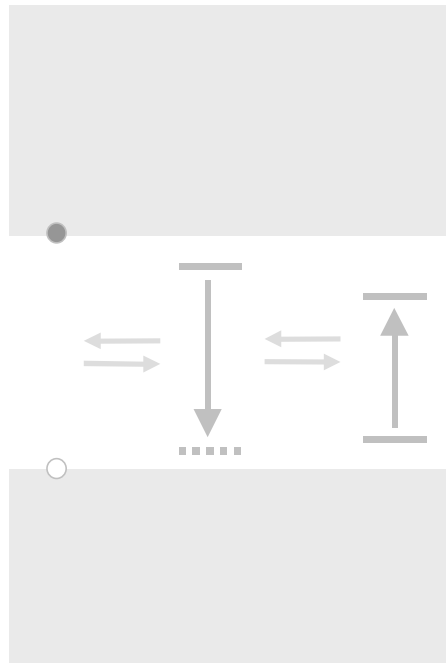
3.4 Conclusions

We have fabricated two types of miniature optical waveguide amplifiers, by Er ion implantation into Al_2O_3 , and by $\text{Er}_2\text{O}_3/\text{Al}_2\text{O}_3$ co-sputtering. It is found that the co-operative upconversion coefficient C_{24} in the co-sputtered material is two orders of magnitude higher than in the ion implanted material. As a result the co-sputtered material shows poor amplification characteristics. The high upconversion coefficient is attributed to a strongly non-homogeneous Er distribution resulting from the co-sputtering process.

References

- ¹ F. Auzel, *Radiationless processes*, B. DiBartolo, Ed. (Plenum Press, New York, 1980)
- ² W. J. Miniscalco, *J. Lightwave Technol.* **9**, 234 (1991)
- ³ P. Blixt, J. Nilsson, T. Carlnäs, and B. Jaskorzynska, *IEEE Photon. Technol. Lett.* **3**, 996 (1991)
- ⁴ G. N. van den Hoven, E. Snoeks, A. Polman, J. W. M. van Uffelen, Y. S. Oei, and M. K. Smit, *Appl. Phys. Lett.* **62**, 3065 (1993)
- ⁵ G. N. van den Hoven, R. J. I. M. Koper, A. Polman, C. van Dam, J. W. M. van Uffelen, and M. K. Smit, *Appl. Phys. Lett.* **68**, 1886 (1996)
- ⁶ G. N. van den Hoven, J. A. van der Elsken, A. Polman, C. van Dam, J. W. M. van Uffelen, and M. K. Smit, *Appl. Opt.* **36**, 3338 (1997)
- ⁷ G. N. van den Hoven, E. Snoeks, A. Polman, C. van Dam, J. W. M. van Uffelen, and M. K. Smit, *J. Appl. Phys.* **79**, 1258 (1996)
- ⁸ See e.g. E. Desurvire, *Erbium-doped fiber amplifiers* (John Wiley & Sons, New York, 1994)

Part II



Chapter 4

Excitation and de-excitation of Er^{3+} in crystalline silicon

Temperature dependent measurements of the 1.54 μm photoluminescence of Er implanted N co-doped crystalline Si are made. Upon increasing the temperature from 12 K to 150 K, the luminescence intensity quenches by more than a factor thousand, while the luminescence lifetime quenches from 420 μs to 3 μs . The quenching processes are described by an impurity Auger energy transfer model that includes bound exciton dissociation and a non-radiative energy backtransfer process. Electron and hole trap levels are determined. It is concluded that the observed decrease in the Er luminescence intensity is mainly caused by a reduction of the Er luminescence efficiency due to energy backtransfer. At temperatures above 100 K, exciton dissociation is found to reduce the Er excitation efficiency. Direct evidence for a backtransfer process followed by exciton dissociation is obtained from analysis of spectral response measurements on an Er implanted Si solar cell.

4.1 Introduction

With the increasing importance of combining optical and electronic technology, the need for an effective light source in silicon grows. One way of realizing such a light source is by optical doping, in which optically active elements are incorporated in the silicon matrix. Erbium is an interesting optical dopant, as its intra-4f transition from the first excited state (${}^4\text{I}_{13/2}$) to the ground state (${}^4\text{I}_{15/2}$) causes luminescence at 1.54 μm , a standard wavelength in telecommunication.

Erbium luminescence in crystalline silicon has been extensively studied in the past years.¹⁻⁷ Excitation spectroscopy has shown that Er photoluminescence in silicon is not caused by resonant absorption of pump photons, but by excitation via optically generated electrons and holes. The excitation mechanism that has been proposed³ to describe Er excitation in Si is shown in Fig. 4.1. In this model, electrons are trapped (T) at a deep level in the silicon bandgap, where they form a

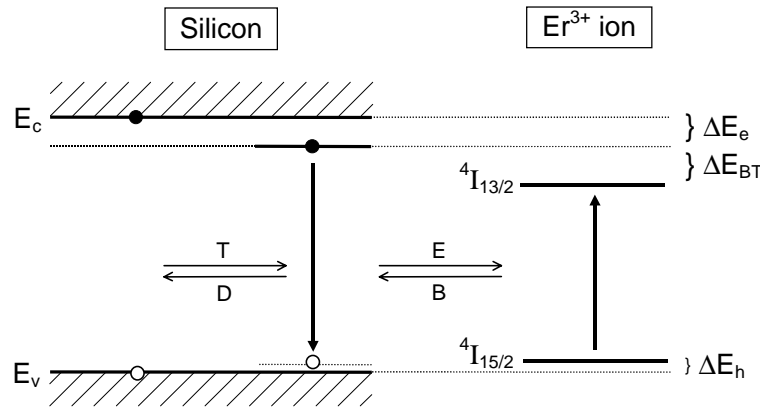


Figure 4.1. Model of excitation and de-excitation of Er^{3+} in Si. Exciton trapping (T) and dissociation (D), Er^{3+} excitation (E) and energy backtransfer (B) are indicated by the horizontal arrows.

bound exciton. The deep level can for example be an impurity induced level³ or a level corresponding to a hybridization between the Er^{3+} 5d state and silicon conduction band states.⁸ Recombination of a bound exciton can excite (E) the Er^{3+} 4f-shell in an Auger process. The erbium ion can then decay radiatively, resulting in 1.54 μm luminescence.

Although relatively bright Er luminescence is commonly observed at low temperature ($T < 100$ K), the luminescence intensity is found to decrease rapidly upon increasing the temperature to room temperature. This luminescence quenching can be due to a lowering of either the excitation efficiency or the Er luminescence efficiency. The excitation efficiency can decrease due to an increase of the bulk recombination rate at higher temperatures, which competes with recombination at the Er related trap level. Alternatively, the Er excitation efficiency may decrease due to the reverse of process (T), which is dissociation of a localized exciton (D). This process lowers the fraction of trapping events that results in Er excitation. The dissociation process must be phonon-assisted, since it requires an activation energy of ΔE_e , ΔE_h as shown in Fig. 4.1. Consequently, the dissociation rate increases with increasing temperature.

The Er luminescence efficiency can decrease as a result of energy backtransfer (B) from excited erbium to a trapped carrier state. Such backtransfer, followed by either exciton dissociation, or exciton recombination at the trap, decreases the Er excited state lifetime, and with it the Er luminescence efficiency. Due to the energy mismatch between excited Er and the localized exciton state, the backtransfer process also requires thermal energy, indicated by ΔE_{BT} in Fig. 4.1. Consequently, as the temperature is increased, the Er lifetime is expected to decrease. The luminescence efficiency can also be influenced by Auger energy transfer to free carriers,⁶ if these are present at sufficiently high concentration.

These carriers are present either because of active optical pumping, or due to electrical doping of the Si. The latter possibility also induces a temperature dependent quenching, since the electrical dopants ionize as the temperature is increased, leading to an increasing Auger quenching and a lower luminescence lifetime.

Although the model outlined above has been used to describe the luminescence quenching of erbium in crystalline silicon, no direct proof of the dissociation and backtransfer processes has been supplied. Furthermore, few reports have been made of the position of the relevant deep levels in the bandgap. In this chapter, we present measurements of the temperature dependence of the erbium photoluminescence intensity and lifetime in nitrogen co-doped crystalline silicon. We acquire information on the position of the energy levels involved in excitation and de-excitation of the erbium. From the data we find that backtransfer is the main quenching factor. The data are used to explain the 1.54 μm photoresponse observed in Er doped solar cells presented by Keevers *et al.*⁹

4.2 Experiment

A single crystal Czochralski grown silicon wafer (p-type, B-doped, [100], 1-10 Ωcm) was implanted with Si, N and Er at room temperature, at a pressure below 10^{-6} mbar. Silicon was implanted at 450 keV to a fluence of $3.5 \times 10^{15} \text{ cm}^{-2}$. Nitrogen was co-implanted at 225 keV to a fluence $1 \times 10^{15} \text{ cm}^{-2}$, followed by an erbium implant at 1.46 MeV to a fluence of $1.6 \times 10^{14} \text{ cm}^{-2}$. The sample was annealed in vacuum for two hours at 490 °C and for one hour at 600 °C, to recrystallize the implanted layer. Rutherford backscattering spectrometry showed that the Er has a Gaussian depth distribution at a depth of 490 nm, with a full width at half maximum (FWHM) of 310 nm and a peak concentration of $5 \times 10^{18} \text{ cm}^{-3}$.¹⁰ The nitrogen concentration profile as determined from secondary ion mass spectrometry peaks at a depth of 580 nm and shows a FWHM of 200 nm and a peak concentration of $6 \times 10^{19} \text{ cm}^{-3}$.

Photoluminescence (PL) measurements were done using the 515 nm line of an Ar ion laser as a pump beam. The pump beam was modulated by an acousto-optic modulator. The sample was mounted in a closed cycle helium cryostat, using silver paint to ensure good thermal contact. The PL signal was focused into a grating monochromator, and detected using a liquid nitrogen cooled Ge detector in combination with standard lock-in techniques. Luminescence decay traces were obtained by averaging the detector signal on a digital oscilloscope. The system response time was 0.5 μs . Measurements were taken at temperatures ranging from 12 K to 170 K.

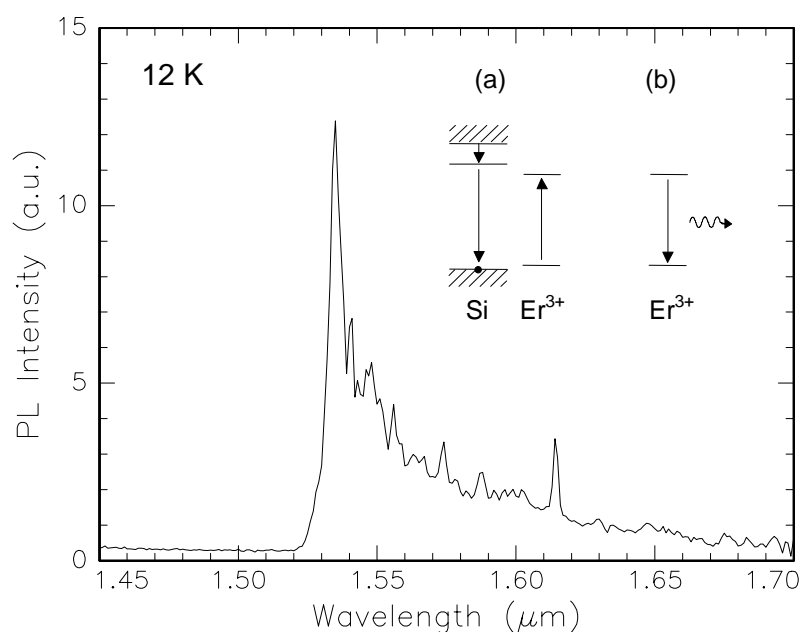


Figure 4.2. Photoluminescence spectrum of Er and N doped crystalline silicon at 12 K. Schematically indicated are the processes of (a) exciton trapping followed by Er excitation and (b) radiative relaxation of the Er.

4.3 Results and discussion

Figure 4.2. shows a PL spectrum taken at a temperature of 12 K. The observed erbium spectrum is typical for erbium in silicon,¹⁰ showing a series of sharp lines due to the Stark-splitting of the intra-4f levels, and a main peak at a wavelength of 1.535 μm . The small signal observed at wavelengths below 1.520 μm is often seen in Er implanted Si, and is attributed to luminescence from ion implantation induced defects in Si that remain after annealing.

Figure 4.3 shows an Arrhenius plot of the integrated Er PL intensity (open circles). To achieve optimum signal-to-noise ratio, the data in Fig. 4.3 were taken at different pump powers in the range of 1 mW to 100 mW, and then normalized to pump power. All data were taken in the regime where the PL intensity depends linearly on pump power, precluding effects of beam heating, saturation of the erbium excited state, and beam induced free carrier Auger quenching of the Er^{3+} excited state. A slight intensity quenching is observed up to a temperature of 85 K, above which a much stronger quenching sets in.

Luminescence decay measurements were performed at 1.535 μm , at temperatures ranging from 12 K to 170 K. At low temperatures, the luminescence decay is almost purely single exponential. At higher temperatures the decay becomes strongly non-exponential. The $1/e$ decay times τ_{Er} are included in Fig. 4.3

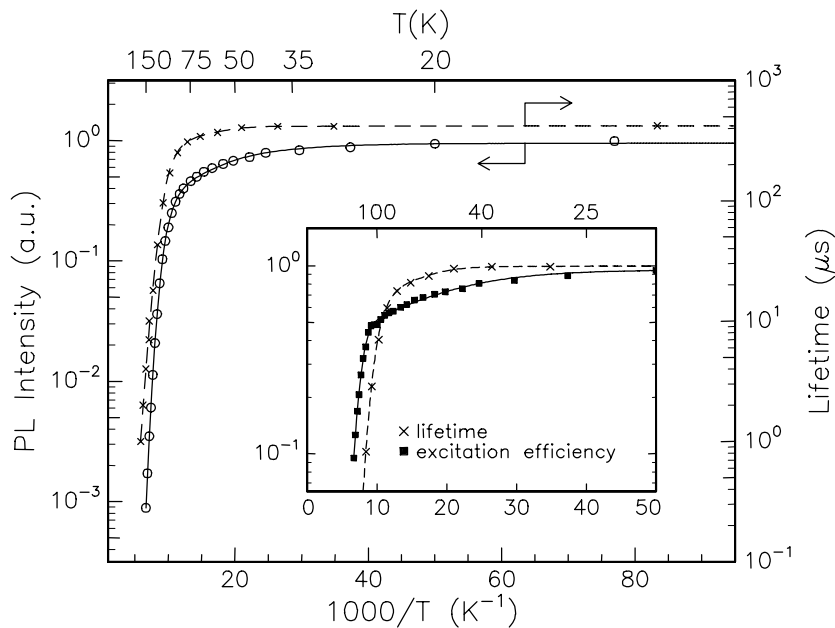


Figure 4.3. Arrhenius plot of the temperature dependence of the 1.54 μm PL intensity (circles, left axis) and the $1/e$ luminescence lifetime (crosses, right axis) of Er and N implanted crystalline Si.

(crosses). A strong decrease in lifetime is observed above 85 K, indicating that a decrease in luminescence efficiency is an important factor in the measured intensity quenching. The slight intensity decrease observed in going from 12 K to 85 K is not accompanied by a decrease in lifetime, indicating that this intensity quenching is caused by a change in excitation efficiency, and not by a change in luminescence efficiency. This might be due to the detrapping of holes weakly bound to a filled trap.

The observed temperature dependence of the lifetime can be described using the model in Fig. 4.1. Once excited, an Er ion can decay through two pathways: either by emitting a 1.54 μm photon, or by energy backtransfer to a deep level in the gap, generating a bound exciton. The exciton can then either re-excite the Er, dissociate, or recombine at a rate W_R without exciting Er. The latter process is assumed to occur at a higher rate than the low temperature spontaneous Er decay rate W_0 . The total decay rate W , equal to $1/\tau_{Er}$, is then given by

$$W = W_0 + W_E e^{-\Delta E_{BT}/kT}. \quad (1)$$

The exponential term accounts for the phonon assisted backtransfer process, where W_E is a pre-factor and ΔE_{BT} the energy difference involved in the backtransfer process (see Fig. 4.1). From the high temperature slope of the lifetime curve, we

find $\Delta E_{BT}=135\pm 5$ meV. Furthermore, by fitting Eq. 1 to the lifetime data we find $W_E=10^8-10^{10}$ s⁻¹.

It should be noted that the trap level mentioned in the discussion of the model is not the only carrier recombination center present in the silicon. In reality, recombination at dislocations and point defects introduced by the ion implantation process are likely to dominate the minority carrier lifetime τ_p . We therefore assume that retrapping of a dissociated exciton is negligible. Inserting this in the model, we find the following low pump power behavior for the PL intensity:

$$I_{PL} \propto \frac{W_0}{W} \times \frac{W_E}{W_E + W_R + W_h e^{-\Delta E_h/kT} + W_{eh} e^{-(\Delta E_e + \Delta E_h)/kT}} \times G \tau_p \quad (2)$$

where ΔE_e is the depth of the electron trap, ΔE_h the hole binding energy at an occupied trap, W_R the rate constant for exciton recombination at the trap, W_h the prefactor for hole detrapping, W_{eh} the prefactor for exciton dissociation, G the carrier generation rate, and τ_p the minority carrier lifetime. The prefactors W_h and W_{eh} contain the carrier velocity and the electron and hole capture cross sections. Depending on the nature of the trap, these prefactors scale with temperature as T^α with $-1.5 < \alpha < 0.5$.

The first factor in Eq. 2 gives the Er luminescence efficiency. Consequently, we can obtain a measure for the Er excitation efficiency by dividing the measured intensities by the measured luminescence lifetimes. This was done using a spline fit through the lifetime data (dashed lines, Fig. 4.3). The resulting excitation efficiency is shown in the inset in Fig. 4.3 (squares). The curve clearly shows two activated regimes: a region with a small activation energy up to 100 K attributed to hole detrapping, and a highly activated region above 100 K attributed to exciton dissociation. Note that at 85 K the exciton dissociation is still negligible, while the Er lifetime already starts to decrease strongly. This implies that at these temperatures the observed reduction in Er lifetime is mainly due to energy backtransfer, followed by exciton recombination at the trap level. At higher temperatures, energy backtransfer followed by exciton dissociation starts to occur.

The efficiency data in Fig. 4.3 were fitted using the second and third factor in Eq. 2, by varying ΔE_h , ΔE_e , and the prefactors W_h and W_{eh} , as well as the absolute scaling. Assuming a temperature independent τ_p , and taking into account the allowed range for α in the prefactors, we find $\Delta E_e=125\pm 3$ meV and $\Delta E_h=12\pm 6$ meV. The fitting result for $\alpha=-1/2$ is shown in the inset in Fig. 4.3 (solid line). It is clear that the proposed model describes the two activation regimes in the excitation process quite well.

The mismatch between the Er³⁺ excited state (⁴I_{13/2}) energy and the silicon band gap at 150 K amounts to ~350 meV. The fitted activation energies together bridge only 272±10 meV. One possible explanation of the difference is that the erbium excitation occurs through a level different from that involved in the de-excitation process. For example, impurity related levels such as those introduced by

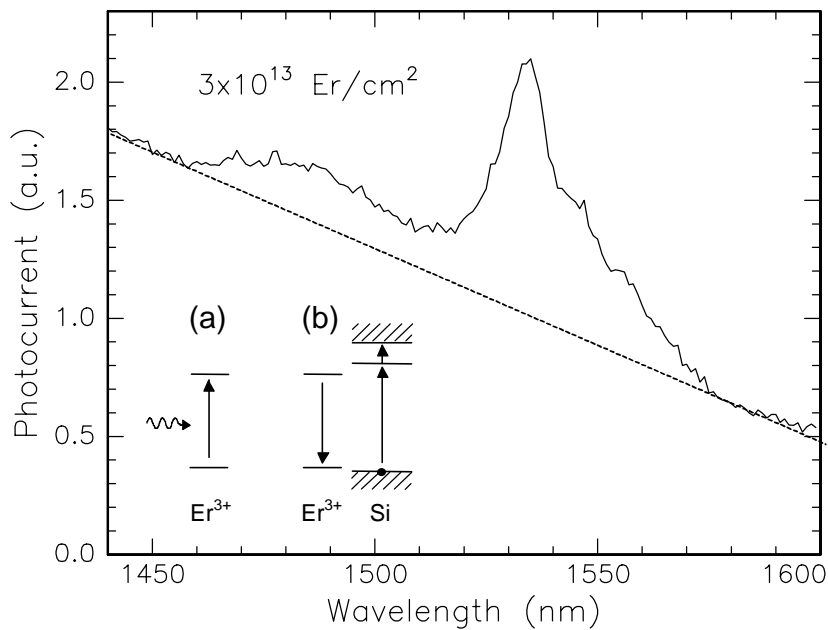


Figure 4.4. Photocurrent spectrum of an erbium implanted PERL silicon solar cell, from data in Ref. 9. The dashed line is a linear interpolation of the background signal. Schematically indicated are the processes of (a) Er excitation and (b) energy backtransfer followed by exciton dissociation.

nitrogen, are spatially rather extended, and couple strongly to conduction band states. Such levels are effective electron-hole recombination centers, which makes them probable excitation channels for the erbium. The predicted Er related 5d-like level⁸ however, is localized near the erbium, resulting in a weak coupling to conduction band states, and a relatively strong coupling to the first excited state of the erbium. Carrier recombination at the latter erbium related energy level could therefore be the main de-excitation channel. This would imply that the erbium PL emission may be optimized by increasing the excitation rate using different impurities and reducing the de-excitation rate by changing the local structure around the erbium (which can in itself also be modified by the addition of impurities).

In order to further investigate the backtransfer process, spectral response measurements on a passivated emitter, rear locally diffused (PERL) Si solar cell¹¹ performed by Keevers *et al.*⁹ were analyzed. The solar cell was implanted with 3.5 MeV Er ions to a fluence of $3 \times 10^{13} \text{ cm}^{-2}$. After implantation the cell was annealed at 1060°C for one hour and at 1000°C for 75 min. The solar cell was made at the University of New South Wales, and its detailed electrical characteristics are reported in Ref. 9.

Figure 4.4 shows the measured photocurrent as a function of wavelength. Superimposed on a decreasing background signal, which is attributed to absorption by implantation induced defects, a pronounced room temperature erbium absorption

spectrum is observed, peaking at a wavelength of 1.535 μm . These data are direct experimental evidence for a backtransfer process leading to the generation of free carriers from an excited state in Er^{3+} . Temperature dependent measurements of the Er related photocurrent, as well as the Er photoluminescence intensity and lifetime measured in the PERL solar cell, are analyzed in Chapter 5. The Er induced photocurrent can be used to fabricate an Er doped waveguide detector in Si. Preliminary measurements on such a waveguide detector structure are discussed in Chapter 6.

4.4 Conclusions

The 1.54 μm Er^{3+} luminescence intensity in crystalline Si, co-doped with 6×10^{19} N cm^{-3} , quenches by three orders of magnitude as the temperature is increased from 12 K to 150 K, while the luminescence lifetime decreases from 420 μs to 3 μs . Using an impurity Auger model to describe the data, we find that the luminescence quenching at high temperature is mainly due to non-radiative Er relaxation, and only partly due to a decrease in excitation efficiency. The Er excitation rate decreases presumably due to electron detrapping with an activation energy of 125 ± 3 meV and hole detrapping with an activation energy of 12 ± 6 meV. A non-radiative erbium de-excitation process with an activation energy of 135 ± 5 meV reduces the erbium luminescence efficiency at high temperatures. The obtained activation energies show that the level causing erbium excitation may be different from the level causing erbium de-excitation. Analysis of photocurrent data of an Er implanted solar cell gives evidence for a non-radiative Er^{3+} de-excitation process, resulting in the generation of free carriers.

References

- ¹ P. N. Favennec, H. l'Haridon, D. Moutonnet, M. Salvi, and M. Gauneau, *Jpn. J. Appl. Phys.* **29**, L524 (1990)
- ² J. Michel, J. L. Benton, R. F. Ferrante, D. C. Jacobson, D. G. Eaglesham, E. A. Fitzgerald, Y. -H. Xie, J. M. Poate and L. C. Kimerling, *J. Appl. Phys.* **70**, 2672 (1991)
- ³ F. Priolo, G. Franzò, S. Coffa, A. Polman, S. Libertino, R. Barklie and D. Carey, *J. Appl. Phys.* **78**, 3874 (1995)
- ⁴ A. Polman, G. N. van den Hoven, J. S. Custer, J. H. Shin, R. Serna and P. F. A. Alkemade, *J. Appl. Phys.* **77**, 1256 (1995)
- ⁵ S. Coffa, G. Franzò, F. Priolo, A. Polman and R. Serna, *Phys. Rev. B* **49**, 16313 (1994)
- ⁶ F. Priolo, G. Franzò, and S. Coffa, and A. Carnera, *Phys. Rev. B* **57**, 4443 (1998)
- ⁷ T. Gregorkiewicz, D. T. X. Thao, J. M. Langer, H. H. P. Th. Bekman, M. S. Bresler, J. Michel, and L. C. Kimerling, *Phys. Rev. B* **61**, 5369 (2000)
- ⁸ M. Needels, M. Schlüter, M. Lannoo, *Phys. Rev. B* **47**, 15533 (1993)

- ⁹ M. J. Keevers, F. W. Saris, G. C. Zhang, J. Zhao, M. A. Green and R. Elliman, Proceedings 13th European Photovoltaic Solar Energy Conference, Nice, Oct. 1995, p. 1215
- ¹⁰ M. J. A. de Dood, P. G. Kik, J. H. Shin and A. Polman, Mat. Res. Soc. Symp. Proc. **422**, 219 (1996)
- ¹¹ M. A. Green, *Silicon Solar Cells*, (University of New South Wales, Sydney, 1995) Ch. 6

Chapter 5

Energy backtransfer and infrared photoresponse in Er doped silicon *p-n* diodes

Temperature dependent measurements of the photoluminescence (PL) intensity, PL lifetime, and infrared photocurrent, were performed on an erbium implanted silicon *p-n* junction in order to investigate the energy transfer processes between the silicon electronic system and the Er 4f energy levels. The device features excellent light trapping properties due to a textured front surface and a highly reflective rear surface. The PL intensity and PL lifetime measurements show weak temperature quenching of the erbium intra-4f transition at 1.535 μm for temperatures up to 150 K, attributed to Auger energy transfer to free carriers. For higher temperatures, much stronger quenching is observed, which is attributed to an energy backtransfer process, in which Er de-excites by generation of a bound exciton at an Er related trap. Dissociation of this exciton leads to the generation of electron-hole pairs that can be collected as a photocurrent. In addition, non-radiative recombination takes place at the trap. It is shown for the first time that all temperature dependent data for PL intensity, PL lifetime, and photocurrent can be described using a single model. By fitting all temperature dependent data simultaneously, we are able to extract the numerical values of the parameters that determine the (temperature dependent) energy transfer rates in erbium doped silicon. While the external quantum efficiency of the photocurrent generation process is small (1.8×10^{-6}) due to the small erbium absorption cross section and the low erbium concentration, the conversion of Er excitations into free *e-h* pairs occurs with an efficiency of 70% at room temperature.

5.1 Introduction

Erbium doped silicon is an interesting material, in which energy transfer can take place between the semiconductor electronic system and the internal 4f states of the rare earth ion.¹⁻⁷ Previously, this material has mainly been studied because it provides a means to attain light emission from silicon, a phenomenon that is of great importance in Si-based opto-electronic technology. Indeed, room temperature photoluminescence (PL) from Er doped silicon has been reported, and room temperature light emitting diodes have been fabricated.⁸⁻¹⁰ The excitation mechanism of Er in Si can be described in terms of an impurity Auger excitation process as indicated schematically in Fig. 5.1. Electron-hole ($e-h$) pairs, generated either optically or electrically, can be trapped at an Er related defect level (W_T in Fig. 5.1). Subsequently, the $e-h$ pair can recombine and energy is transferred to the Er ion (W_E in Fig. 5.1), which then becomes excited from the ground state ($^4I_{15/2}$) to the first excited state ($^4I_{13/2}$). The Er may then decay (W_0 in Fig. 5.1) by the emission of a photon with a wavelength of 1.54 μm .

It is well known that the photo- and electroluminescence from Er in Si both decrease strongly ("quench") as the temperature is increased.^{2,5,6,8} Two quenching mechanisms have been identified. First, at temperatures typically above 30 K, Auger quenching takes place,⁴ in which an excited Er ion is de-excited by energy transfer to a free electron or hole ($W_{A,e}$ and $W_{A,h}$ in Fig. 5.1). The strength of this process depends on the free carrier concentration, which in turn depends on the dopant concentration and the temperature. Second, at temperatures typically above 150 K a much stronger quenching process becomes significant, which is attributed to an energy backtransfer process characterized by a rate constant W_{BT} as shown in Fig. 5.1. In this process an excited Er ion decays by generation of an $e-h$ pair bound at an Er related trap. This backtransfer process is the reverse of the excitation process W_E depicted in Fig. 5.1. Once the bound $e-h$ pair is formed, it can recombine and re-transfer its energy to the Er ion or it can dissociate, either by absorption of a photon or by absorbing energy from lattice vibrations, leading to the generation of a free electron hole pair (rate constant W_D in Fig. 5.1).

At present this energy backtransfer mechanism from an excited Er ion to the Si electronic system limits the room temperature performance of erbium doped silicon photo- and electroluminescence devices. On the other hand, the backtransfer process may also be used in an advantageous way, namely to detect infrared light in silicon. Normally, silicon only weakly absorbs infrared light at photon energies below the bandgap at 1.1 eV.¹¹ However, if the silicon is doped with Er, 1.54 μm photons may be absorbed by the Er, which in turn can generate free carriers via the backtransfer process as described above, followed by the dissociation process. If the Er is located in or near the depletion region of a $p-n$ junction these free carriers generate a current, an effect known as the impurity photovoltaic effect. Early demonstrations of an Er related photocurrent can be found in Refs. 6, 12, and 13, in which Si $p-n$ junctions show an enhanced photoresponse around 1.53 μm as a result

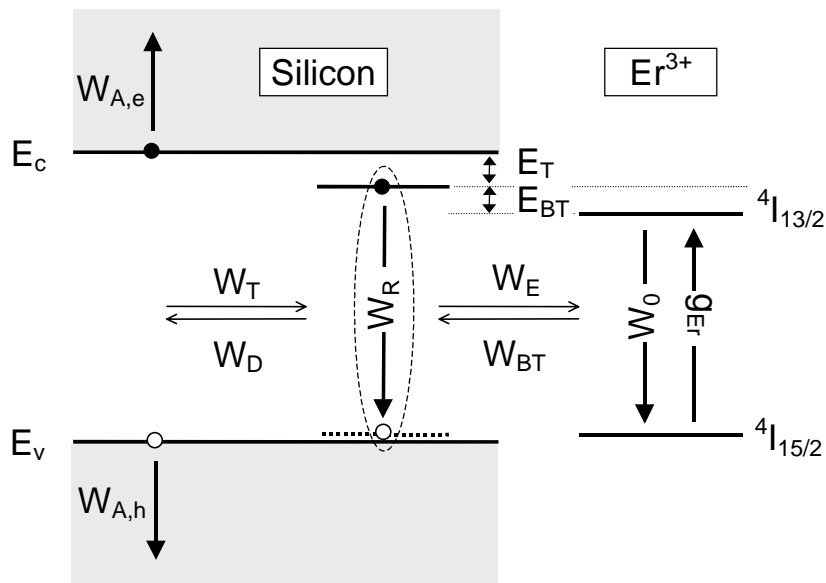


Figure 5.1. Energy transfer processes in Er doped silicon. Optically generated carriers in Si can be trapped at an Er related trap level in the Si bandgap. The bound exciton may then recombine and transfer its energy to the Er^{3+} ion, which can then emit a photon at 1.535 μm . In the reverse process, an optically excited Er ion decays by the creation of a bound exciton, which can then dissociate resulting in the generation of a free electron-hole pair. In a p - n junction geometry these carriers can be collected leading to a net photocurrent at 1.534 μm . Exciton recombination at the Er related trap is also included.

of Er doping. Based on this process, Er doping of silicon may be used to improve the efficiency of Si-based solar cells or to fabricate Si-based infrared detectors.

Although all processes in Fig. 5.1 are known, little is known about their relative importance. In particular, the parameters W_E , W_R , as well as the absorption cross section of Er in Si ($\sigma_{1.535}$) which are all needed to predict the quantum efficiency of an Er doped p - n junction, are not known. In this chapter, we perform a quantitative study of all excitation and de-excitation processes in Er doped Si. Temperature dependent measurements of the 1.54 μm PL intensity, PL lifetime and photocurrent are performed on an erbium implanted Si p - n junction. By comparing the data with calculations using a rate equation model that takes into account all energy transfer processes as depicted in the model of Fig. 5.1 the energy transfer rates and activation energies are derived. It is found that after optical excitation of the Er, the generation of free carriers that can be collected (i.e. backtransfer followed by exciton dissociation) occurs with an efficiency of 70% at room temperature. At 300 K, the rate limiting step in this process is the backtransfer. All these measurements were only possible because of the use of a specially textured solar cell geometry, in which enhanced light trapping significantly enhanced the

effective optical excitation rate of Er ions in the p - n junction. Finally, the implications of this work for solar cell and infrared detector technology are addressed.

5.2 Experiment

A 200 μm thick float zone grown silicon (100) wafer (B doped, resistivity 2.5 Ωcm) was processed for the fabrication of a passivated-emitter rear-locally-diffused (PERL) solar cell¹² at the University of New South Wales. To enhance the light trapping in the cell, the wafer top surface was textured by anisotropic etching, yielding square based inverted pyramids with facets inclined at 55° from the sample normal. Next, 3.5 MeV Er ions were implanted into the textured surface layer to a total fluence of 1×10^{13} ions/ cm^2 . The emitter region was formed by surface doping with phosphorous, carried out from a gas source in a tube furnace, followed by thermal annealing at 835 $^\circ\text{C}$ and two oxidation steps at 1030 $^\circ\text{C}$ for 60 min. and 1000 $^\circ\text{C}$ for 75 min. During these high temperature processes most of the damage generated during implantation was annealed out. The surface P concentration after annealing was 1×10^{19} ions/ cm^3 , with the emitter region extending to a depth of 0.7 μm , measured normal to the facets. The Er projected range and straggle are 1.0 μm and 0.2 μm respectively. The mean implant range normal to the facets then is 0.6 μm , placing Er near the junction region of the cell. Part of Er will therefore be located in the space charge region of the junction, while the remaining Er will be located in the emitter and base regions of the cell.

Current-voltage measurements on the Er implanted PERL cell show an open circuit voltage of 0.664 V, a fill factor of 0.74 and an efficiency of 19.2% under AM1.5 illumination. This is lower than the typical efficiency for standard PERL cells, which is attributed to carrier recombination at defect levels caused by remaining ion implantation damage. The cell was placed in a closed cycle helium cryostat using silver paint to ensure good electrical and thermal contact. Infrared photocurrent measurements were done in short circuit condition using a tunable solid state laser diode with a wavelength ranging from 1.50 μm to 1.58 μm at a power of typically 1 mW, and spectral resolution of 0.01 nm. The area of the laser spot on the sample was 1.5 cm^2 . In the same setup, the 1.54 μm photoluminescence resulting from excitation with the 515 nm line of an Ar ion laser was measured. A grating monochromator was used in combination with a liquid nitrogen cooled Ge detector and phase sensitive detection techniques. The spectral resolution was 6 nm. The $1/e$ PL lifetime was measured by modulating the pump beam *on-off* and recording the time dependent luminescence signal on a digital oscilloscope.

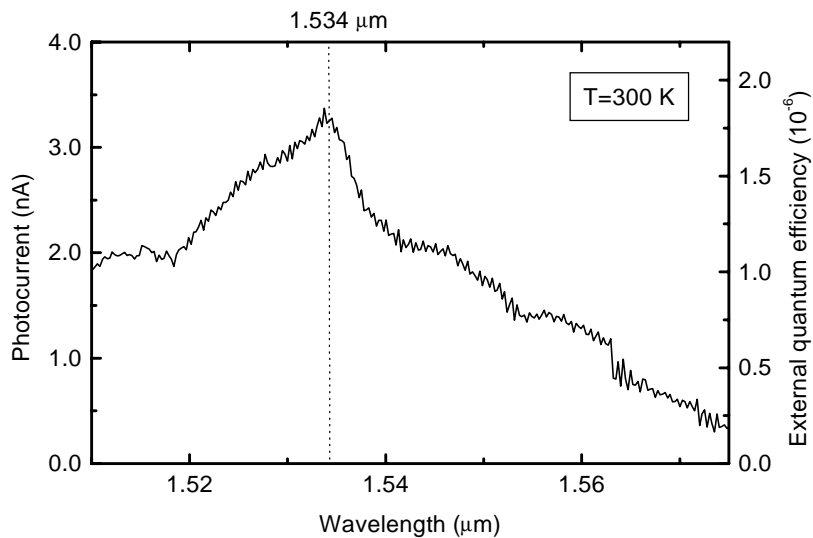


Figure 5.2. Photocurrent spectrum of a PERL Si solar cell implanted with Er at 3.5 MeV to a fluence of 1×10^{13} ions/cm². An external quantum efficiency scale is provided on the right hand side.

5.3 Results

Figure 5.2 shows an infrared photocurrent spectrum measured on the textured PERL solar cell at 300 K under 1.5 mW irradiation. The spectrum displays the characteristic features of an Er absorption spectrum peaking around 1.534 μm . The short circuit current at 300 K was 3.3 nA at 1.534 μm . The external quantum efficiency, defined as the number of collected $e-h$ pairs per incoming photon, thus is 1.8×10^{-6} at 1.534 μm . Note that due to the textured top surface and the highly reflective backside of the PERL cell, each incoming photon experiences multiple internal reflections and will therefore pass several times through the Er doped region. In fact, similar experiments on untextured Si solar cells showed a photocurrent at 1.534 μm at 300 K of only 0.5 nA, seven times lower than the PERL cell. At this low current the signal-to-noise ratio was too poor to measure the temperature dependence of the photocurrent of this planar cell such as will be shown below for the PERL cell.

Figure 5.3 shows the temperature dependence of the photocurrent at 1.534 μm , plotted in an Arrhenius graph. It can clearly be seen that the photocurrent increases over nearly two orders of magnitude, as the temperature is increased from 100 K to 300 K. Also plotted in Fig. 5.3 is the photoluminescence at 1.535 μm measured on the same sample, under 515 nm excitation. Three distinct temperature regions can be identified for the PL intensity as a function of temperature: I) a temperature independent region below 30 K, II) a weakly temperature dependent region between

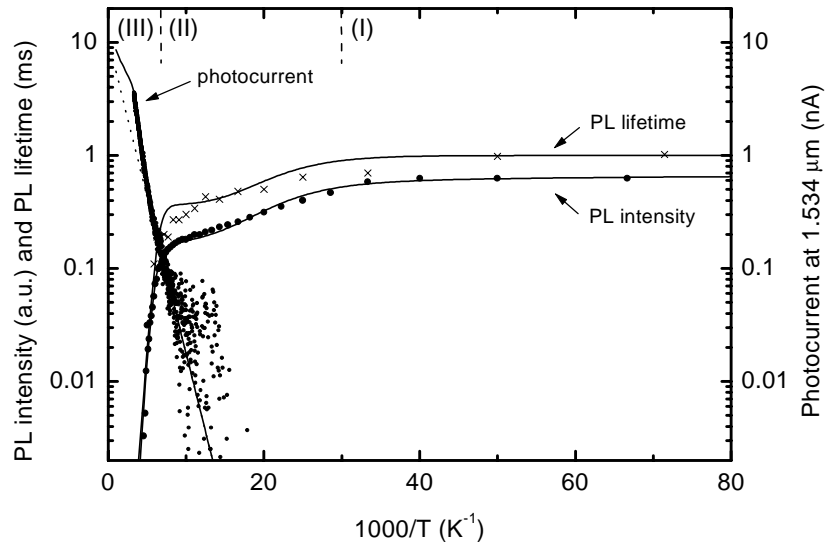


Figure 5.3. Temperature-dependent photocurrent at 1.534 μm , measured on the Er implanted PERL cell. The temperature dependence of photoluminescence intensity and PL lifetime at 1.535 μm excited by 515 nm light are also included. Three quenching regimes are indicated, and are labeled (I), (II), and (III). The drawn lines are fits of the model, using the parameters in Table 5.1.

30 K and 150 K, and III) a strongly temperature dependent decrease of the intensity above 150 K. Figure 5.3 also shows the temperature dependence of the PL lifetime at 1.535 μm , which shows the same trend as the PL intensity. Note that a measurable photocurrent is only observed in the temperature range where both PL intensity and PL lifetime show strong temperature quenching.

Spectral photocurrent measurements at temperatures below 150 K show a small signal, not related to Er, most likely due to implantation induced defects in the p - n junction. Indeed it has been shown that implantation damage induces an infrared photoresponse in silicon solar cells.¹² The observed defect current can be described by an activated process, with an activation energy of 55 meV as indicated by the dotted line in Fig. 5.3.

5.4 Energy transfer processes

In order to calculate and predict the temperature dependence of the PL intensity and PL lifetime as well as the photocurrent, the following five processes must be taken into account.

5.4.1 Optical absorption and emission ($\sigma_{1.535}$)

The Er^{3+} emission cross section is temperature dependent, due to changes in the thermal distribution over the Stark levels in the excited state manifold of Er^{3+} as the

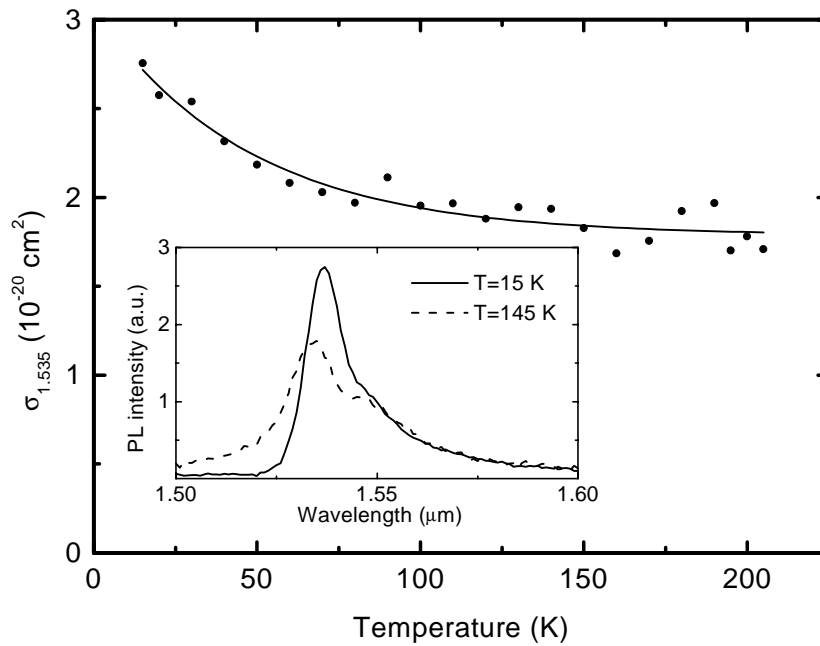


Figure 5.4. Temperature dependence of the Er emission cross section at 1.535 μm , derived from PL spectra such as shown in the inset (taken at 15 K and 145 K). The drawn line through the data is described by Eq. (1)

temperature is increased. This can be seen by comparing the normalized PL emission spectra taken at 15 K and 145 K, shown in the inset in Fig. 5.4. This effect must be included in the analysis of both the infrared photocurrent and of the photoluminescence data.

From the shape of the PL spectra, the optical emission cross section of Er in Si can be calculated,¹⁴ assuming that the measured PL lifetime at 15 K (1.0 ms, see Fig. 5.3) is equal to the radiative lifetime of Er in Si. From such a calculation, using the PL spectrum taken at 15 K, it follows that the emission cross section at 15 K at 1.535 μm ($\sigma_{1.535}$) equals $2.7 \times 10^{-20} \text{ cm}^2$.

The temperature dependence of the Er emission cross section at 1.535 μm can be determined by taking normalized measurements of the integrated PL emission spectrum as a function of temperature, as shown in Fig. 5.4. The drawn line is a smooth fit through the data described by the following equation:

$$\sigma_{1.535}(T)(10^{-20} \text{ cm}^2) = 1.8 + 1.2 \exp(-0.02 \times T(\text{K})). \quad (1)$$

From the McCumber reciprocity formula^{15,16} it follows that the temperature dependence of the absorption cross section is similar to that of the emission cross section at the location of the emission peak. Experimentally, it is generally observed that the magnitude of the absorption cross section at this wavelength is close to the

emission cross section. The rate constant for optical excitation of Er under 1.534 μm illumination is then given by:

$$g_{Er} = (1 - R)L_{eff}\sigma_{1.535}\phi, \quad (2)$$

with ϕ the photon flux ($\text{cm}^{-2}\text{s}^{-1}$), R the reflectivity of the cell around 1.535 μm (taken equal to zero), and L_{eff} the effective number of light passes through the depletion region. The rate constant g_{Er} is defined as the probability per unit time that an Er ion in the ground state is optically excited.

5.4.2 Auger quenching ($W_{A,e}$, $W_{A,h}$)

An excited Er ion can decay by Auger energy transfer to free carriers. Such carriers are provided by the P doping in the emitter region of the cell, the B doping of the Si substrate, and by the Er ions which can act as a donor in Si.¹⁷ The Auger quenching effect causes a decrease in the PL lifetime and in the luminescence intensity, but does not generate free $e-h$ pairs. The Auger quenching rate constant to free electrons in erbium doped silicon containing a donor concentration N_D (cm^{-3}) is given by:

$$W_{A,e}(T) = C_{A,e}N_D \left(1 + 2 \exp\left(-\frac{E_d - E_F}{kT}\right) \right)^{-1}, \quad (3)$$

where $C_{A,e}$ ($\text{cm}^{-3}\text{s}^{-1}$) is the Auger quenching coefficient for free electrons, E_d the donor ionization energy, and E_F the Fermi energy. For Auger quenching to free holes ($W_{A,h}$) a similar relation holds. The Auger quenching coefficient for Er in Si has recently been measured by Priolo *et al.*⁵ and amounts to $5 \times 10^{-13} \text{ cm}^3\text{s}^{-1}$ for both electrons and holes. In the fitting procedure we vary N_D and E_d , while the Fermi energy as a function of temperature is numerically determined.

5.4.3 Er excitation and backtransfer (W_E , W_{BT})

Erbium can be excited by recombination of a trapped $e-h$ pair at an Er related defect level in the Si bandgap (see Fig. 5.1). The temperature independent rate constant for this process is denoted as W_E . Conversely, an excited Er ion can decay non-radiatively by the formation of such a trapped $e-h$ pair. The temperature dependence of the backtransfer process may be described either by a single activation barrier or by a phonon-assisted process.¹⁸ In both cases, the rate constant for energy backtransfer becomes:

$$W_{BT}(T) = W_E \exp\left(-\frac{E_{BT}}{kT}\right). \quad (4)$$

Measurements of the Er luminescence quenching in Er doped silicon have indicated a typical backtransfer energy of 150 meV at temperatures above 100 K.^{3,4} As the bandgap of silicon decreases by 45 meV upon going from 15 K to 300 K,¹⁹ the trap energy will most likely be temperature dependent. The depth of the trap as a function of temperature is assumed to show the same relative variation as the silicon bandgap.

5.4.4 Electron-hole pair trapping and dissociation (W_D , W_T)

The rate constant for carrier trapping at an Er related trap is given by $W_T = \sigma_T v_{th} N_T$, with σ_T a temperature independent carrier trapping cross section, v_{th} the carrier thermal velocity given by $(3kT/m_{e,h})^{1/2}$, and N_T (cm^{-3}) the trap density, which we assume to be equal to the Er density. Once an $e-h$ pair is trapped, it can recombine and excite the Er ion, or it can dissociate with an activation energy E_T , generating a free electron hole pair. Inside the depletion region these carriers are immediately separated by the built-in electric field ($\sim 10^4$ V/cm). Assuming that photon assisted dissociation is negligible at the low applied photon flux ($5 \times 10^{15} \text{ cm}^{-2} \text{ s}^{-1}$), the rate constant for the $e-h$ pair dissociation process is given by

$$W_D(T) = \sigma_T v_{th} N_c \exp\left(-\frac{E_T}{kT}\right). \quad (5)$$

The dissociation energy E_T is given by the temperature dependent difference between the trap energy and the conduction band energy. The description of backtransfer and detrapping imposes that the total energy of the thermal processes leading to free carrier generation corresponds to the silicon bandgap: $E_{Er} + E_{BT} + E_T = E_g$, with E_{Er} the energy of the Er intra-4f transition (809 meV) and E_g the temperature dependent bandgap of Si.

5.4.5 Carrier recombination at the Er related trap level

The Er PL intensity is found to quench strongly at temperatures above 150 K. The PL lifetime seems to follow this behavior, although the PL intensity quickly becomes too low to determine the PL lifetime. This type of PL lifetime quenching is generally observed for Er doped silicon,^{2,5,6} showing that at these temperatures a large fraction of the Er decay is occurring non-radiatively. If these non-radiative events are generating current, the infrared photocurrent should saturate already well below 300 K. The fact that no such saturation is observed (see Fig. 5.3) implies that the initial PL lifetime quenching at temperatures around 150 K is due to non-radiative decay processes that do not generate free $e-h$ pairs. To account for this effect, an additional recombination process must be included in the model of Fig. 5.1, of which the associated rate constant is denoted as W_R . This is an important observation, since this recombination process has not been included in any of the previous models^{3,5} to describe the temperature dependence of the Er related PL in

Si. As no PL is observed at the energy characteristic for this transition (0.96 eV; 1.3 μm), it must be assumed that this recombination occurs non-radiatively.

5.5 Comparison between model and experiment

5.5.1 Photoluminescence rate equations

In PL measurements, the Er is excited through optically generated carriers (see Fig. 5.1). In the depletion region, these carriers are immediately swept away, which means that the PL signal mostly reflects Er located in the B-doped (p-type) base region of the cell. We will assume that a fixed fraction of the generated minority carriers is captured at the Er related trap, resulting in a temperature independent trapped $e-h$ pair generation rate, with a rate constant g_{eh} . The concentration of trapped electron hole pairs N_{eh} (cm^{-3}) and excited Er ions N_{Er}^* (cm^{-3}) resulting from this excitation are then determined by the following coupled rate equations:

$$\frac{\partial N_{eh}}{\partial t} = g_{eh} + W_{BT} N_{Er}^* - (W_E + W_D + W_R) N_{eh}, \quad (6)$$

$$\frac{\partial N_{Er}^*}{\partial t} = W_E N_{eh} - (W_0 + W_A + W_{BT}) N_{Er}^*. \quad (7)$$

5.5.2 Photoresponse rate equations

In the case of photocurrent measurements, the Er ions are excited directly by 1.534 μm light, at a rate g_{Er} . Moreover, as the photocurrent is primarily generated by Er located within the depletion region, Auger quenching to free carriers is expected to be negligible. The rate equations then become:

$$\frac{\partial N_{eh}}{\partial t} = W_{BT} N_{Er}^* - (W_E + W_D + W_R) N_{eh}, \quad (8)$$

$$\frac{\partial N_{Er}^*}{\partial t} = g_{Er} N_{Er} + W_E N_{eh} - (W_0 + W_{BT}) N_{Er}^*. \quad (9)$$

Both sets of differential equations were solved analytically for steady state conditions.

5.5.3 Model calculations

All experimental data in Fig. 5.3 can be described as a function of temperature by solving Eqs. 6-9: the photocurrent is given by $qN_{eh}(T) \times W_D(T) \times V \times \eta_{coll}$ with q the electron charge, V the illuminated volume of the depletion region, and η_{coll} the carrier collection efficiency, which for visible radiation was measured to be ~ 1 for

all temperatures probed, the PL intensity is proportional to $\sigma_{I.535}(T) \times N_{Er}^*(T)$, and the photoluminescence lifetime is to first order given by:

$$\tau_{PL}(T) = [W_0(T) + W_A(T) + W_{BT}(T)]^{-1}. \quad (10)$$

Figure 5.3 includes calculations of the photoluminescence intensity, the photoluminescence lifetime, and photocurrent as a function of temperature, using the parameters listed in Table 5.1. All parameters were derived by fitting the experimental data in Fig. 5.3 and 5.4, except for the backtransfer energy, which was taken from Ref. 6 and the Auger quenching coefficient, that was taken from Ref. 5. In the calculations it is assumed that all implanted Er can contribute to the photocurrent.

Figure 5.3 shows that as the temperature is increased to 100 K the Er photoluminescence lifetime and intensity decrease slightly with temperature, due to Auger quenching. This effect does not lead to the generation of free carriers, and hence the Er related photocurrent is negligible in this temperature range. At higher temperatures (above 150 K) backtransfer sets in, leading to a further decrease of the luminescence lifetime and intensity. As the temperature increases, the $e-h$ pair dissociation W_D starts to be competitive with $e-h$ pair recombination occurring at the Er related trap level (W_R). The dissociation process generates free carriers in and near the depletion region that can be collected, leading to the buildup of a

parameter	symbol	value	source
Er areal density	N_{Er}	$1 \times 10^{13} \text{ cm}^{-2}$	this work
photon flux	ϕ	$7.7 \times 10^{15} \text{ cm}^{-2} \text{ s}^{-1}$	this work
Si indirect bandgap (15 K-300 K)	E_g	1.168 - 1.123 eV	Ref. 19
Er absorption / emission cross section (15 K)	$\sigma_{I.535}$	$2.7 \times 10^{-20} \text{ cm}^2$	this work, Fig. 5.4
Er radiative decay rate	W_0	$1.0 \times 10^3 \text{ s}^{-1}$	this work, Fig. 5.3
backtransfer pre-factor	W_E	$2 \times 10^8 \text{ s}^{-1}$	this work (fitted)
backtransfer activation energy (150 K)	E_{BT}	150 meV	Refs. 3,4
carrier trapping cross section	σ_T	$3 \times 10^{-15} \text{ cm}^2$	set
dissociation activation energy (150 K)	E_T	199 meV	set at $E_g - (E_{BT} + E_{Er})$
Auger quenching constant	C_A	$5 \times 10^{-13} \text{ cm}^3 \text{ s}^{-1}$	Ref. 5
Auger quenching activation energy	$E_{A,h}$	30 meV	this work (fitted)
dopant concentration	N_D	$3.5 \times 10^{15} \text{ cm}^{-3}$	this work (fitted)
trap recombination rate	W_R	$2 \times 10^8 \text{ s}^{-1}$	this work (fitted)
light trapping \times collection efficiency	$L_{eff} \eta_{coll}$	9	this work (fitted)

Table 5.1. Input parameters for the model used to calculate the PL intensity, PL lifetime, and photocurrent data in Fig. 5.3.

rates (s ⁻¹)	symbol	15 K	300 K
radiative decay rate	W_0	1.0×10^3	1.0×10^3
free carrier Auger quenching rate	W_A	~ 0	1.7×10^3
backtransfer rate	W_{BT}	~ 0	1.7×10^6
trap dissociation rate	W_D	~ 0	5.2×10^8
trap recombination rate	W_R	2×10^8	2×10^8

Table 5.2. Comparison of the various rates in the model of Fig. 5.1, calculated from the steady state solution of the rate equation model, using input parameters listed in Table 5.1. Results are shown for 15 K and 300 K.

measurable photocurrent. Finally, when W_D becomes larger than W_R , the Er related photocurrent is expected to saturate. This effect can be seen in Fig. 5.3 as a change in the slope of the calculated current at high temperatures.

In fitting the data, it was found that the values for the parameters σ_T , W_R , and W_E are correlated. In order to reproduce PL lifetime quenching above 150 K, the backtransfer rate has to become significant compared to the Er radiative lifetime, and consequently the prefactor W_E has to be larger than $\sim 10^7$ s⁻¹. Furthermore, in order to observe PL lifetime quenching the backtransfer has to be followed by either $e-h$ pair dissociation (scaling with σ_T) or recombination at the Er related trap (W_R). The observation that the photocurrent has not yet saturated at room temperature implies that the $e-h$ pair dissociation is limiting the current generation, and backtransfer followed by recombination at the Er related trap (W_R) is causing the initial PL lifetime quenching. Within these constraints for σ_T , W_R , and W_E , similar fits can be obtained with either a low W_E and a high W_R or a high W_E and a low W_R .

The absolute slope of the photocurrent data near room temperature in Fig. 5.3 corresponds to an activation energy that is lower than the backtransfer energy and the dissociation energy. In order to reproduce this behavior, the current generation process must approach saturation near room temperature. This means that at room temperature $e-h$ pair dissociation (W_D) is competitive with recombination at the Er related trap, which determines the ratio σ_T/W_R . Electron capture cross sections in Si are typically in the range 10^{-14} - 10^{-16} cm². For the fits in Fig. 5.3 we have chosen $\sigma_T = 3 \times 10^{-15}$ cm².

In order to obtain the correct absolute value of the room temperature photocurrent, the product $L_{eff} \times \eta_{coll}$ was found to be 9. Assuming $\eta_{coll} \approx 1$, this implies that the number of internal reflections is 9, which is a reasonable value for a PERL cell.¹¹ For a good description of the Auger quenching up to 100 K, a dopant concentration of 3.5×10^{15} cm⁻³ was found, which is in correspondence with the B doping level in the base region of the cell. The ionization energy was found to be 30 meV, which is smaller than that of boron in Si (45 meV), which may be

attributed to the donor behavior of Er itself,^{17,20} or to the presence of a potential gradient near the edge of the depletion region.

Table 5.2 lists various energy transfer rates calculated at 15 K and 300 K. As can be seen the backtransfer rate constant increases from a negligible value at 15 K to $1.7 \times 10^6 \text{ s}^{-1}$ at 300 K. The dissociation rate constant increases from a negligible value at 15 K to $5.2 \times 10^8 \text{ s}^{-1}$ at 300 K. At 300 K the dissociation rate constant is more than two orders of magnitude larger than the backtransfer rate constant, and more than a factor two larger than the recombination rate constant (W_R), showing that the photocurrent is approaching saturation. Note that the backtransfer rate constant at 300 K is much larger than the radiative rate constant ($1 \times 10^3 \text{ s}^{-1}$) and the free carrier Auger quenching rate constant ($6.5 \times 10^3 \text{ s}^{-1}$). From the data it can be calculated that at 300 K, the excited Er ions generate free carriers that can be collected with an efficiency of 70%.

5.6 Implications for solar cell and infrared detector design

As demonstrated above, the internal quantum efficiency due to backtransfer at 300 K is calculated to be 70%, *i.e.* once a $1.54 \text{ }\mu\text{m}$ photon is absorbed by an Er^{3+} ion, the probability that it leads to the generation of an $e-h$ pair that can be collected is 70%. The external quantum efficiency, defined as the number of $e-h$ pairs collected per incoming photon, derived from the photocurrent data amounts to 1.8×10^{-6} at 300 K. This number is low due to the small absorption cross section of the Er^{3+} ions, combined with the relatively low Er concentration in the sample. In order to have a significant effect on the infrared response of a Si solar cell, the Er concentration in the cell must be significantly increased, or the interaction length of the light with the Er should be strongly enhanced.

In the latter respect it is interesting to note the possibility to use Er doped Si in a waveguide detector geometry, in which the light path can be of centimeter length, rather than the micrometer range in the PERL cell discussed in this chapter. Experiments on the photoresponse of such Er doped Si infrared waveguide detectors are described in Chapter 6. The maximum time response for such a detector at room temperature is given by the slowest of the backtransfer and trap dissociation rates. From Table 5.2 it follows that this is equal to $1.7 \times 10^6 \text{ s}^{-1}$ at room temperature. Detectors with such a response time could e.g. find applications in all-optical interconnects used to electrically isolate the driver circuits from Si based high power diodes and transistors, which typically operate at frequencies of 10 kHz.

5.7 Conclusions

PL intensity, PL lifetime, and infrared ($\lambda \approx 1.5 \text{ }\mu\text{m}$) photocurrent measurements have been performed on an Er implanted $p-n$ junction in the temperature range 15 K - 300 K. All data can be fitted using a model for the energy transfer processes in Er

doped silicon that is centered around an Er related trap that mediates the energy transfer between the Si electronic system and the Er 4f energy levels. The temperature dependent excitation transfer rates and energies are determined, and it is found that non-radiative recombination at the trap must be included in the model. A significant photocurrent is measured from the junction around 1.535 μm , which is attributed to energy transfer from optically excited Er to the Si electronic system. The efficiency of this process at room temperature is 70%. Such energy conversion processes may be useful in Si solar cells and infrared detector technology once the Er concentration or light path length can be significantly increased.

References

- ¹ J. Michel, J. L. Benton, R. F. Ferrante, D. C. Jacobson, D. J. Eaglesham, E. A. Fitzgerald, Y.-H. Xie, J. M. Poate, and L. C. Kimerling, *J. Appl. Phys.* **70**, 2672 (1991)
- ² S. Coffa, G. Franzò, F. Priolo, A. Polman, and R. Serna, *Phys. Rev. B* **49**, 16313 (1994)
- ³ F. Priolo, G. Franzò, S. Coffa, A. Polman, S. Libertino, R. Barklie, and D. Carey, *J. Appl. Phys.* **78**, 3874 (1995)
- ⁴ J. Palm, F. Gan, B. Zheng, J. Michel, and L. C. Kimerling, *Phys. Rev. B* **54**, 17603 (1996)
- ⁵ F. Priolo, G. Franzò, and S. Coffa, and A. Carnera, *Phys. Rev. B* **57**, 4443 (1998)
- ⁶ P. G. Kik, M. J. A. de Dood, K. Kikoin, and A. Polman, *Appl. Phys. Lett.* **70**, 1721 (1997), Chapter 4 of this thesis
- ⁷ I. Tsimperidis, T. Gregorkiewicz, H. H. P. Th. Bekman, C. J. G. M. Langerak, *Phys. Rev. Lett.* **81**, 4748 (1998)
- ⁸ G. Franzò, F. Priolo, S. Coffa, A. Polman, and A. Carnera, *Appl. Phys. Lett.* **64**, 2235 (1994)
- ⁹ B. Zheng, J. Michel, F. Y. G. Ren, L. C. Kimerling, D. C. Jacobson, and J. M. Poate, *Appl. Phys. Lett.* **64**, 2842 (1994)
- ¹⁰ J. Stimmer, A. Reittinger, J. F. Nützel, G. Abstreiter, H. Holzbrecher, and C. Buchal, *Appl. Phys. Lett.* **68**, 3290 (1996)
- ¹¹ *Silicon Solar Cells*, M. A. Green (University of New South Wales, Sydney, 1995)
- ¹² M. J. Keevers, F. W. Saris, G. C. Zhang, J. Zhao, M. A. Green, and R. Elliman, Proceedings of the 13th European Photovoltaic Solar Energy Conference, Nice, October 1995, p.1215
- ¹³ J. Michel, B. Zheng, J. Palm, E. Ouellette, and L. C. Kimerling, *Mat. Res. Soc. Symp. Proc.* **422**, 317 (1996)
- ¹⁴ D. E. McCumber, *Phys. Rev.* **134**, A299 (1964)
- ¹⁵ D. E. McCumber, *Phys. Rev.* **136**, A954 (1964)
- ¹⁶ W. J. Miniscalco, *J. Lightwave Technol.* **9**, 234 (1991)
- ¹⁷ J. L. Benton, J. Michel, L. C. Kimerling, D. C. Jacobson, Y.-H. Xie, D. J. Eaglesham, E. A. Fitzgerald, and J. M. Poate, *J. Appl. Phys.* **70**, 2667 (1991)
- ¹⁸ A. Taguchi and K. Takahei, *J. Appl. Phys.* **83**, 2800 (1998)
- ¹⁹ C. D. Thurmond, *J. Electrochem. Soc. (USA)* **122**, 1133 (1975)
- ²⁰ F. Priolo, S. Coffa, G. Franzò, C. Spinella, A. Carnera, and V. Bellani, *J. Appl. Phys.* **74**, 4936 (1993)

Chapter 6

Quantum efficiency of an Er doped waveguide detector in silicon operating at 1.54 μm

A new concept for an Er doped waveguide detector in silicon is introduced. The detector structure can be fabricated using silicon-on-insulator material, and consist of an Er doped p - n junction located in the core of a silicon ridge waveguide. The detection scheme relies on the optical absorption of 1.54 μm light by the Er^{3+} ions in the waveguide core, followed by an efficient electron-hole pair generation by the excited Er and subsequent carrier separation by the electric field of the p - n junction. By performing optical mode calculations and including realistic doping profiles, we show that an external quantum efficiency of 10^{-3} can be achieved in a 4 cm long waveguide detector fabricated using standard silicon processing. The quantum efficiency of the detector is mainly limited by free carrier absorption in the waveguide core, and may be further enhanced by optimizing the electrical doping profiles. Preliminary photocurrent measurements on an Er doped Si waveguide detector at room temperature show an Er related photocurrent at 1.54 μm .

6.1 Introduction

Silicon is an ideal material for the fabrication of optical waveguides that are compatible with optical telecommunication technology at 1.5 μm , because of its high transparency and high refractive index at this wavelength. The high transparency is due to the large mismatch between the 1.5 μm photon energy (0.8 eV) and the silicon bandgap energy (1.1 eV at room temperature). The energy mismatch also excludes the fabrication of all-silicon active waveguide devices such as detectors and emitters operating at 1.5 μm . This problem may be solved by doping the silicon with small amounts of erbium (Er). In silicon, the rare earth ion Er^{3+} can be electrically excited and subsequently emit 1.54 μm light due to an

electronic transition in its incompletely filled $4f$ shell, as was shown in Chapters 4 and 5. Er doped LEDs in Si operating at $1.54 \mu\text{m}$ have been made, with a quantum efficiency of up to 10^{-4} at room temperature.¹⁻³ In Chapter 5 it was shown that an Er doped Si p - n junction can generate a photocurrent when illuminated with $1.54 \mu\text{m}$ light. This effect allows the fabrication of a silicon photodetector that is sensitive at $1.54 \mu\text{m}$.⁴

The Er related photoresponse at $1.54 \mu\text{m}$ is caused by an interaction between the Er ion and the Si matrix. When Er in Si is optically excited into the first excited state, it can de-excite and generate a localized electron-hole (e - h) pair, which then dissociates thermally. If this process occurs near the depletion region of a p - n junction, the generated charge carriers produce a photocurrent. As was shown in the previous chapter, excited Er can generate electron-hole pairs with a high efficiency at room temperature (70%). However, due to the small optical absorption cross section of the Er ions and the limited width of the depletion region, the fraction of the light that is absorbed at normal incidence on such a p - n junction is very small ($\sim 10^{-7}$). To improve the absorption efficiency, a high Er concentration and a large interaction length are required. The maximum concentration of Er soluble in Czochralski grown silicon⁵ is $\sim 10^{18} \text{ cm}^{-3}$. It can be further enhanced by co-doping with impurities such as oxygen.^{6,7} The interaction length of the light with the Er doped junction can be increased by using a waveguide geometry, in which the p - n junction extends over the full length of the waveguide. In this chapter we will describe the effects that determine the performance of such a waveguide detector, and calculate the quantum efficiency that can be achieved. Finally, preliminary measurements of the photoresponse of such an Er doped Si p - n junction waveguide detector are presented.

6.2 Device layout

Figure 6.1 shows a possible waveguide detector structure. The device is based on commercially available silicon-on-insulator (SOI) material, consisting of a thin crystalline Si top layer separated from a thick Si substrate by an SiO_2 layer. In this material, light can be confined in the high refractive index Si top layer ($n_{1.54}=3.5$) by total internal reflection at the interface with air ($n_{1.54}=1.0$) and with the SiO_2 layer ($n_{1.54}=1.44$), provided that the SiO_2 is sufficiently thick to avoid coupling to the Si substrate. Lateral confinement is achieved by etching a ridge structure in the Si top layer (see Fig. 6.1). A ridge width of $10 \mu\text{m}$ and an etch depth of $2 \mu\text{m}$ are chosen, ensuring good optical mode confinement. The center of the waveguide is doped with Er. A p - n junction is formed near the waveguide center by means of a shallow boron implant into the n -type Si layer. This also generates the p^+ region required for good electrical contact. The n^+ (P doped) side contacts are located $10 \mu\text{m}$ away from the waveguide core. Electrical contact is made via metal stripe contacts running along the n^+ and p^+ regions, as indicated in Fig. 6.1.

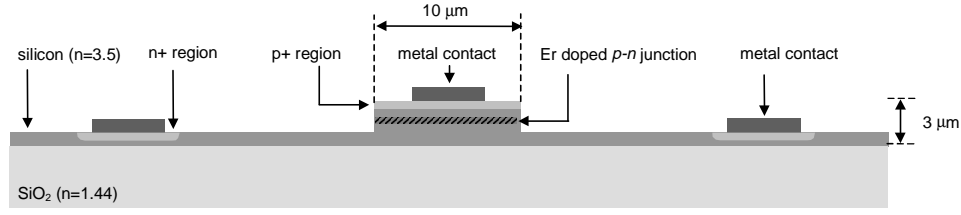


Figure 6.1. Schematic cross section of an Er doped waveguide detector in Si.

6.3 Contributions to the external quantum efficiency

The external quantum efficiency η_{ext} of the detector structure shown in Fig. 6.1 is determined by the fraction of the incoming light that is absorbed by the Er, and the conversion efficiency of excited Er to free $e-h$ pairs η_{int} , which in Chapter 5 we determined to be 70% at room temperature. This gives

$$\eta_{ext} = \left(1 - e^{-\alpha_{WG} \times L}\right) \frac{\alpha_{Er}}{\alpha_{WG}} \times \eta_{int} \quad (1)$$

with α_{Er} (cm^{-1}) the absorption coefficient due to optical absorption at $1.54 \mu\text{m}$ by Er, α_{WG} (cm^{-1}) the total waveguide loss including absorption and scattering, and L (cm) the waveguide length. For a sufficiently long detector, η_{ext} is dominated by α_{Er}/α_{WG} , which gives the magnitude of the Er absorption relative to the total waveguide loss.

Apart from the absorption loss, the waveguide loss α_{WG} also contains scattering loss. It has been shown that a scattering loss below 0.5 dB/cm at $1.5 \mu\text{m}$ can be achieved in SOI waveguides.⁸ In the quantum efficiency calculations this loss will be neglected. The remaining loss contributions in the waveguide detector are: optical absorption by the Er ions, absorption by free carriers, and absorption by the metal contacts.

6.3.1 Absorption by the metal contacts

The presence of a contact on top of the ridge waveguide is required for current collection, but introduces a strong absorption. For example, the absorption coefficient of aluminum at $1.54 \mu\text{m}$ is $1.3 \times 10^6 \text{ cm}^{-1}$. It can be calculated that the presence of an aluminum top contact in the structure in Fig. 6.1 would cause the guided $1.54 \mu\text{m}$ light to be absorbed within $100 \mu\text{m}$. In order to reduce the absorption by the top contact to an acceptable level, the light intensity near the top contact should be reduced. This can be achieved by lowering the effective index just below the top contact, e.g. by performing an additional etch to narrow the top region of the waveguide core, or by partial oxidation of the ridge below the metal

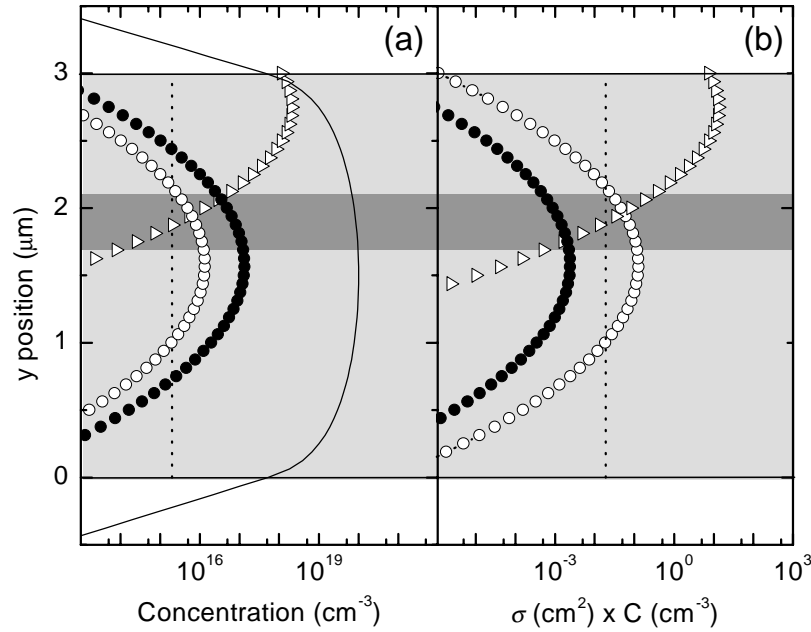


Figure 6.2(a) Concentration depth profiles at $x=0$ for boron (\triangleright), erbium (\bullet), and the Er induced free carrier (electron) concentration (\circ), for the device layout in Fig. 6.1. The Si bulk doping is indicated by the dotted line, and the calculated TE(0,0) mode intensity for $\lambda=1.54 \mu\text{m}$ is indicated by the solid line. The light grey region represents the waveguide core, and the dark grey region represents the depletion region formed at the p - n junction. In this region, free carrier absorption is strongly reduced. (b) Local absorption coefficient for each of the individual curves in Fig. 6.2(a), obtained by multiplying the curves in (a) with the corresponding absorption cross sections, as listed in Table 6.1.

contact. Alternatively, a transparent conductive layer, e.g. indium-tin-oxide optimized for $1.54 \mu\text{m}$ transmission, may be used as a buffer layer between the metal contact and the waveguide core. Since absorption by the top contact is not intrinsic to the detection scheme, it is not included in the following quantum efficiency calculations.

6.3.2 Optical absorption by Er

The magnitude of the Er related optical absorption in the waveguide detector structure is given by $\alpha_{Er} = \sigma_{Er} \times C_{Er,peak} \times \Gamma_{Er}$ with $\sigma_{Er} = 1.8 \times 10^{-20} \text{ cm}^2$ the optical absorption cross section of Er at $1.54 \mu\text{m}$ as determined in Chapter 5, $C_{Er,peak} (\text{cm}^{-3})$ the Er peak concentration, and Γ_{Er} the effective overlap of the Er concentration profile with the intensity distribution in the waveguide core. To optimize the mode overlap, the Er should be located near the center of the waveguide. In the structure

in Fig. 6.1 this can be achieved by means of Er ion implantation at an energy of 5 MeV. The optimum Er concentration will be discussed in section 6.6.

6.3.3 Free carrier absorption

Free electrons and holes in silicon can be excited higher in their respective bands by absorption of sub-bandgap radiation. This free carrier absorption occurs inside the waveguide core due to three sources of electrical carriers: free electrons from the n-type Si waveguide layer (α_n), holes in the p⁺ top contact (α_{p^+}), and Er related free electrons in the center of the waveguide ($\alpha_{Er,e}$) which are present due to the donor character of Er.⁹ The cross sections for optical absorption by free electrons and holes are $9.5 \times 10^{-18} \text{ cm}^2$ and $6.4 \times 10^{-18} \text{ cm}^2$ respectively.¹⁰ Note that these cross sections are two orders of magnitude larger than the cross section for optical absorption by Er. Consequently, for optimum detector performance the overlap of the intensity profile with the highly doped p⁺ contact should be as small as possible.

6.4 Numerical calculations

Calculations of the detector performance were made for the detector layout shown in Fig. 6.1. A 70 keV boron implant to a fluence of 10^{14} cm^{-2} was used for the p⁺ top contact formation, and the Si background doping was taken to be $2 \times 10^{15} \text{ cm}^{-3}$ (corresponding to a resistivity of 2 Ωcm). The Er implantation energy was chosen such that the Er was placed in the center of the waveguide core (5 MeV) and the Er fluence was 10^{13} cm^{-2} . This fluence is sufficiently low to prevent amorphization of the Si, avoiding Er segregation during subsequent crystal regrowth.⁷

Figure 6.2(a) shows the resulting free carrier distributions and the Er distribution as a function of y-position in the waveguide core, with $y=0 \text{ }\mu\text{m}$ corresponding to the Si/SiO₂ interface and $y=3 \text{ }\mu\text{m}$ corresponding to the top of the ridge. Indicated are the hole distribution in the p⁺ contact (\triangleright), the Er concentration profile (\bullet), the Er induced electron concentration (\circ), which is taken to be 10% of the Er concentration assuming 10% electrical activation,⁹ and the Si background doping (dotted line). The depletion region induced by these doping profiles extends from $y=1.7$ to $y=2.1 \text{ }\mu\text{m}$ as indicated by the dark grey area, and contains approximately 30% of the implanted Er.

The requirement of low intensity in the p⁺ region and high intensity at the Er doped center of the waveguide core is optimally fulfilled by 0th-order optical modes. The intensity distributions of the 0th-order transverse electric mode TE(0,0) and the 0th-order transverse magnetic mode TM(0,0) at $1.54 \text{ }\mu\text{m}$ were calculated using a finite difference method. Figure 6.3 shows a graph of the calculated TE(0,0) intensity distribution, with $x=0$ corresponding to the center of the ridge and $y=0$ to the Si/SiO₂ interface. The location of the waveguide core has been indicated. Due to the large core size, almost all power is confined within the Si core. The TM(0,0) mode (not shown) has an almost identical intensity distribution, with a slightly

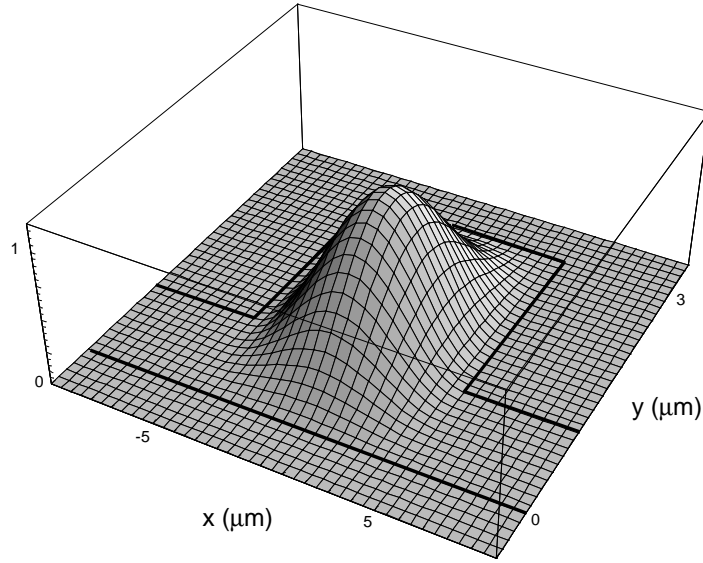


Figure 6.3 Plot of the calculated TE(0,0) mode intensity on a linear scale at $1.54 \mu\text{m}$ in a $3 \mu\text{m} \times 10 \mu\text{m}$ silicon ridge waveguide on SiO_2 . A sketch of the waveguide structure is included.

lower intensity at the top and bottom interfaces. The calculated TE(0,0) intensity distribution at $x=0$ has also been included in Fig. 6.2(a) (solid line).

In order to compare the magnitude of the different contributions to the total absorption, we have multiplied the concentrations in Fig. 6.2(a) by the corresponding absorption cross sections (see Table 6.1). These data are shown in Fig. 6.2(b), using the same symbols as in Fig. 6.2(a). This plot clearly shows that in the present geometry optical absorption by Er is only a small contribution to the total absorption. However, since the interaction between the separate doping profiles generates a depletion region, in part of the waveguide the optical absorption by Er will dominate. The total detector response will thus be determined by absorption in this region, relative to the free carrier absorption losses outside this region.

In order to obtain the absorption of 0th-order modes, we have determined the overlap Γ of the normalized optical modes with the peak-normalized dopant distributions. In the case of free carrier absorption we have taken into account the absence of free carriers in the depletion region of the (unbiased) p - n junction. These data, listed in Table 6.1, together with the known peak concentrations C_{peak} of the distributions and the relevant cross sections σ give the separate contributions to the total absorption according to $\alpha = \sigma \times C_{peak} \times \Gamma$. The results are summarized in Table 6.1. The main contribution to the absorption is found to be free carrier absorption by holes in the top contact ($\alpha_{p+} = 0.65 \text{ cm}^{-1}$ and 0.56 cm^{-1} for the TE(0,0) and

TM(0,0) modes, respectively), even though the mode overlap with these carriers is only $\sim 5\%$.

From the results in Table 6.1 we find that the total waveguide absorption of the detector structure shown in Fig. 6.1 is $\alpha_{WG} = 0.71 \text{ cm}^{-1}$ and $\alpha_{WG} = 0.62 \text{ cm}^{-1}$ for the TE(0,0) and TM(0,0) modes respectively. This means that more than 90% of the guided light is absorbed in a $\sim 4 \text{ cm}$ long waveguide. The fraction of the TE and TM polarized light absorbed by the Er is 1.5×10^{-3} and 1.8×10^{-3} respectively. Together with the known η_{int} of 70%, and assuming an electron-hole collection efficiency of 1, we find an external quantum efficiency of $\sim 10^{-3}$ for a 4 cm long waveguide detector. This is three orders of magnitude higher than measured in Er doped p - n junctions illuminated at normal incidence (see Chapter 5), due to the increased interaction length that can be achieved in a waveguide geometry.

6.5 Preliminary measurements

An Er doped Si p - n junction waveguide detector was fabricated according to the layout in Fig. 6.1, using a 3 MeV Er implant to a fluence of 10^{13} cm^{-2} , a 40 keV B implant to a fluence of 10^{14} cm^{-2} , and a total waveguide length of 5 mm. These conditions, though somewhat different from those used in the simulations, were identical to those used in the experiments described in Chapter 5, in which the concept of the photocurrent generation process was shown. A sketch of the detector structure is shown in Fig. 6.4, showing the Si ridge waveguide with the aluminum top and side contacts. The detector exhibits an open circuit voltage of 0.7 V. Photocurrent measurements were performed by coupling the output of a tunable diode laser ($\lambda_{em} = 1.51\text{-}1.57 \text{ }\mu\text{m}$) into the detector waveguide using a single mode tapered fiber. The laser signal was mechanically chopped at 267 Hz and the photocurrent was measured using lock-in detection. The collected current was converted to external quantum efficiency η_{ext} by dividing the collected photocurrent by the $1.5 \text{ }\mu\text{m}$ photon flux in the input fiber. Hence η_{ext} also includes the fiber-to-waveguide coupling efficiency. Figure 6.4 shows the thus obtained η_{ext} as a function of wavelength, measured at a forward bias of 0.4 V. The spectrum indeed shows an Er related signal at $1.53 \text{ }\mu\text{m}$, on top of a relatively flat background. The background

	$\sigma (\text{cm}^2)$	$C_{peak} (\text{cm}^{-3})$	$\Gamma^{\text{TE}} (\%)$	$\alpha^{\text{TE}} (\text{cm}^{-1})$	$\Gamma^{\text{TM}} (\%)$	$\alpha^{\text{TM}} (\text{cm}^{-1})$
α_{Er}	1.8×10^{-20}	1.4×10^{17}	43	0.0011	44	0.0011
$\alpha_{Er,e}$	9.5×10^{-18}	1.4×10^{16}	29	0.039	31	0.041
α_n	9.5×10^{-18}	2×10^{15}	79	0.015	79	0.015
α_{p+}	6.4×10^{-18}	2×10^{18}	5.2	0.65	4.4	0.56

Table 6.1. Optical absorption cross sections and peak concentrations used in the quantum efficiency calculations, as well as the calculated mode overlap and absorption coefficients.

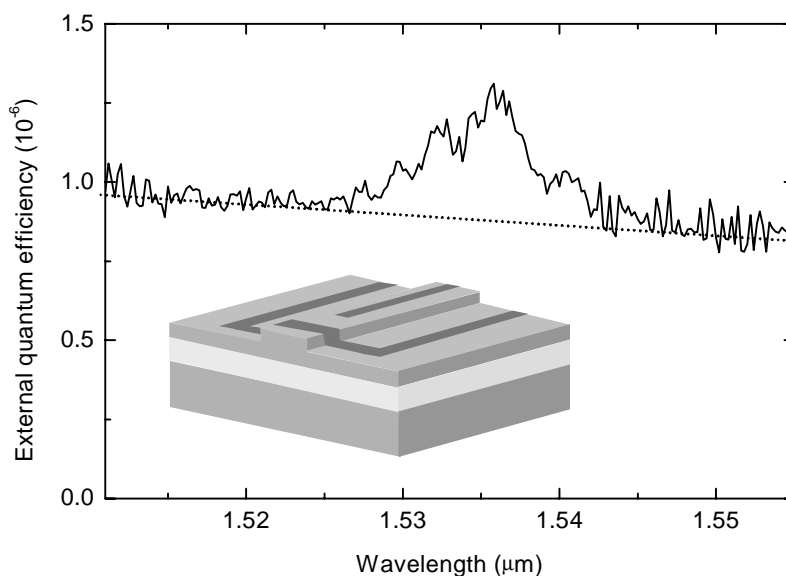


Figure 6.4. Photoresponse of an Er doped waveguide detector fabricated in silicon-on-insulator material using standard silicon processing technology, showing an Er related photocurrent at 1.535 μm . A sketch of the waveguide structure is included. The detector response may be enhanced by three orders of magnitude by lowering the optical mode overlap with the metal contacts (indicated by the dark stripes).

current was also observed for the ion implanted planar p - n junction described in Chapter 5, and is thought to be related to implantation damage in the p - n junction. The Er related photocurrent was found to be roughly independent of the bias conditions, while the background current increased by a factor 14 upon increasing the reverse bias from 0V to 5V. This increase may be related to the spatial distribution of the Er induced implantation damage, which is expected to be mostly located at the end-of-range of the Er implantation profile. As the reverse bias is increased the depletion region reaches the defect rich region, possibly leading to a large defect related current. The defect related current generation mechanism could also be considered as a candidate for a Si based infrared detector.

The observed Er related external quantum efficiency $\eta_{ext}=4\times 10^{-7}$ is much lower than the value calculated in section 6.4, which is due to the strong absorption of the aluminum top contact. The absorption of the TE(0,0) mode by the top contact is estimated to be $\alpha_{TC}\approx 10^2 \text{ cm}^{-1}$ using the calculated mode overlap of 9×10^{-5} and the absorption coefficient of bulk aluminum. Taking this absorption into account, the maximum η_{ext} that can be obtained in the present detector design is 7×10^{-6} , which is about a factor 20 higher than observed. This difference may be related to coupling losses, a low current collection efficiency, or the excitation of higher order modes which are more strongly absorbed by the p^+ doping and the metal contact than low order modes.

6.6 Device optimization

As was already shown in the preceding sections, the presence of free carriers in the waveguide core strongly influences the detector efficiency. The efficiency can be increased by reducing the electrical doping levels. The minimum carrier concentration that can be used is determined by the field required for efficient charge separation. This sets a limit to the doping levels on either side of the Er doped core region.

Another way of increasing the detector efficiency is by increasing the amount of Er in the waveguide core. This however also has a number of undesired consequences. Firstly, because of the donor character of Er, the absorption by Er induced electrons increases. As can be seen from Table 6.1, increasing the Er concentration by a factor 10 already generates an Er related free carrier absorption with a magnitude similar to α_{p+} , which significantly influences the quantum efficiency. Incorporation of large concentrations of erbium may also introduce undesired crystal damage,⁶ which increases the carrier recombination rate and reduces the collection efficiency.

The combination of a good crystal quality and a high Er concentration has only been achieved by the use of oxygen co-doping and high temperature anneals.⁶ Unfortunately these are also the conditions that lead to a high Er donor activity (up to 80%).⁶ Consequently, further experiments are required to find the appropriate impurity co-doping and annealing conditions for optimum detector performance. Note that most studies of the incorporation of Er in Si have focused on optimizing the Er luminescence intensity and reducing the thermal quenching of the intensity. The thus obtained 'optimized' processing conditions may in fact be non-ideal for the desired current generation process.

The proposed detector length of 4 cm is impractical for integration with electrical integrated circuits. However, due to the high refractive index of silicon it is possible to create low loss waveguide bends with a bending radius on the order of 1 μm .¹¹ This makes it possible to design a 4 cm long waveguide spiral confined on an area $< 2 \text{ mm}^2$ with a 40 μm waveguide spacing. Another issue related to the device dimensions is the junction capacitance. The junction area of the 4 cm long waveguide, given by the product of the ridge width and the waveguide length, is 0.4 mm^2 . The capacitance associated with such a large p - n junction limits the detector response time. This problem may be solved by 'photon recycling', *i.e.* by designing a waveguide structure in which light makes multiple passes through a smaller p - n junction. A simple design could involve a Bragg reflector at the waveguide end which reflects the remaining 1.54 μm light back into the detector, reducing the required waveguide length by a factor 2. More sophisticated designs may include micro-ring resonators and waveguide microcavities.¹² Eventually the optimum detector response time will be determined by the rate limiting step in the energy transfer process from Er to the Si electronic system, which in Chapter 5 was determined to be $2 \times 10^6 \text{ s}^{-1}$. Detectors with such a response time could e.g. find

applications in all-optical interconnects used to electrically isolate the driver circuits from Si based high power diodes and transistors, which typically operate at frequencies of 10 kHz.

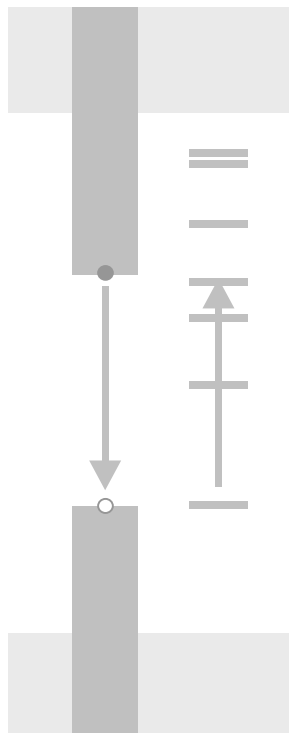
6.7 Conclusions

We have shown that an Er doped waveguide detector in silicon can be fabricated. The proposed structure consists of a silicon waveguide containing an Er doped p - n junction along the waveguide. The detection scheme is based on an energy conversion scheme in which the excitation energy of optically excited Er is transferred to the Si electronic system, causing a photocurrent under 1.54 μm illumination. From optical mode calculations it is concluded that an external quantum efficiency of 10^{-3} can be achieved in a 4 cm long waveguide structure. It is shown that free carrier absorption is an intrinsic limiting factor for the external quantum efficiency. Optimization of the detector design should therefore focus on obtaining optimum overlap of the Er doping profile with the depletion region and minimum overlap of the optical modes with free carriers in the waveguide. Preliminary measurements on an Er doped waveguide detector in silicon indeed show an Er related photocurrent at 1.54 μm . The measured low quantum efficiency is quite low (4×10^{-7}) due to the presence of a strongly absorbing metal top contact.

References

- ¹ G. Franzò, F. Priolo, S. Coffa, A. Polman, and A. Carnera, *Appl. Phys. Lett.* **64**, 2235 (1994)
- ² B. Zheng, J. Michel, F. Y. G. Ren, L. C. Kimerling, D. C. Jacobson, and J. M. Poate, *Appl. Phys. Lett.* **64**, 2842 (1994)
- ³ S. Coffa, G. Franzò, and F. Priolo, *Appl. Phys. Lett.* **69**, 2077 (1996)
- ⁴ A. Polman, N. Hamelin, P. G. Kik, S. Coffa, M. Saggio, and F. Frisina, European Patent 98830592.6, US Patent 09/415,022
- ⁵ D. J. Eaglesham, J. Michel, E.A. Fitzgerald, D. C. Jacobson, J. M. Poate, J. L. Benton, A. Polman, Y.-H. Xie, and L.C. Kimerling, *Appl. Phys. Lett.* **58**, 2797 (1991)
- ⁶ S. Coffa, F. Priolo, G. Franzò, V. Bellani, A. Carnera, and C. Spinella, *Phys. Rev. B* **48**, 11782 (1993)
- ⁷ J. S. Custer, A. Polman, and H. M. van Pinxteren, *J. Appl. Phys.* **75**, 2809 (1994)
- ⁸ J. Schmidtchen, A. Splett, B. Schuppert, K. Petermann, and G. Burbach, *El. Lett.* **27**, 1486 (1991)
- ⁹ J. L. Benton, J. Michel, L. C. Kimerling, D. C. Jacobson, Y. H. Xie, D. C. Eaglesham, E. A. Fitzgerald, and J. M. Poate, *J. Appl. Phys.* **70**, 2667 (1991)
- ¹⁰ M. A. Green, *Silicon solar cells* (University of New South Wales, Sydney, 1995), p. 48
- ¹¹ A. M. Agarwal, L. Liao, J. S. Foresi, M. R. Black, X. Duan, and L. C. Kimerling, *J. Appl. Phys.* **80**, 6120 (1996)
- ¹² J. S. Foresi, P. R. Villeneuve, J. Ferrera, E. R. Thoen, G. Steinmeyer, S. Fan, J. D. Joannopoulos, L. C. Kimerling, H. I. Smith, and E. P. Ippen, *Nature* **390**, 143 (1997)

Part III



Chapter 7

Strong exciton-erbium coupling in Si nanocrystal doped SiO₂

Silicon nanocrystals were formed in SiO₂ using Si ion implantation followed by thermal annealing. The nanocrystal doped SiO₂ layer was implanted with Er to a peak concentration of 1.8 at.%. Upon 458 nm excitation the sample shows a broad nanocrystal related luminescence spectrum centered around 750 nm and two sharp Er luminescence lines at 982 nm and 1536 nm. By measuring the excitation spectra of these features as well as the temperature dependent intensities and luminescence dynamics we conclude that (a) the Er is excited by excitons recombining within Si nanocrystals through a strong coupling mechanism, (b) the Er excitation process at room temperature occurs at a sub-microsecond time scale, (c) excitons excite Er with an efficiency >55%, (d) each nanocrystal can have at most ~1 excited Er ion in its vicinity.

7.1 Introduction

Erbium doped silica glass is used in optical telecommunication technology as an amplification medium. The Er³⁺ ions in the glass matrix exhibit a number of sharp emission lines due to electronic transitions within the 4f shell. The transition from the first excited state to the ground state occurs at 1.53 μm, a standard wavelength in optical telecommunication. Optical amplification at this wavelength can be achieved if sufficient Er can be brought into the first excited state. Unfortunately, the optical cross sections for the intra-4f transitions are rather small, typically on the order of 10⁻²¹ cm². For this reason there is considerable interest in sensitizing the Er³⁺ ions by adding a strongly absorbing species that can transfer energy efficiently to Er. Examples of such sensitizers are the rare earth ion ytterbium¹ and various organic dyes.²

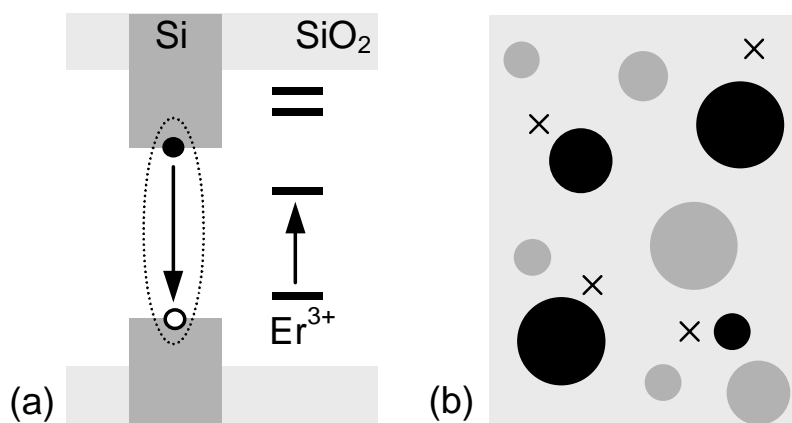


Figure 7.1. (a) Schematic Er excitation model, showing the electronic band structure of Si nanocrystal-doped SiO₂ and the Er 4f energy levels. An optically generated exciton (dotted line) confined in the nanocrystal can recombine and excite Er³⁺. (b) Schematic representation of SiO₂ containing Er (crosses) and nanocrystals (circles). The nanocrystals that couple to Er (black circles) show no exciton luminescence.

Several years ago, it was shown that Er incorporated in silicon rich SiO₂ could be excited outside of the Er³⁺ optical absorption lines.^{3,4} The same effect was observed in Er doped porous silicon,^{5,6} which consists of silicon nanoclusters surrounded by a thin layer of SiO₂. More recently, Fujii *et al.* reported that the presence of Si nanocrystals in Er doped SiO₂ considerably enhances the effective Er absorption cross section.⁷ Following the latter observation, a number of articles appeared that showed similar results for samples prepared by means of cosputtering,⁸ pyrolysis,⁹ and ion implantation.^{10,11} Although the exact structural properties of the nanocrystals depend on the fabrication method employed, all observations strongly suggest that energy is transferred from Si nanocrystals to the Er. A possible excitation model is shown in Fig. 7.1(a), which shows a schematic band diagram of SiO₂ containing a Si nanocrystal and Er³⁺. First a photon is absorbed by the nanocrystal, which causes generation of an exciton inside the nanocrystal. This exciton can recombine radiatively, emitting a photon with an energy that depends on the nanocrystal size. If an Er ion is present close to the nanocrystal, the exciton can recombine non-radiatively by bringing Er into one of its excited states.

Although the excitation model sketched in Fig. 7.1(a) is often referred to, the following issues have not been solved: (1) the *lifetime paradox*: recently Franzò *et al.*¹¹ found that the nanocrystal luminescence decay time is not affected by the presence of Er. They argued that this would be inconsistent with the model in Fig. 7.1(a), since in this model erbium adds a non-radiative decay path for exciton recombination, which should lower the nanocrystal lifetime. (2) The *temperature dependence*: the nanocrystal luminescence intensity and the Er luminescence

intensity are thought to be proportional to the excited concentration of excitons. Nevertheless, in temperature dependent measurements^{8,11} the Er luminescence intensity has repeatedly been observed to behave independently of the nanocrystal luminescence intensity. (3) The *excitation efficiency*: it is not known how efficiently the exciton energy can be transferred to Er. (4) The *excitable Er fraction*: excitation via Si nanocrystals enhances the Er luminescence intensity, but it is not known which fraction of the Er is actually excitable. This knowledge is essential for the design of optical amplifiers and lasers based on Er and nanocrystal doped SiO₂. In this chapter these four points will be addressed and resolved.

7.2 Experiment

Silicon ions were implanted at 35 keV to a fluence of 6×10^{16} cm⁻² into a 100 nm thick SiO₂ layer that was formed by wet thermal oxidation of a lightly B-doped Si(100) substrate. The material was subsequently annealed at 1100 °C for 10 min. in vacuum at a base pressure below 3×10^{-7} mbar. This procedure is known to produce well passivated Si nanocrystals in the size range 2-5 nm.¹² The corresponding nanocrystal concentration is approximately 10^{19} nanocrystals/cm³. The nanocrystal doped region was then implanted with 5.1×10^{15} Er/cm² at 125 keV resulting in an Er peak concentration of 1.8 at.% at a depth of 50 nm. This material was annealed at 1000 °C in vacuum in order to remove implantation induced damage. To further reduce defect related luminescence, the material was passivated by performing an anneal at 800 °C for 30 min. in forming gas (H₂:N₂ at 1:9) at atmospheric pressure.

Photoluminescence (PL) spectra were measured using an Ar laser at 457.9 nm as excitation source. The excitation power was 1-10 mW in a ~1 mm diameter laser spot. The laser beam was modulated at 11 Hz using an acousto-optical modulator. The photoluminescence was focused onto the entrance slit of a grating monochromator and detected using standard lock-in techniques. Luminescence spectra were measured in the 600-1150 nm range using a AgOCs photomultiplier tube, and in the range 1100-1700 nm using a liquid nitrogen cooled Ge detector. All spectra were corrected for the system response. Photoluminescence decay traces were recorded using either a photomultiplier in combination with a photon counting system, or a Ge detector in combination with a digitizing oscilloscope. The system response time in the two cases was 150 ns and 160 μs, respectively. The sample temperature was controlled between 20 K and 300 K using a closed cycle He cryostat.

7.3 Results and discussion

Figure 7.2 shows PL spectra taken at 20, 60, 180, and 300 K at a pump power of 10 mW. At all temperatures a broad luminescence band is observed, extending from 0.6 μm to 1.1 μm, which is attributed to radiative recombination of excitons inside

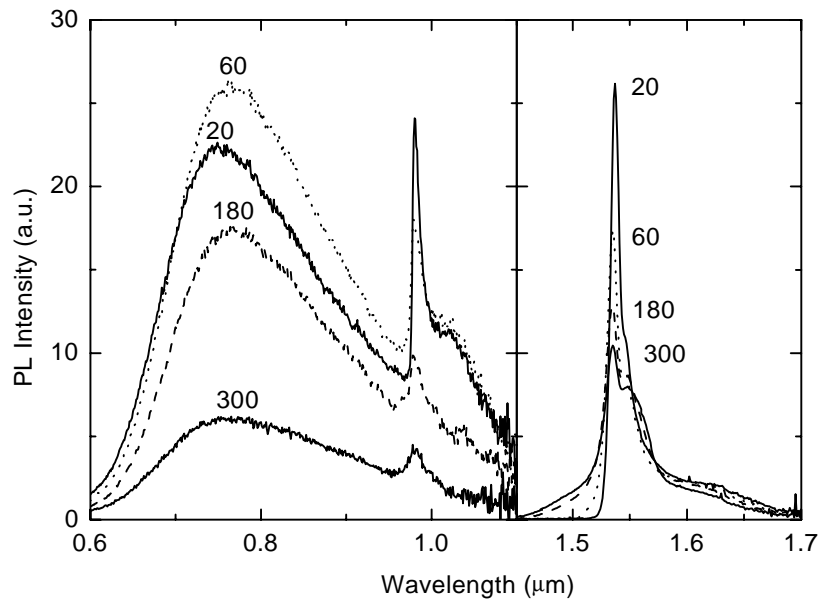


Figure 7.2. Photoluminescence spectra at 20 K, 60 K, 180 K and 300 K showing a broad nanocrystal spectrum in the range 0.6-1.1 μm , and two clear Er luminescence lines at 982 nm and 1536 nm.

Si nanocrystals.¹² The exciton luminescence appears at energies above the bandgap energy of bulk Si due to quantum confinement.¹³ The large spectral width of the nanocrystal luminescence is the result of the rather broad nanocrystal size distribution (2-5 nm diameter). Superimposed on the nanocrystal luminescence spectrum a relatively sharp peak is observed at 982 nm, corresponding to the $^4I_{11/2} \rightarrow ^4I_{15/2}$ transition of Er^{3+} . Another clear emission line is observed at a wavelength of 1536 nm, corresponding to the $^4I_{13/2} \rightarrow ^4I_{15/2}$ transition of Er^{3+} .

Figure 7.3 shows photoluminescence excitation spectra of the nanocrystal luminescence at 750 nm and the Er luminescence at 1536 nm. At a fixed pump power, both the nanocrystal luminescence intensity and the Er luminescence intensity are seen to increase by a factor two when the excitation wavelength is decreased from 514 nm to 458 nm. The absence of absorption resonances in the Er excitation spectrum indicates that the Er is not excited directly by absorption of pump photons, but indirectly via an energy transfer process from Si nanocrystals, as was shown before.^{7,8,11} We attribute the observed wavelength dependence of the luminescence intensity to the increasing nanocrystal optical absorption cross section for increasing photon energy, leading to a higher exciton generation rate. It is tempting to conclude that the luminescent nanocrystals are the nanocrystals that are responsible for the Er excitation. This turns out not to be true, as will be shown below.

In Fig. 7.2 it can be seen that increasing the temperature from 20 K to 300 K first causes the nanocrystal luminescence to increase by 16% and then to decrease

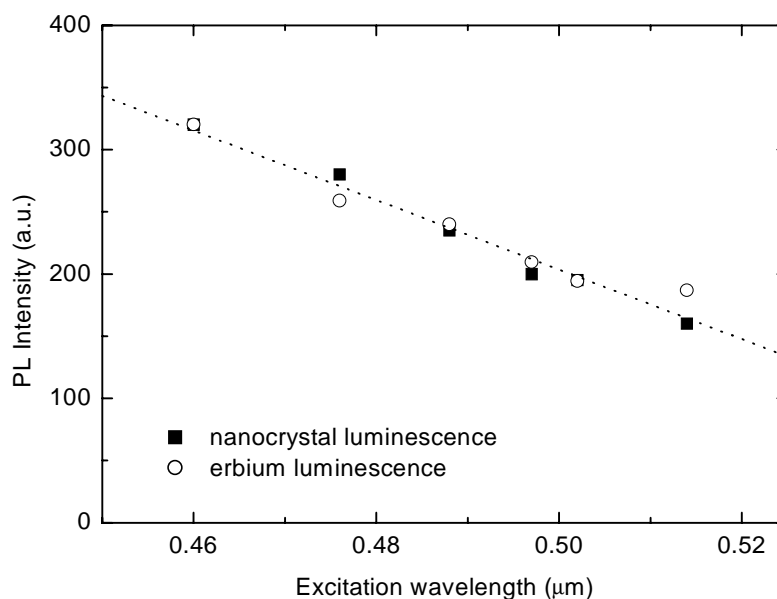


Figure 7.3. Excitation spectrum of the nanocrystal luminescence at 750 nm and the Er luminescence at 1536 nm. The dotted line is a guide to the eye.

by 75% upon going from 60 K to 300 K. This kind of temperature dependence is commonly observed for Si nanocrystals, and can be fully described¹⁴ by a model that takes into account the temperature dependent population of the exciton singlet and triplet states (with low and high radiative decay rate, respectively) in competition with non-radiative processes. The Er luminescence peak at 1.536 μm exhibits an entirely different temperature dependence. The temperature increase only induces spectral broadening due to the thermal redistribution over the Stark levels, while the integrated intensity remains constant within 10%. These observations contradict any model that directly links the observed nanocrystal and Er luminescence intensities.

Figure 7.4 shows luminescence decay curves of the nanocrystal luminescence at 750 nm and the Er luminescence at 1536 nm, measured at 15 K and 300 K at a pump power of 1 mW. It is found that the nanocrystal decay rate (Fig. 7.4(a)) increases from $1.5 \times 10^3 \text{ s}^{-1}$ to $4.8 \times 10^4 \text{ s}^{-1}$ upon going from 15 K to 300 K, which is consistent with the exciton singlet-triplet decay model.¹² The Er decay rate at 1.536 μm (Fig. 7.4(b)) is found to be 500 s^{-1} at all temperatures between 20 K and 300 K, which implies that the Er luminescence efficiency is temperature independent.

A consistent description of the observed temperature dependencies can be obtained if we assume *strong coupling* between a Si nanocrystal and Er. If the energy transfer from a nanocrystal to Er is fast, we expect to see no luminescence from a nanocrystal that is coupled to Er, since any generated exciton will immediately recombine non-radiatively by exciting Er. Such fast transfer might occur because at the high nanocrystal density ($\sim 10^{19} / \text{cm}^3$) the maximum distance

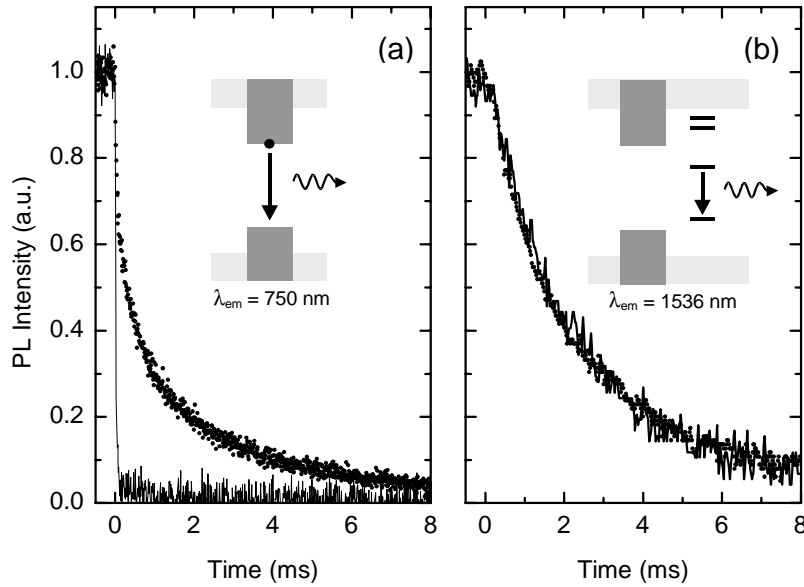


Figure 7.4. Luminescence decay measurements taken at 15 K (dots) and at 300 K (drawn lines) of (a) nanocrystal luminescence at 750 nm, and (b) Er^{3+} luminescence at 1536 nm.

between an Er ion and the nearest nanocrystal is ~ 1 nm. The Er luminescence intensity will then be determined by the product of the nanocrystal absorption cross section, which is approximately temperature independent and the Er luminescence efficiency, which is also temperature independent (Fig. 7.4(b)).

The fact that the Er luminescence is constant up to room temperature, implies that the energy transfer to Er must occur well within the nanocrystal decay time at 300 K, which is 21 μs . Consequently the transfer rate constant must be larger than $\sim 10^6 \text{ s}^{-1}$ at room temperature. This fast transfer explains the paradox encountered by Franzò *et al.*, who found that while the incorporation of Er does reduce the nanocrystal luminescence, it does not affect the nanocrystal decay time. This behavior is now expected, since in the strong coupling case all observed nanocrystal luminescence originates from nanocrystals that do not couple to Er, while nanocrystals that do couple to Er show no luminescence. This model is shown schematically in Fig. 7.1(b).

In order to determine the Er excitation efficiency, we measured both the nanocrystal and the Er luminescence $1/e$ rise time (τ_r) and decay time (τ) at 5 mW pump power (see time dependent data in Fig. 7.5(a)). From these two time constants we can deduce the excitation rate $R = (1/\tau_r - 1/\tau)$, assuming that both the Er and the nanocrystals effectively behave as two-level systems. At a pump intensity of 5 mW/mm^2 we find for the nanocrystal excitation rate $R_{nc} = 940 \text{ s}^{-1}$ and for the excitation rate of the Er $^4\text{I}_{13/2}$ level $R_{Er} = 570 \text{ s}^{-1}$. Note that this Er excitation rate may contain a contribution of excitation into the higher lying Er energy levels,

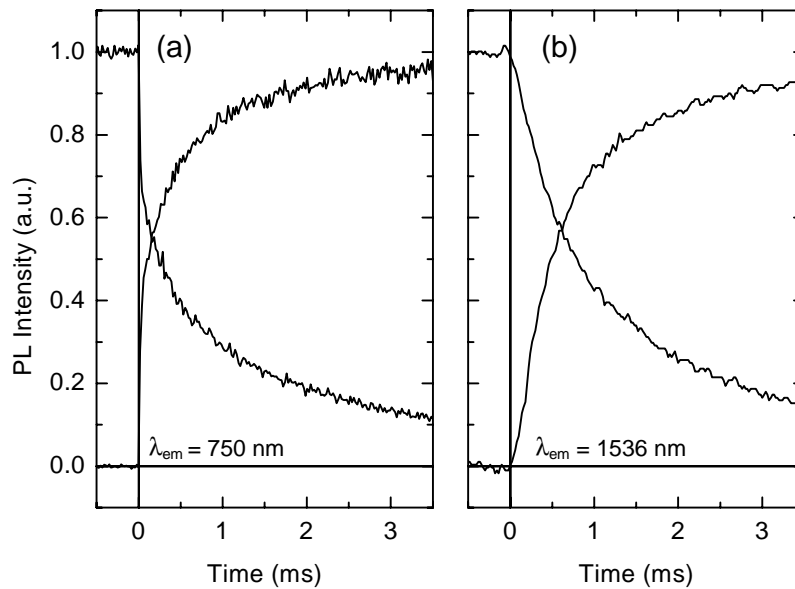


Fig. 7.5. Luminescence rise time and decay measurements at 5 mW pump power at 15 K for (a) nanocrystal luminescence at 750 nm, and (b) Er luminescence at 1536 nm.

followed by non-radiative relaxation to the first excited state. Comparing the nanocrystal and Er excitation rates, we conclude that at least 55% of the generated excitons recombine by transferring energy to Er.¹⁵ This high conversion efficiency is in agreement with the strong coupling picture.

The high excitation efficiency also raises a new question. At the peak concentration of 1.8 at.% Er, the Er-to-nanocrystal ratio is approximately 100:1, which implies that in principle many Er ions compete for the same exciton. Nevertheless the observed Er excitation rate is close to that of a single nanocrystal. This leads to the conclusion that a single nanocrystal can effectively excite only ~1 Er ion. This has important implications for the design of nanocrystal sensitized Er doped lasers or optical amplifiers operating at 1.54 μm , as will be further discussed in Chapters 8 and 9.

7.4 Conclusions

We have shown evidence for strong coupling between excitons and Er in Si nanocrystal doped SiO₂. The energy transfer takes place at a sub-microsecond time scale. The exciton-to-Er energy transfer efficiency is larger than 55%, and the maximum number of excitable Er ions around a single nanocrystal is near unity.

References

- ¹ M. P. Hehlen, N. J. Cockroft, T. R. Gosnell, and A. J. Bruce, *Phys. Rev. B* **56**, 9302 (1997)
- ² S. I. Klink, G. A. Hebbink, L. Grave, F. C. J. M. Van Veggel, D. N. Reinhoudt, L. H. Slooff, A. Polman, and J. W. Hofstraat, *J. Appl. Phys.* **86**, 1181 (1999)
- ³ S. Lombardo, S. U. Campisano, G. N. van den Hoven, A. Cacciato, and A. Polman, *Appl. Phys. Lett.* **63**, 1942 (1993)
- ⁴ G. N. van den Hoven, J. H. Shin, A. Polman, S. Lombardo, and S. U. Campisano, *J. Appl. Phys.* **78**, 2642 (1995)
- ⁵ T. Kimura, A. Yokoi, H. Horiguchi, R. Saito, T. Ikoma, and A. Sato, *Appl. Phys. Lett.* **65**, 983 (1994)
- ⁶ J. H. Shin, G. N. van den Hoven, and A. Polman, *Appl. Phys. Lett.* **66**, 2379 (1995)
- ⁷ M. Fujii, M. Yoshida, Y. Kanzawa, S. Hayashi, and K. Yamamoto, *Appl. Phys. Lett.* **71**, 1198 (1997)
- ⁸ M. Fujii, M. Yoshida, S. Hayashi, and K. Yamamoto, *J. Appl. Phys.* **84**, 4525 (1998)
- ⁹ J. St. John, J.L. Coffey, Y. Chen, and R.F. Pinizzotto, *J. Am. Chem. Soc.* **121**, 1888 (1998)
- ¹⁰ C. E. Chryssou, A. J. Kenyon, T. S. Iwayama, C. W. Pitt, and D. E. Hole, *Appl. Phys. Lett.* **75**, 2011 (1999)
- ¹¹ G. Franzò, V. Vinciguerra, and F. Priolo, *Appl. Phys. A* **69**, 3 (1999)
- ¹² M. L. Brongersma, A. Polman, K. S. Min, E. Boer, T. Tambo, and H. A. Atwater, *Appl. Phys. Lett.* **72**, 2577 (1998)
- ¹³ C. Delerue, G. Allan, and M. Lannoo, *Phys. Rev. B* **48**, 11024 (1993)
- ¹⁴ M. L. Brongersma, P. G. Kik, and A. Polman, *Appl. Phys. Lett.* **76**, 351 (2000)
- ¹⁵ We assume that the nanocrystal absorption cross section and radiative decay rate are not affected by the presence of Er

Chapter 8

Exciton-erbium interactions in Si nanocrystal doped SiO₂

The presence of silicon nanocrystals in Er doped SiO₂ can enhance the effective Er optical absorption cross section by several orders of magnitude due to a strong coupling between quantum confined excitons and Er. This chapter discusses the fundamental processes that determine the potential of Si nanocrystals as sensitizers for use in Er doped waveguide amplifiers or lasers. Silicon nanocrystals were formed in SiO₂ using Si ion implantation and thermal annealing. The nanocrystal doped SiO₂ layer was implanted with different doses of Er, resulting in Er peak concentrations in the range 0.015 at.% - 1.8 at.%. All samples show a broad nanocrystal related luminescence spectrum centered around 800 nm and a sharp Er luminescence line at 1536 nm. By varying the Er concentration and measuring the nanocrystal and Er photoluminescence intensity, the nanocrystal excitation rate, the Er excitation and decay rate, and the Er saturation with pump power, we conclude that: *a)* the maximum amount of Er that can be excited via exciton recombination in Si nanocrystals is ~1 Er ion per nanocrystal, *b)* the Er concentration limit can be explained by two different mechanisms occurring at high pump power, namely Auger de-excitation and pair induced quenching, *c)* the excitable Er ions are most likely located in an SiO₂-like environment and have a luminescence efficiency < 18%, and *d)* at a typical nanocrystal concentration of 10¹⁹ cm⁻³, the maximum optical gain at 1.54 μm of an Er doped waveguide amplifier based on Si nanocrystal doped SiO₂ is ~0.6 dB/cm.

8.1 Introduction

Erbium doped optical amplifiers are an important component in optical telecommunication networks. The operation of these amplifiers relies on an optical transition of Er³⁺ at 1.54 μm, which is in the region of optimum transmission of silica based glass fiber. The transition responsible for the 1.54 μm luminescence

occurs within the partially filled 4f shell of Er^{3+} , which is electrically shielded from its surroundings by filled 5s and 5p shells. As a result of spin-spin and spin-orbit interactions, the 4f shell can be optically excited into several discrete energy levels, for example at 0.81 μm , 0.98 μm , and 1.54 μm . The optical cross sections for these transitions are small, typically on the order of 10^{-21} cm^2 , because optical transitions between the 4f levels are parity forbidden. Consequently, rather high pump intensities are needed to reach population inversion, typically on the order of 1 kW/cm^2 .

Several years ago, it was shown that Er incorporated in silicon rich SiO_2 could also be excited outside of the Er^{3+} optical absorption lines.^{1,2} The same effect was observed in Er doped porous silicon,^{3,4} which consists of silicon nanoclusters surrounded by a thin layer of SiO_2 , and more recently in Si nanocrystal doped SiO_2 containing Er.⁵⁻⁹ It was shown that the addition of Si nanocrystals to Er doped SiO_2 strongly enhances the effective Er absorption cross section. In Chapter 7 it was demonstrated that exciton recombination inside Si nanocrystals causes the excitation of Er through a strong coupling mechanism.

This energy transfer process could enable the fabrication of an optical amplifier operating at 1.54 μm that is optically excited at pump intensities as low as a few mW/mm^2 . Additionally, it may be possible to excite Er electrically by supplying electrical carriers to an Er and Si nanocrystal doped SiO_2 layer. However, little is known about a number of crucial parameters that determine the performance of such devices, such as the Er excitation efficiency, the Er luminescence efficiency, and the maximum Er concentration.

In Chapter 7 we have shown that at high Er concentration (1.8 at.%) the Er excitation process is efficient (quantum efficiency > 55%), while the excitable fraction of the Er is low. In the present chapter we report the Er concentration dependence of the optical properties of Si nanocrystal doped SiO_2 . We show that the maximum concentration of excitable Er in this material is ~0.02 at.%, and propose mechanisms that could give rise to this concentration maximum. Furthermore, we show that the Er luminescence efficiency is less than 18%. Finally, we show that the maximum gain that can be obtained in this material is ~0.6 dB/cm at 1.54 μm .

8.2 Experiment

A 100 nm thick layer of SiO_2 was grown on a lightly B-doped Si(100) substrate by means of wet thermal oxidation. This layer was implanted with 35 keV Si to a fluence of $6 \times 10^{16} \text{ cm}^{-2}$. The implantation yields an approximately Gaussian depth distribution of excess Si in the SiO_2 film, with a peak concentration of 19 at.% at a depth of 45 nm. The samples were subsequently annealed at 1100 $^\circ\text{C}$ for 10 min. in vacuum at a base pressure below 3×10^{-7} mbar, in order to induce nucleation and growth of Si nanocrystals. This treatment has been shown to produce Si nanocrystals with a diameter in the range 2-5 nm.¹⁰ Assuming a typical nanocrystal diameter of 3 nm ($\sim 10^3$ Si atoms), the nanocrystal peak concentration is estimated

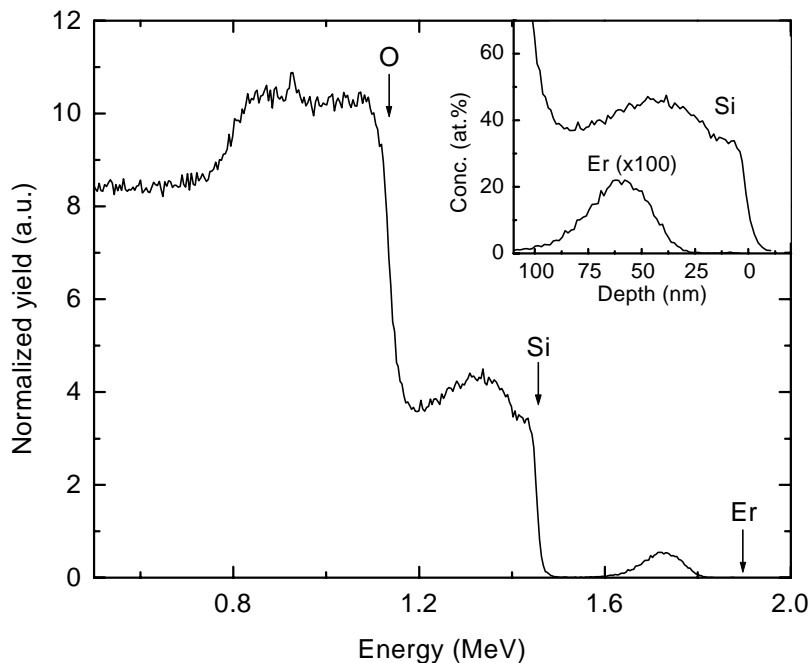


Figure 8.1. RBS measurement of Si nanocrystal doped SiO₂ implanted with 4.5×10^{14} Er/cm², taken at a scattering angle of 96.2° using a 2 MeV He⁺ beam. The surface energies of Er, Si, and O are indicated by the arrows. The inset shows the corresponding Er and Si concentration profiles.

to be $\sim 10^{19}$ cm⁻³ at the center of the SiO₂ layer. The samples were then implanted with different Er fluences in the range 3.6×10^{13} cm⁻² – 5.1×10^{15} cm⁻² at a fixed energy of 125 keV. These implants result in an approximately Gaussian Er depth distribution, with Er peak concentrations ranging from 0.015 at.% to 1.8 at.% at a depth of 61 nm. A non Er implanted sample was kept as a reference. Figure 8.1 shows a Rutherford Backscattering Spectrometry (RBS) measurement of a sample containing 4.5×10^{14} Er/cm² taken at a scattering angle of 96.2° using a 2.0 MeV He⁺ beam. The energies corresponding to erbium, silicon, and oxygen located at the sample surface are indicated. Note that the rise of the RBS signal around 1.13 MeV is the combined effect of signal from oxygen at the sample surface and signal from silicon in the substrate. The inset shows the Si and Er concentration profile in the SiO₂ layer as obtained from the RBS data. Note that the Er ions were implanted slightly deeper than the Si ions.

All samples were annealed for 10 min. in vacuum at 1000 °C to remove implantation induced damage. In order to further reduce defect related luminescence and to saturate dangling bonds on the Si nanocrystal surface, a passivating anneal was performed at 780 °C for 30 min. in forming gas (H₂:N₂ at 1:9) at atmospheric pressure.

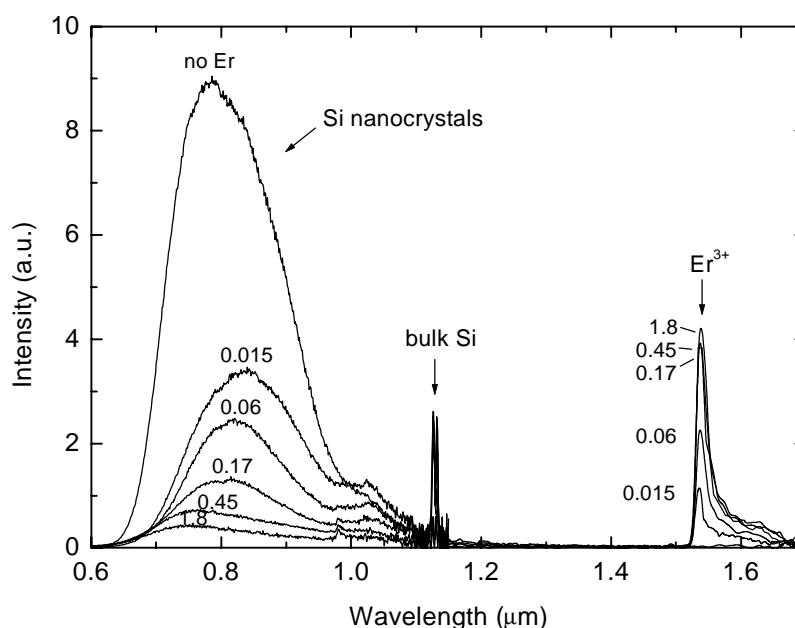


Figure 8.2. Photoluminescence spectra of Si nanocrystal doped SiO₂ containing different Er concentrations in the range 0 - 1.8 at.%, measured at 15 K using a pump power of 1 mW at 458 nm.

Photoluminescence (PL) spectra were measured using the 458 nm line of an Ar laser as excitation source at a peak power of 1 mW in a $\sim 1 \text{ mm}^2$ laser spot. The laser beam was modulated *on-off* at 11 Hz using an acousto-optical modulator. The emitted light was passed through a grating monochromator and detected using standard lock-in techniques. Spectra were measured in the range 600-1150 nm using an AgOCs photomultiplier tube, and in the range 1100-1700 nm using a liquid nitrogen cooled Ge detector. All spectra were corrected for the detector response. Photoluminescence decay traces were recorded using a multichannel photon counting system in combination with the photomultiplier and a digitizing oscilloscope in combination with the Ge detector. The system response for the two cases was 150 ns and 160 μs , respectively. For all luminescence measurements the samples were cooled to 15 K using a closed cycle He cryostat.

8.3 Results and discussion

8.3.1 Photoluminescence vs. Er concentration

Figure 8.2 shows a PL spectrum of a SiO₂ film doped with Si nanocrystals (marked "no Er"). The sample shows a broad luminescence band peaking at 790 nm. We have previously shown that this luminescence is caused by the radiative recombination of electron-hole pairs (excitons) confined within the Si nanocrystals.¹⁰ Due to quantum confinement¹¹ the exciton luminescence appears at energies

above the bandgap energy of bulk Si (1.17 eV at 15 K). The large spectral width of the nanocrystal luminescence is the result of the broad nanocrystal size distribution (2-5 nm diameter). The luminescence peak at 1.13 μm is caused by phonon-assisted electron-hole pair recombination in the Si substrate. Figure 8.2 also shows luminescence spectra for samples containing Er at various concentrations. The incorporation of 0.015 at.% Er reduces the nanocrystal luminescence by more than a factor two, and a luminescence peak appears at a wavelength of 1.536 μm . This wavelength corresponds to the radiative transition from the first excited state ($^4\text{I}_{13/2}$) to the ground state ($^4\text{I}_{15/2}$) of Er^{3+} . Increasing the Er concentration leads to a further reduction of the nanocrystal luminescence intensity, accompanied by an increase of the Er luminescence intensity. This behavior is consistent with the strong coupling model presented in Chapter 7, in which a nanocrystal becomes 'dark' once it couples to a nearby Er ion. Increasing the Er concentration therefore increases the fraction of dark nanocrystals.

Upon increasing the Er concentration, the nanocrystal luminescence spectrum is first seen to shift to longer wavelength, and then to shorter wavelength. This effect is related to the slight mismatch in the Er and Si implantation depth (see Fig. 8.1). As was shown previously,¹² the long wavelength emission originates from relatively large nanocrystals located at the center of the Si implanted region, while the emission at short wavelength originates from relatively small nanocrystals located in the tails of the Si concentration profile. Since in the present work the Er is implanted slightly deeper than the silicon, the incorporation of a small amount of Er will first affect the (small) nanocrystals near the SiO₂/Si interface, leading to a reduction in the emission at short wavelength. As the Er concentration is increased, the (large) nanocrystals at the center of the SiO₂ film are also affected, leading to a reduction in the emission at large wavelength, as observed in Fig. 8.2.

8.3.2 Internal quantum efficiency vs. Er concentration

The power conversion efficiency of potential optical amplifiers or lasers making use of Er excitation via Si nanocrystals will depend on the internal quantum efficiency (IQE) of the energy transfer process, *i.e.* the efficiency with which nanocrystals coupled to Er can generate excited Er. To determine the Er concentration dependence of the IQE, the intensities in Fig. 8.2 were converted to photon flux and then integrated over the nanocrystal emission spectrum and the Er emission spectrum respectively. Figure 8.3 shows the thus obtained nanocrystal related emission ϕ_{nc} (●) and Er related emission ϕ_{Er} (○) on the same relative scale. At zero Er concentration $\phi_{Er}=0$ and $\phi_{nc}=100$. At the highest Er concentration $\phi_{Er}=9$ and $\phi_{nc}=7$, which indicates that 9 Er related photons are obtained at the cost of 93 nanocrystal related photons. These values give a *relative* measure of the concentration dependent IQE, since we do not know the Er and nanocrystal luminescence efficiencies. Thus we have:

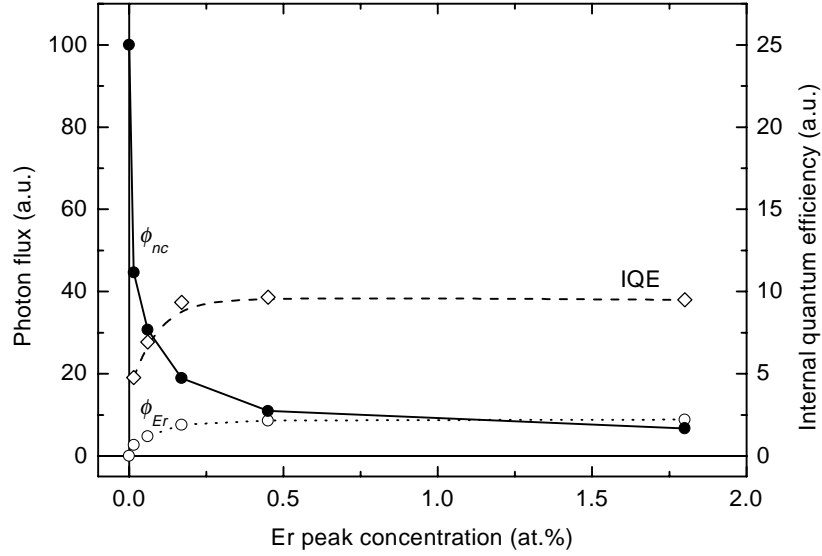


Figure 8.3. Integrated emission of the nanocrystal-related luminescence (●) and the Er related luminescence (○) on the same relative scale, measured at 15 K. The relative internal quantum efficiency of the Er excitation process is plotted on the right hand axis (◇).

$$\text{IQE} \propto \frac{\phi_{Er}}{\phi_{nc}(0) - \phi_{nc}}, \quad (1)$$

with $\phi_{nc}(0)$ the nanocrystal related emission at zero Er concentration. This IQE is depicted in Fig. 8.3 for all Er concentrations (◇). The IQE first increases with Er concentration, and then saturates above 0.2 at.% Er. The fact that the internal quantum efficiency reaches a fixed value at high Er concentration confirms that the observed reduction in nanocrystal luminescence is caused by energy transfer to Er, and not for example by the destruction of nanocrystals during the ion implantation process. We conclude that the IQE of nanocrystals coupled to Er is essentially independent of the Er concentration. The relatively low efficiency at low Er concentration will be discussed further in section 8.3.6.

Using independent measurements of the nanocrystal and Er excitation rates published presented in Chapter 7, we have shown that at an Er concentration of 1.8 at.%, the $\text{IQE} \geq 55\%$. The observation in Fig. 8.3 that only 10% of the nanocrystal photons yield $1.54 \mu\text{m}$ photons then implies that the Er luminescence efficiency from the first excited state $\eta_{1.54} < 18\%$. Implications of this observation will be discussed in section 8.3.7.

8.3.3 Nanocrystal luminescence lifetime vs. Er concentration

Figure 8.4 shows nanocrystal luminescence decay traces taken at 750 nm and $T=15 \text{ K}$ for samples containing different Er concentrations. In a sample containing

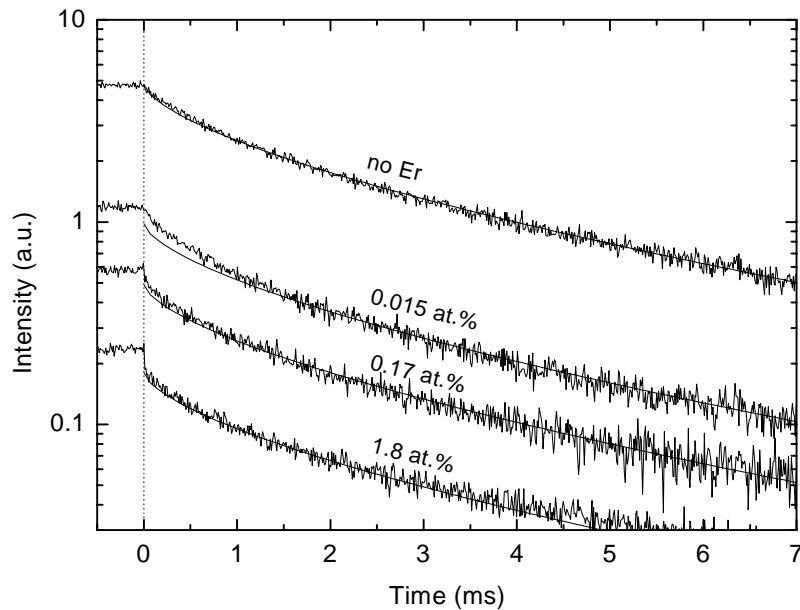


Figure 8.4. Photoluminescence decay traces of the nanocrystal luminescence at 750 nm for different Er concentrations in the range 0-1.8 at.%, measured at 15 K using 1 mW pump power at 458 nm. The pump is switched off at $t=0$. The drawn lines represent stretched exponential decay with $\tau=2.0$ ms and $\beta=0.65$.

no Er, the nanocrystal luminescence shows a $1/e$ lifetime of 2.0 ms. The decay is well described by stretched exponential decay of the form $I(t)=\exp(-(t/\tau)^\beta)$ with $\tau=2.0$ ms and $\beta=0.65$ (solid line). The same curve has been overlaid on all data in order to facilitate comparison between the different traces.

Incorporation of Er leads to a significant reduction of the nanocrystal luminescence intensity at 750 nm, as was already observed in Fig. 8.2. The decay time however varies only slightly from sample to sample, and no trend is observed with increasing Er concentration. The highest Er concentration sample shows a small initial fast decay, which is attributed to luminescence from defects in the SiO₂ matrix.¹²

These lifetime measurements confirm the strong coupling model proposed in Chapter 7, which states that the decrease in nanocrystal intensity for increasing Er concentration in Fig. 8.2 is due to a reduction in the number of luminescent nanocrystals. All remaining nanocrystal luminescence therefore originates from nanocrystals that are not coupled to Er, which show their intrinsic decay characteristics. These nanocrystals are expected to be mostly located near the sample surface, where the Er concentration is relatively low (see RBS data in Fig. 8.1).

The fact that the nanocrystal luminescence decay time does not depend on the Er concentration has been observed previously by Franzò *et al.*⁹ They explained

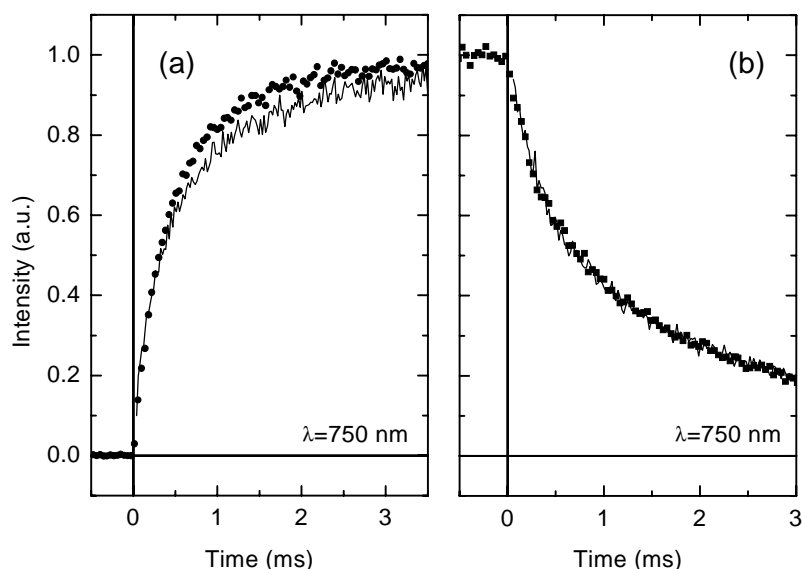


Figure 8.5. Photoluminescence rise (a) and decay traces (b) of the nanocrystal luminescence at 750 nm, measured at 15 K using 5 mW excitation at 458 nm for samples containing no Er (dots) and 1.8 at.% Er (solid line).

their experimental findings by assuming that the nanocrystal related luminescence around 750 nm is not emitted by quantum confined excitons, but rather by a luminescent center at the nc-Si/SiO₂ interface that is excited via optically generated excitons. In this scenario, excitons can transfer their energy either to such a center or to an Er ion, after which the Er ion and the center do not interact. Consequently, varying the Er concentration would only shift the balance between these two processes, and indeed leave the lifetime of the 750 nm luminescence unaffected. However, according to this model, the reduction of the nanocrystal luminescence in Fig. 8.2 should be accompanied by a reduction of the apparent nanocrystal *excitation rate*. Such a reduction is not observed, as will be shown below.

The effect of Er on the nanocrystal excitation rate was measured by monitoring the time dependence of the 750 nm luminescence while modulating the pump beam. Figure 8.5 shows normalized luminescence traces at 750 nm after switching the pump laser on (a) and off (b) for a sample containing no Er (dots) and a sample containing an Er peak concentration of 1.8 at.% (solid line). The applied pump power was 5 mW at 458 nm. The defect related fast component (see Fig. 8.4) has been removed from the data to facilitate comparison. The nanocrystal luminescence decay characteristics (Fig. 8.5(b)) are identical for the two samples, with a 1/e decay time $\tau_{decay}=1.30$ ms. This is somewhat shorter than the 1/e times observed at a pump power of 1 mW, possibly due to exciton-exciton interactions or saturation of nanocrystals with a long lifetime. The 1/e rise times τ_{rise} are 0.47 ms and 0.56 ms for samples containing no Er and 1.8 at.% Er, respectively.

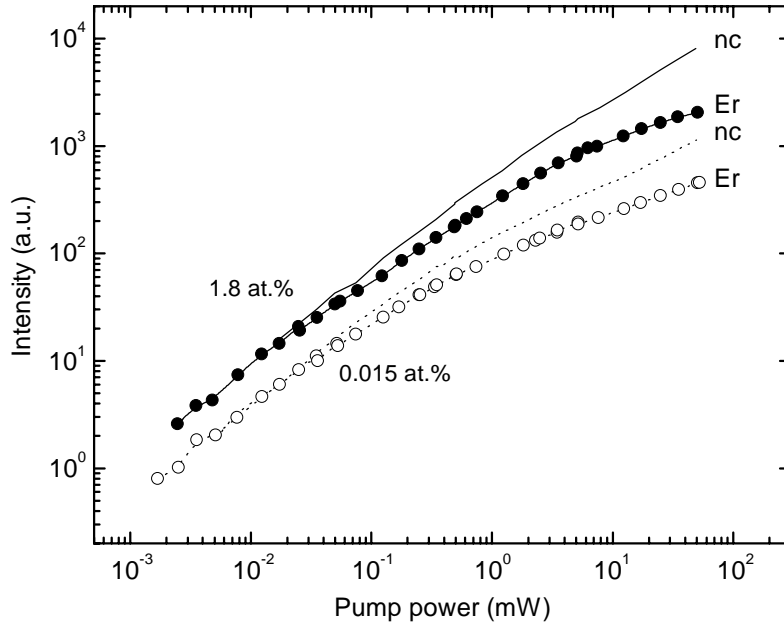


Figure 8.6. Photoluminescence intensity of the nanocrystal peak luminescence and the Er peak luminescence as a function of pump power for samples containing 0.015 at.% and 1.8 at.% Er, measured at 15 K using 458 nm pump light in a $\sim 1 \text{ mm}^2$ spot.

The measured τ_{rise} and τ_{decay} can be used to determine the excitation rate R_{exc} . If we model the luminescence at 750 nm by a two-level system, R_{exc} is given by

$$R_{exc} = \frac{1}{\tau_{rise}} - \frac{1}{\tau_{decay}} . \quad (2)$$

This gives a nanocrystal excitation rate of 1360 s^{-1} at 750 nm in the sample containing no Er. Incorporation of 1.8 at.% Er reduces the nanocrystal excitation rate to 1020 s^{-1} . The 25% reduction in excitation rate is insufficient to explain the observed twenty-fold decrease of the nanocrystal luminescence intensity at 750 nm upon incorporating 1.8 at.% Er (Fig. 8.2). Hence the data can not be described using the model proposed by Franzò *et al.* The data can be described by the strong coupling model, since this mechanism indeed leaves the luminescence characteristics of the luminescent nanocrystals, *i.e.* those which are not coupled to Er, unaffected.

8.3.4 Er luminescence intensity vs. pump power

The data in Fig. 8.2 show a sub-linear increase of the Er luminescence intensity with Er concentration. This can be ascribed to the fact that as the Er concentration is

increased, at a given pump power the exciton concentration available for Er excitation is reduced. At sufficiently high pump power however, the Er luminescence intensity is no longer limited by the exciton concentration but rather by the total amount of excitable Er. Therefore we can compare the total amount of excitable Er in samples with different Er concentrations by comparing Er luminescence intensities at high pump power.

Figure 8.6 shows the effect of pump power on the Er and nanocrystal luminescence intensity for samples containing 0.015 at.% Er and 1.8 at.% Er respectively. For both samples the nanocrystal luminescence intensity was scaled to coincide with the low power Er luminescence intensity. Below 20 μW the Er luminescence and the nanocrystal luminescence depend linearly on pump power. At these low pump powers the Er luminescence intensities from the two samples differ by a factor ~ 2 . Increasing the pump power causes a sublinear increase of the Er luminescence in both samples, suggesting that a significant fraction of the excitable Er is brought into the first excited state. At a pump power of 50 mW the nanocrystal luminescence continues to increase, while the Er luminescence intensity levels off. In this pump power regime the exciton generation rate is no longer the limiting factor for the Er luminescence intensity. Nevertheless, the Er luminescence intensities for the two samples at 50 mW pump power differ by only a factor 5, even though the total amount of Er in the samples differs by more than a factor 100.

The above shows that the concentration of excitable Er in the high concentration (1.8 at.%) sample is at most 5 times higher than in the low concentration (0.015 at.%) sample. This suggests that the concentration of excitable Er is < 0.1 at.%. The existence of such a concentration limit is also observed in the Er excitation rate, as will be shown in the next paragraph.

8.3.5 The Er excitation and decay rate vs. Er concentration

When the amount of Er coupled to a nanocrystal is increased, the Er excitation rate per ion should reduce, since several Er ions then compete for the same exciton. In order to determine the concentration dependent Er excitation rate, we performed rise time and decay time measurements of the Er luminescence at 1.536 μm . At the applied pump power of 1 mW all samples show approximately exponential time dependencies. Figure 8.7 shows the measured rates $W_{\text{rise}}=1/\tau_{\text{rise}}$ (Δ) and $W_{\text{decay}}=1/\tau_{\text{decay}}$ (\blacktriangledown) obtained by exponential fitting of the data.

The Er decay rate increases from 500 s^{-1} to 700 s^{-1} as the Er peak concentration is increased from 0.015 at.% to 1.8 at.%. This increase is attributed to a concentration quenching effect which is known to occur when rare earth ions are spaced closely enough to allow for energy exchange between neighboring ions. As a result, excitation energy can migrate¹³ to neighboring ions, which may in turn be coupled non-radiatively to quenching sites, *e.g.* defects or OH groups present in the matrix. In a simple concentration quenching model, the Er decay rate increases linearly with Er concentration, which is indeed observed in Fig. 8.7. By measuring the slope of the decay rate data in Fig. 8.7, we can estimate¹⁴ that the concentration

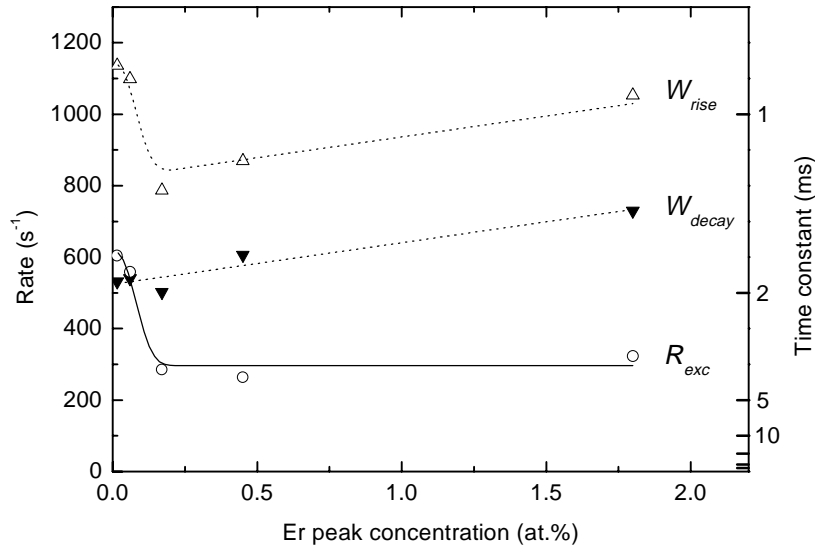


Figure 8.7. Rise (Δ) and decay rates (\blacktriangledown) of the 1.536 μm Er luminescence, measured at 15 K using a pump power of 1 mW at 458 nm, and the Er excitation rate (\circ) derived from these data. The drawn lines serve as a guide to the eye.

of quenching sites in the Er implanted Si nanocrystal doped SiO₂ film is as low as 10^{18} cm^{-3} .

Data for the Er excitation rate R_{exc} calculated from τ_{rise} and τ_{decay} using Eq. 2 are also shown in Fig. 8.7 (\circ). At an Er concentration of 0.015 at.%, the Er excitation rate is 600 s^{-1} . Increasing the Er concentration to 0.17 at.% reduces the excitation rate by a factor 2. A further increase of the Er concentration has no effect on the excitation rate, even though at these concentrations several Er ions might couple to the same nanocrystal, which would reduce the excitation rate per Er ion. The fact that such a reduction is not observed, shows that there is an upper limit to the number of Er ions that can be excited by a single nanocrystal. From the data in Fig. 8.7 it is clear that this limit is reached at an Er concentration < 0.17 at.% Er, which is consistent with the maximum value of 0.1 at.% Er found in the preceding paragraph.

From the measured Er excitation rate of $\sim 300 \text{ s}^{-1}$ at 1 mW we can determine an effective absorption cross section σ_{eff} for the Er excitation process. We find that $\sigma_{eff} \approx 10^{-15} \text{ cm}^2$ at 458 nm, which is a factor $\sim 10^5$ larger than what can be achieved using direct optical pumping of the Er ions. This value is of the same order as a typical Si nanocrystal absorption cross section at this wavelength,¹⁵ confirming that a single nanocrystal can excite only a limited number of Er ions. In fact, in Chapter 7 we measured both the Er excitation rate at 1.536 μm and the nanocrystal excitation rate at 750 nm in a sample containing 1.8 at.% Er, and found that the Er excitation rate was a factor ~ 2 lower than the nanocrystal excitation rate. This proves that in the high Er concentration limit a single nanocrystal can excite only 1-2 Er ions. This

observation, together with the estimated nanocrystal concentration of 10^{19} cm^{-3} , implies that the maximum excitable Er concentration is approximately 0.02 at. %.

It is intriguing to note that the Er excitation rate in the low concentration limit is approximately a factor two higher than in the high concentration limit. This suggests that increasing the Er concentration either increases the number of excitable Er ions per nanocrystal from 1 to 2, or decreases the number of nanocrystals that can excite the same Er ion from 2 to 1.

The higher Er excitation rate at low concentration is also reflected in the pump power dependent Er luminescence intensity in Fig. 8.6. At high pump power, where the number of Er ions determines the luminescence intensity, the intensity from the high concentration sample is approximately 5 times higher than that from the low concentration sample. At low pump power, where the Er excitation rate is the limiting factor for the intensity, the intensity from the low concentration sample is relatively higher by a factor ~ 2.5 , as was expected from the higher excitation rate at low Er concentration.

8.3.6 Models describing the Er concentration limit

The existence of an upper limit to the amount of excitable Er could indicate that there is a limit to the amount of *optically active* Er that can be incorporated in this material. This may for example be caused by Er clustering or ErSi_2 formation at the Si/SiO₂ interface, which would prevent the Er from being in the 3+ valence state. However, measurements on Er and Si nanocrystal doped waveguides that are presented in Chapter 9 show a strong Er^{3+} related absorption, suggesting that a large fraction of the Er is in the optically active state.

Alternatively, the observed concentration limit could be an intrinsic property of the excitation process. The amount of excitable Er will be low when the effective Er excitation efficiency is influenced by the presence of *excited* Er. Such a situation arises when the formation of an exciton near an excited Er ion immediately leads to: (a) *Auger de-excitation*, in which the already excited Er ion transfers its energy to the generated exciton (Fig. 8.8(a)). This process has been shown to occur in Er doped bulk Si.¹⁶ After such Auger de-excitation the exciton can relax and subsequently excite an Er ion, effectively bringing the system back to the situation before the exciton was formed; or (b) *pair induced quenching*: at sufficiently high Er concentration, two excited Er ions can interact yielding one Er ion in the $^4I_{9/2}$ state, which rapidly decays to the first excited state, and one Er ion in the ground state (Fig. 8.8(b)). This co-operative upconversion effect usually produces a shortening of the Er decay rate at high pump power, which has not been observed. However, if the Er-Er coupling is sufficiently strong, no effect on the lifetime is seen. This special case is usually called pair induced quenching.

An interesting point to note is that both these processes reduce the internal quantum efficiency at high excitation rates. Figure 8.7 showed that at 1 mW pump power, the Er excitation rate is relatively large at low Er concentrations.

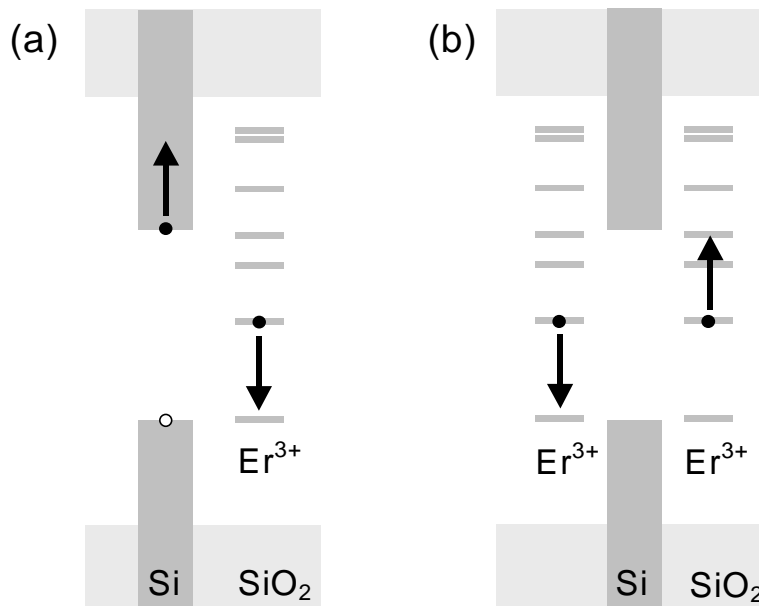


Figure 8.8. Schematic band diagram of Er and Si nanocrystal doped SiO₂ showing the process of (a) Auger de-excitation, and (b) pair-induced quenching. These processes can account for the observed Er concentration limit in Si nanocrystal doped SiO₂. Note that the Er energy levels represent collective states of the Er³⁺ 4f electrons, which are in fact well below the SiO₂ valence band edge.

Consequently, the internal quantum efficiency is expected to be relatively low at low Er concentration, which is indeed observed in Fig. 8.3.

8.3.7 The Er local environment

The maximum Er luminescence lifetime in these Si nanocrystal doped SiO₂ films is approximately 2 ms, corresponding to a decay rate of 500 s⁻¹. This decay rate is much higher than the radiative decay rate in pure SiO₂, which is ~50 s⁻¹.¹⁷ The relatively fast decay can be caused by two effects, namely by additional non-radiative decay (W_{nr}) or by an increased radiative decay rate (W_r). We will now discuss the influence of these two effects in our samples. From the measurements in Fig. 8.3 we find that the Er luminescence efficiency given by $\eta_{1.54} = W_r/(W_r+W_{nr})$ is less than 18% (see section 8.3.2). Since we know that the total decay rate W_r+W_{nr} is 500 s⁻¹ (Fig. 8.7), we estimate that the Er radiative decay rate $W_r < 90$ s⁻¹. In fact, we expect the radiative decay rate to be higher than the value of 50 s⁻¹ in bulk SiO₂ because of the presence of the Si substrate. If an ion is placed sufficiently close to a region with a high refractive index, its radiative decay rate increases due to an

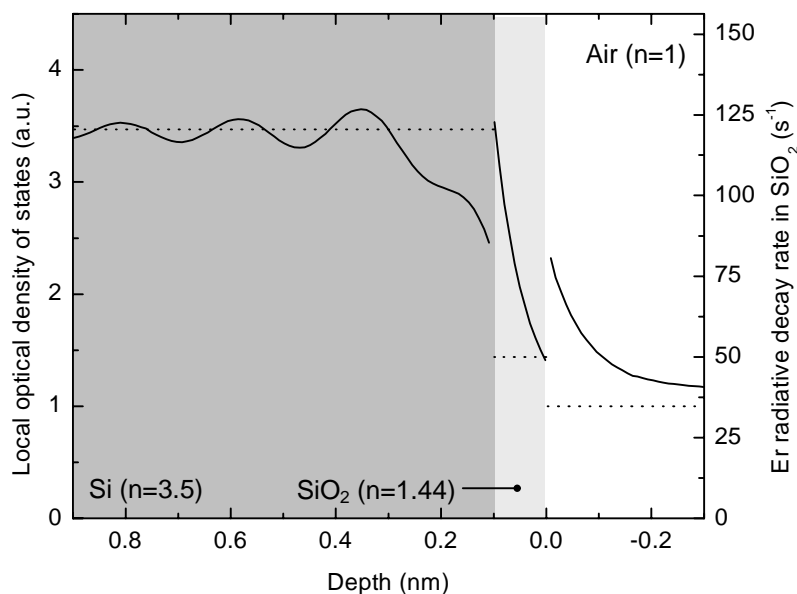


Figure 8.9. Local optical density of states (LDOS) relative to the LDOS in vacuum, calculated at a wavelength of $1.54 \mu\text{m}$. The dotted lines indicate the corresponding bulk value. The right hand axis indicates the Er radiative decay rate in the SiO_2 layer, assuming a bulk radiative lifetime of 20 ms .¹⁷

increase of the local optical density of states (LDOS).^{18,19} Figure 8.9 shows the calculated LDOS as a function of depth, relative to the value in vacuum for a wavelength of $1.54 \mu\text{m}$. Also indicated is the Er radiative decay rate in the SiO_2 , assuming a radiative lifetime in bulk SiO_2 of 50 s^{-1} . The calculation shows that W_r increases smoothly from 50 s^{-1} at the sample surface to 120 s^{-1} near the SiO_2/Si interface. This corresponds quite well with the radiative decay rate $W_r < 90 \text{ s}^{-1}$ obtained from our experiments. The fact that the observed decay rates can be described using the radiative lifetime in SiO_2 suggests that the excitable Er ions are not located inside the Si nanocrystals, but in an SiO_2 -like environment near the nanocrystals.

8.3.8 Device implications

In section 8.3.5 it was found that the effective Er absorption cross section σ_{eff} at 458 nm is approximately 10^{-15} cm^2 . This large cross section could be used in Er doped waveguide lasers and amplifiers, in which population inversion is reached at low pump power. It is important to mention here that although all luminescence measurements in this chapter were performed at 15 K , we have shown in Chapter 7 that the effective Er cross section is temperature independent up to at least 300 K .

In a Si nanocrystal sensitized optical amplifier based on the material studied here, the Er concentration should be kept low, since we have shown that only $\sim 0.02 \text{ at.}\%$ Er can be simultaneously kept in the excited state (see section 8.3.5). At higher

Er concentrations a large fraction of the Er will be in the ground state due to the processes discussed in section 8.3.6, which will result in significant losses at 1.54 μm . The maximum gain per unit length g_{max} that can be achieved in a waveguide amplifier is given by $g_{max}(\text{dB/cm})=4.34\times\sigma_{em}\times N_{Er}$ with N_{Er} the Er concentration and σ_{em} the emission cross section at 1.54 μm . Taking a typical value²⁰ $\sigma_{em}=7\times 10^{-21}$ cm^2 and the maximum Er concentration (2×10^{19} Er/cm^3) we find a maximum gain of 0.6 dB/cm.

In order to achieve net amplification at 1.54 μm , the Er induced gain should overcome the intrinsic device losses, including background absorption, scattering losses, and free carrier absorption. The latter process deserves special attention, because the presence of electron-hole pairs in the amplification medium is *required* for the Er excitation process. In free carrier absorption, free electrons and holes are excited higher in their respective energy bands by incoming photons. This process can occur at sub-bandgap energies, and can therefore affect the 1.54 μm transmission.

In bulk silicon, free carrier absorption cross sections at 1.54 μm are on the order of 10^{-17} cm^2 ,²¹ which is $\sim 10^4$ times larger than the cross section for stimulated emission of Er at 1.54 μm . Consequently, the exciton concentration in an Er doped optical amplifier should be at least a factor 10^4 lower than the excited Er concentration. This means that at a typical nanocrystal pump rate of 10^3 s^{-1} , the exciton lifetime should be well below 0.1 μs . The achievement of net optical gain thus requires that the Er excitation and the non-radiative processes listed in section 8.3.6 occur within 0.1 μs , which appears well possible. Furthermore, the concentration of nanocrystals *not* coupled to Er should be kept low, since they show room temperature exciton lifetimes > 10 μs . The above shows that the achievement of optical gain requires careful optimization of the Er distribution. If the Er concentration is too low, some nanocrystals will not be coupled to Er, and these will induce free carrier absorption. If the Er concentration is too high, part of the Er cannot be excited, which will introduce loss at 1.54 μm . These narrow concentration limits suggest that stochastic methods for Er incorporation, such as ion implantation and sputtering, are not desirable. A more promising method would be chemical synthesis, in which the number of Er ions per nanocrystal can be accurately tuned.

In order to investigate the processes of optical gain and free carrier absorption in Er and Si nanocrystal doped SiO₂, we have fabricated optical waveguides using Si nanocrystal doped SiO₂ as the guiding medium. Measurements on these samples are presented in Chapter 9.

8.4 Conclusions

We have shown that the maximum amount of Er that can be excited via exciton recombination in Si nanocrystals is ~ 1 Er ion per nanocrystal, corresponding to ~ 0.02 at.% Er. This observation can be explained by two different mechanisms occurring at high pump power, namely *Auger de-excitation* and *pair induced*

quenching. The luminescent Er ions are most likely located in an SiO₂-like environment near the Si nanocrystals, and have a luminescence efficiency $\eta_{1.54} < 18\%$. Using the obtained parameters, we can predict a maximum optical gain of 0.6 dB/cm at 1.54 μm for a Si nanocrystal sensitized Er doped waveguide amplifier in SiO₂, provided that free carrier absorption can be suppressed.

References

- ¹ S. Lombardo, S. U. Campisano, G. N. van den Hoven, A. Cacciato, and A. Polman, *Appl. Phys. Lett.* **63**, 1942 (1993)
- ² G. N. van den Hoven, J. H. Shin, A. Polman, S. Lombardo, and S. U. Campisano, *J. Appl. Phys.* **78**, 2642 (1995)
- ³ T. Kimura, A. Yokoi, H. Horiguchi, R. Saito, T. Ikoma, and A. Sato, *Appl. Phys. Lett.* **65**, 983 (1994)
- ⁴ J. H. Shin, G. N. van den Hoven, and A. Polman, *Appl. Phys. Lett.* **66**, 2379 (1995)
- ⁵ M. Fujii, M. Yoshida, Y. Kanzawa, S. Hayashi, and K. Yamamoto, *Appl. Phys. Lett.* **71**, 1198 (1997)
- ⁶ M. Fujii, M. Yoshida, S. Hayashi, and K. Yamamoto, *J. Appl. Phys.* **84**, 4525 (1998)
- ⁷ J. St. John, J. L. Coffey, Y. Chen, and R. F. Pinizzotto, *J. Am. Chem. Soc.* **121**, 1888 (1998)
- ⁸ C. E. Chryssou, A. J. Kenyon, T. S. Iwayama, C. W. Pitt, and D. E. Hole, *Appl. Phys. Lett.* **75**, 2011 (1999)
- ⁹ G. Franzò, V. Vinciguerra, and F. Priolo, *Appl. Phys. A* **69**, 3 (1999)
- ¹⁰ M. L. Brongersma, A. Polman, K. S. Min, E. Boer, T. Tambo, and H. A. Atwater, *Appl. Phys. Lett.* **72**, 2577 (1998)
- ¹¹ C. Delerue, G. Allan, and M. Lannoo, *Phys. Rev. B* **48**, 11024 (1993)
- ¹² M. L. Brongersma, A. Polman, K. S. Min, and H. A. Atwater, *J. Appl. Phys.* **86**, 759 (1999)
- ¹³ W. J. Miniscalco, *J. Lightwave Technol.* **9**, 234 (1991)
- ¹⁴ F. Auzel, in *Radiationless processes*, B. DiBartolo, Ed. (Plenum Press, New York, 1980)
- ¹⁵ D. Kovalev, J. Diener, H. Heckler, G. Polisski, N. Künzner, and F. Koch, *Phys. Rev. B* **61**, 4485 (2000)
- ¹⁶ F. Priolo, G. Franzò, S. Coffa, and A. Carnera, *Phys. Rev. B* **57**, 4443 (1998)
- ¹⁷ L. H. Slooff, M. J. A. de Dood, A. van Blaaderen, and A. Polman, *Appl. Phys. Lett.* **76**, 3682 (2000)
- ¹⁸ H. P. Urbach and G. L. J. A. Rikken, *Phys. Rev. A* **57**, 3913 (1998)
- ¹⁹ E. Snoeks, A. Lagendijk, and A. Polman, *Phys. Rev. Lett.* **74**, 2459 (1995)
- ²⁰ W. J. Miniscalco, *J. Lightwave Technol.* **9**, 234 (1991)
- ²¹ M. A. Green, *Silicon solar cells* (University of New South Wales, Sydney, 1995)

Chapter 9

Gain limiting processes in Er doped Si nanocrystal waveguides in SiO₂

Erbium doped Si nanocrystal based optical waveguides were formed by Er and Si ion implantation into SiO₂. Optical images of the waveguide output facet show a single, well confined optical mode. Transmission measurements reveal a clear Er related absorption of 2.7 dB/cm at 1.532 μm . The Er absorption cross section at 1.532 μm in Si nanocrystal doped SiO₂ is found to be $8 \times 10^{-20} \text{ cm}^2$. Upon optical excitation of the Si nanocrystals at 458 nm, the waveguides emit guided Er photoluminescence. No pump induced change of the Er related absorption was observed. Instead, optical pumping is shown to introduce a broad absorption in the near infrared, which is attributed to trap assisted free carrier absorption in the Si nanocrystal doped oxide layer. It is concluded that an Er doped Si nanocrystal sensitized optical amplifier will show optical gain if the Er concentration is kept below ~ 1 Er ion per nanocrystal, and if the applied pump power is kept low to avoid free carrier absorption.

9.1 Introduction

The rare earth ion Er³⁺ is widely used for optical amplification. The transition from the first excited state (⁴I_{13/2}) to the ground state (⁴I_{15/2}) within the Er 4f shell occurs around 1.53 μm , which is one of the standard wavelengths in optical telecommunication. To achieve the population inversion required for optical amplification, rather large pump powers are needed, because of the small absorption cross sections¹ ($\sim 10^{-21} \text{ cm}^2$) of the intra-4f transitions. This problem can be solved by adding a sensitizer that more efficiently absorbs pump light and subsequently transfers the absorbed energy to the Er³⁺ ion. As we have shown in Chapters 7 and 8, silicon nanocrystals can serve as an efficient sensitizer for Er. Optically generated excitons inside the nanocrystals can recombine and transfer energy to Er

at a rate $> 10^6 \text{ s}^{-1}$ and an efficiency of at least 60%. Due to the broad absorption bands of Si nanocrystals the sensitization scheme would allow for optical pumping of Er doped amplifiers using a broadband light source. In addition, electrical pumping of the Er may be possible.

Although the principle of Er excitation using Si nanocrystals has been shown, there have been no convincing demonstrations of optical gain using this excitation scheme. To study the gain perspective of this new type of waveguide material, we have performed transmission measurements on a highly Er doped optical waveguide in Si nanocrystal doped SiO_2 that shows excellent mode confinement. We observe no change in the Er related optical absorption upon intense optical excitation of the Si nanocrystals. This finding confirms the results presented in Chapters 7 and 8, which indicated the existence of an upper limit of ~ 1 Er ion that can be excited by a single nanocrystal. At very high pump power, the optical pumping of the Si nanocrystal doped SiO_2 waveguides is shown to generate a broad absorption in the infrared, which is attributed to trap assisted free carrier absorption in the Si nanocrystals.

9.2 Experiment

Silicon ions were implanted at 165 keV to a fluence of $1.7 \times 10^{17} \text{ cm}^{-2}$ into a $5 \mu\text{m}$ thick layer of SiO_2 that was grown by wet thermal oxidation of Si(100). The material was annealed at $1100 \text{ }^\circ\text{C}$ for 10 min. in flowing Ar in order to induce nucleation and growth of Si nanocrystals. The temperature of $1100 \text{ }^\circ\text{C}$ was found to yield maximum nanocrystal luminescence. Part of the sample was implanted with Er at 700 keV to a fluence of $1.2 \times 10^{16} \text{ cm}^{-2}$ and annealed at $1000 \text{ }^\circ\text{C}$ for 10 min. in flowing Ar to remove implantation induced damage. The samples were then annealed at $800 \text{ }^\circ\text{C}$ for 10 min. in forming gas ($\text{H}_2:\text{N}_2$ at 1:9) to optimize the nanocrystal and Er photoluminescence intensity.

The Er and Si concentration profiles were determined using Rutherford backscattering spectrometry (RBS). The results are shown in Fig. 9.1(a). The excess Si concentration profile peaks at a depth of 240 nm, and has a full width at half maximum (FWHM) of 160 nm. The Si peak concentration is 42 at.%, corresponding to an excess Si concentration of 13 at.%. Assuming an average nanocrystal diameter of 3 nm ,² the nanocrystal concentration at the peak of the Si profile is estimated to be $1.3 \times 10^{19} \text{ cm}^{-3}$. The Er concentration profile peaks at a depth of 240 nm, with an Er peak concentration of 1.3 at.% and a FWHM of 130 nm.

A series of $3.5 \mu\text{m}$ wide ridge waveguides was formed in the implanted and annealed SiO_2 film using standard photolithography and Ar beam etching to a depth of $0.5 \mu\text{m}$, i.e. well beyond the Si doped region. The excess Si inside the ridges locally raises the index of refraction, providing the index contrast required for optical mode confinement. To reduce scattering losses, the waveguides were covered with a $1.25 \mu\text{m}$ thick SiO_2 cladding layer using microwave sputtering. The samples were subsequently cut to a length of 8 mm, and the waveguide input and

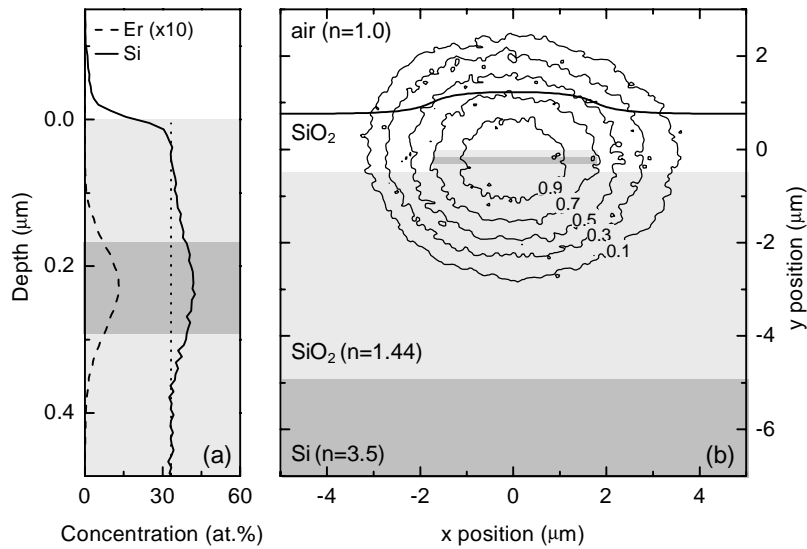


Figure 9.1. (a) Er and Si concentration profiles in an ion implanted planar waveguide sample as determined by RBS. (b) Optical mode image at a wavelength of 1.48 μm taken at the output facet of an Er doped Si nanocrystal based ridge waveguide. The contour lines indicate constant intensity. A sketch of the waveguide structure is included.

output facets were mechanically polished. A sketch of the final structure is drawn in Fig. 9.1(b), where $y=0$ corresponds to the position of the SiO₂ surface before the etching process. The light grey area represents the remaining SiO₂ after etching of the ridge, and the location of the implanted Er and Si is indicated by the dark grey line at $y=0.24 \mu\text{m}$. The smooth solid line at $y\approx 1 \mu\text{m}$ corresponds to the sample surface after deposition of the SiO₂ cladding layer.

Optical transmission measurements were performed using a fiber-coupled white light source emitting in the 1000-1800 nm range, which was modulated *on-off* at 270 Hz for lock-in detection. The white light was butt-coupled to the nanocrystal waveguides using a single mode tapered fiber. The transmitted light was collected by imaging the waveguide output facet onto a multimode fiber using a 10 \times microscope objective. A reference spectrum was obtained by directly imaging the light emitted from the input fiber. The collected light was led to a grating monochromator and detected using a liquid nitrogen cooled Ge detector, in combination with standard lock-in techniques. Optical mode images were obtained by coupling 1.49 μm light from an InGaAsP diode laser into the waveguide, and imaging the waveguide output facet on an infrared camera using a 10 \times microscope objective.

For photoluminescence (PL) measurements, the Si nanocrystal and Er doped waveguides were optically pumped using the 458 nm line of an Ar laser, which was mechanically chopped at a frequency of 18 Hz. The pump light was projected onto

the waveguides from the top using a cylindrical lens. The elongated spot was aligned with the waveguide, and covered the full waveguide length (see inset in Fig. 9.3). In this way the pump power can be evenly distributed over the full length of the waveguide. Despite the small thickness of the nanocrystal doped layer a significant fraction of the pump power (~5%) can be absorbed, because of the large nanocrystal absorption cross section at this wavelength. The guided photoluminescence signal was collected from the output facet as in the transmission measurements. Gain measurements were performed by measuring transmission spectra around 1.5 μm at different constant pump powers.

9.3 Results and discussion

Figure 9.1(b) shows iso-intensity contours of the optical mode image of 1.49 μm laser light guided in one of the waveguides. At this wavelength the waveguide only supports a single mode. The mode is slightly elliptical, with a FWHM of 3.8 μm in the x -direction, and 3.1 μm in the y -direction. Due to the small dimensions of the Er doped core region in this particular sample structure, the Er related absorption and gain will be lower than in a homogeneously doped waveguide. In fact, the effective overlap Γ of the optical mode with the Er profile is only 1%. This low value can be easily increased by changing the size of the nanocrystal doped core by performing multiple Er and Si implants or by depositing a layer of Er and Si doped SiO_2 , e.g. using sputter deposition³ or chemical vapor deposition.⁴

Figure 9.2(a) shows normalized transmission spectra of Si nanocrystal waveguides containing no Er (dotted line) and 1.3 at.% Er (solid line). A clear absorption line is observed around 1.53 μm , due to the ${}^4\text{I}_{15/2} \rightarrow {}^4\text{I}_{13/2}$ absorption of Er^{3+} . The overall transmission in the Er doped sample is a factor ~2.4 lower than in the undoped sample, which is possibly related to changes in the etching process, or to surface contamination. The transmitted intensity in Fig. 9.2(a) is given by

$$I = I_0 \times \eta \times e^{-(\alpha_{WG} + \sigma_{Er} N_{Er} \Gamma)L} \quad (1)$$

with $I_0(\lambda)$ the spectral distribution of the intensity in the incoming fiber, $\eta(\lambda)$ a function that contains the wavelength dependent coupling and collection efficiencies, $\alpha_{WG}(\lambda)$ the waveguide loss including scattering, $\sigma_{Er}(\lambda)$ the Er absorption cross section, $N_{Er} = 8.2 \times 10^{20} \text{ cm}^{-3}$ the Er^{3+} peak concentration, and $L=0.8 \text{ cm}$ the waveguide length. From Eq. 1 it follows that we can obtain the Er related absorption by dividing the normalized curves in Fig. 9.2(a). The thus obtained Er related absorption is shown in Fig. 9.2(b) (solid line). The peak absorption at 1.532 μm is found to be 2.7 dB/cm. From this value we can obtain the Er absorption cross section, using Eq. 1 and the measured values for Γ and N_{Er} . Assuming all Er is in the optically active 3+ valence state, we find that $\sigma_{Er}(1.532 \text{ } \mu\text{m}) = 8 \times 10^{-20} \text{ cm}^2$. This value is rather large compared to values found in

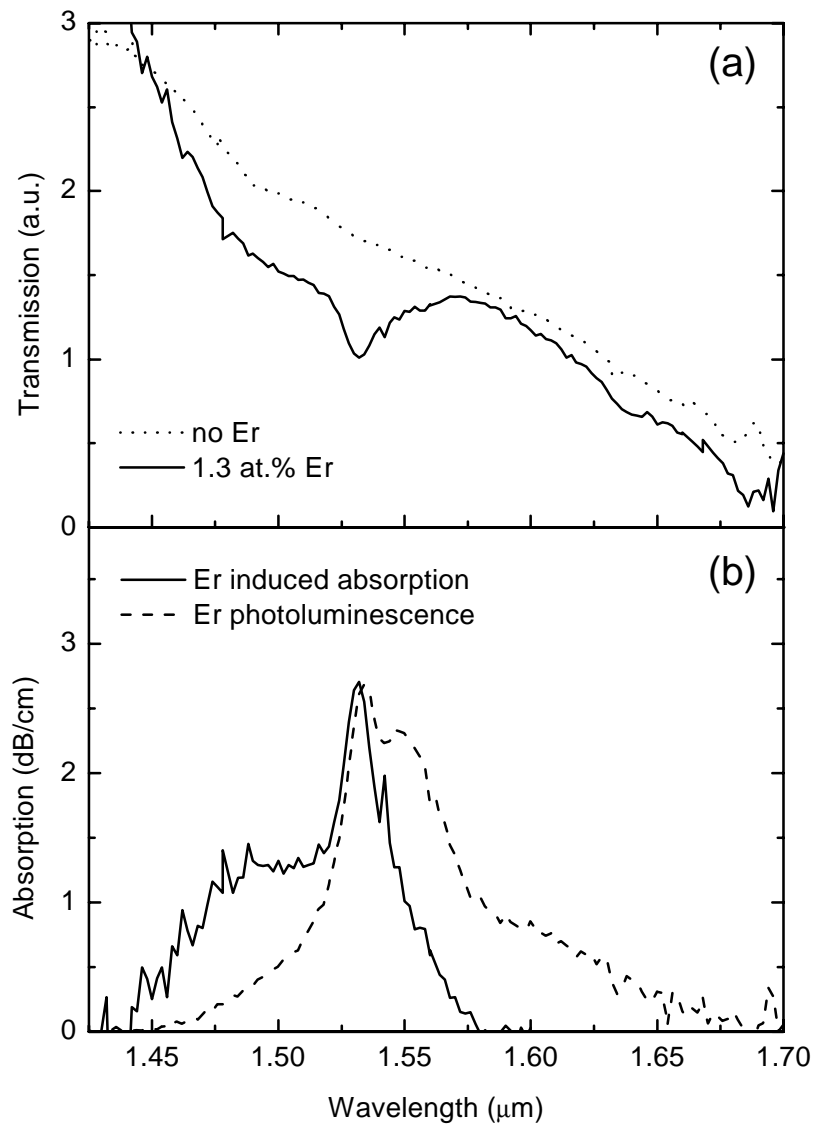


Figure 9.2. (a) Normalized transmission spectra of Si nanocrystal based waveguides containing no Er (dotted line) and 1.3 at.% Er (solid line) (b) Er related absorption spectrum (solid line) derived from the data in (a) and Er photoluminescence spectrum (dashed line) collected at the waveguide output facet (pump power 180 mW at 458 nm).

Er doped Si and SiO₂ based materials,¹ which are typically 10^{-21} - 10^{-20} cm². The large cross section may be due to the strong asymmetry of the local dielectric environment of the excitable Er³⁺ ions. This may also explain the relatively short luminescence lifetimes typically observed in this type of material.

When optically excited at 458 nm (normal incidence) the waveguides show guided Er PL that can be collected at the output facet. The spectral shape was found to be independent of the applied pump power. Figure 9.2(b) shows a PL spectrum

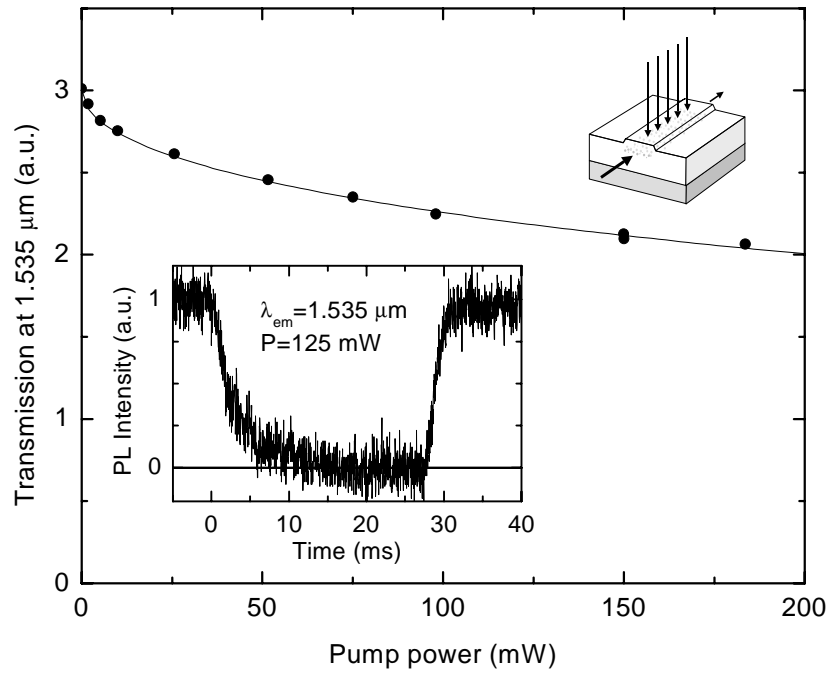


Figure 9.3. Waveguide transmission at 1.535 μm as a function of the applied continuous-wave 458 nm pump power. A sketch of the measurement configuration is included. The inset shows the time-dependent photoluminescence signal at 1.535 μm collected at the output facet during pump modulation.

taken at a pump power of 180 mW (dashed line). To determine the Er excitation rate $R_{Er} = (\tau_{rise}^{-1}) - (\tau_{decay}^{-1})$, the PL rise time τ_{rise} and decay time τ_{decay} at 1.535 μm were measured at different pump powers (see inset in Fig. 9.3). At all pump powers, τ_{decay} was found to be 3.6 ms, while τ_{rise} was system response limited, and was found to be 1.2 ms at all applied pump powers. From these data it follows that at the lowest applied pump power (25 mW) the Er excitation rate R_{Er} is at least 570 s^{-1} , which is sufficient to keep 70% of the excitable Er in the first excited state.

Transmission measurements were performed at different 458 nm pump powers up to 250 mW. Because of the high Er excitation rate, these pump powers are expected to reduce the Er related absorption at 1.53 μm . However, no change in the Er related absorption could be detected within the measurement accuracy. This puts an upper limit to the amount of Er in the waveguide that is excited via Si nanocrystals. From the experimentally obtained values for σ_{Er} and Γ , and the known noise in our transmission spectra of 1% we conclude that the concentration of excitable Er in the Si nanocrystal doped region is less than $3 \times 10^{19} \text{ cm}^{-3}$, which is close to the estimated nanocrystal peak concentration of $1.3 \times 10^{19} \text{ cm}^{-3}$ in our samples. This provides strong support for our finding in Chapters 7 and 8 that the amount of excitable Er in Si nanocrystal doped SiO_2 is limited to ~ 1 Er ion per

nanocrystal. Any Er in excess of this limit cannot be excited and will introduce an unbleachable absorption at 1.53 μm . Note that the peak Er concentration in the waveguides was $8.2 \times 10^{20} \text{ cm}^{-3}$.

Although no change in the Er related absorption is observed, the overall transmission of the waveguides is found to be reduced during optical pumping. Figure 9.3 shows the transmitted signal at 1.535 μm as a function of applied pump power at 458 nm. The same transmission decrease was observed at all wavelengths in the range 1.4-1.7 μm . The data points were measured after steady state was reached, and the input and output fiber position were re-optimized at each pump power to exclude effects related to changes in the coupling or collection efficiency. Apparently optical pumping at 458 nm induces an absorption in the waveguide material. After pump switch-off, the transmission converges to its original value over a period of several minutes. The time dependence of the absorption coefficient after pump switch-off (not shown) is strongly non-single exponential.

The observed transmission change could be related to free carrier absorption, a well known effect in bulk silicon, in which free carriers absorb sub-bandgap radiation due to intra-band transitions.⁵ The transmission change cannot be due to absorption by quantum confined electron-hole pairs, since these recombine at a rate $>10^5 \text{ s}^{-1}$ at room temperature.^{6,7} However, if the charge carriers are physically separated, their lifetime can increase by orders of magnitude. Such separation can occur when optical excitation leads to the ejection of a carrier into a deep trap state near the nanocrystal surface. This nanocrystal photo-ionization process is also thought to be responsible for the observed 'blinking' of luminescent nanocrystals.⁸ In this case, the lifetime of the free carrier and the induced absorption is determined by the time it takes the trapped carrier to tunnel back into the nanocrystal, which can indeed be on the order of minutes.⁹ Note that the pump induced absorption only becomes significant at pump powers $> 10 \text{ mW}$. As shown in Chapter 8 a significant Er excitation rate can already be achieved at a pump intensity of $\sim 5 \text{ mW/mm}^2$, corresponding to an incident pump power of only 0.4 mW on the 8 mm long waveguide.

9.4 Conclusions

Er doped Si nanocrystal based waveguides were fabricated in SiO₂. The waveguides support a single mode at 1.49 μm , and show a clear Er related absorption of 2.7 dB/cm at 1.532 μm . The Er absorption cross section is found to be $8 \times 10^{-20} \text{ cm}^2$. Gain measurements were performed using 458 nm pump light. No change of the Er related absorption is observed, which is consistent with a model in which a single nanocrystal can only excite ~ 1 Er ion. The optical pumping introduces a broad optical absorption in the near-infrared, which is attributed to free carrier absorption occurring inside charged nanocrystals. For the low pump powers typically required to achieve inversion in these nanocrystal sensitized waveguides, free carrier absorption is only a minor effect. Erbium doped Si nanocrystal sensitized optical

amplifiers will show net gain if the pump power required to achieve inversion is low, and if the Er concentration is kept below ~ 1 Er ion per nanocrystal. Optimum gain is expected in a waveguide with a large density of small nanocrystals, each coupled to ~ 1 Er ion.

References

- ¹ W. J. Miniscalco, J. Lightwave Technol. **9**, 234 (1991)
- ² K. S. Min, K. V. Shcheglov, C. M. Yang, H. A. Atwater, M. L. Brongersma, and A. Polman, Appl. Phys. Lett. **69**, 2033 (1996)
- ³ M. Fujii, M. Yoshida, S. Hayashi, and K. Yamamoto, J. Appl. Phys. **84**, 4525 (1998)
- ⁴ G. Franzò, D. Pacifici, V. Vinciguerra, F. Priolo, and F. Iacona, Appl. Phys. Lett. **76**, 2167 (2000)
- ⁵ W. Spitzer and H.Y. Fa, Phys. Rev. **108**, 268 (1957)
- ⁶ M. Hybertsen, Phys. Rev. Lett. **72**, 1514 (1994)
- ⁷ M.L. Brongersma, P.G. Kik, and A. Polman, Appl. Phys. Lett. **76**, 351 (2000)
- ⁸ M. Nirmal, B. O. Dabbousi, M.G. Bawendi, J.J. Macklin, J.K. Trautman, T.D. Harris, and L.E. Brus, Nature **383**, 802 (1996)
- ⁹ C. Svensson, in *The Si-SiO₂ system*, edited by P. Balk (Elsevier, 1988)

Summary

This thesis describes the energy transfer processes occurring in materials that can be used for the fabrication of silicon compatible optical integrated circuits, operating at 1.54 μm . Optical integrated circuits consist of several components such as lasers, multiplexers, modulators, splitters, amplifiers, and detectors, that are integrated on a single substrate. Combining optical functions on one chip could significantly reduce the size and cost of optical systems. The use of silicon as a basis for integrated optics is attractive, because the well developed silicon processing technology allows for the fabrication of sophisticated integrated circuits. In addition, it may enable the combined use of silicon electronics and optical data transmission within one opto-electronic integrated circuit.

Part I of this thesis discusses energy transfer in optical waveguide amplifiers on silicon. The waveguide amplifiers use an intra-4f transition of the rare earth ion erbium occurring at 1.54 μm . To achieve significant amplification at 1.54 μm on the short length scales available in an optical integrated circuit, high Er concentrations (10^{20} - 10^{21} cm^{-3}) are required. At these concentrations Er ions can interact, resulting in the occurrence of co-operative upconversion, an effect in which one excited Er ion is excited into a higher energy state, while a neighboring Er ion returns to the ground state. To counteract such effects, highly doped waveguide amplifiers operate at relatively high pump fluxes. This results in significant excited state absorption, i.e. absorption of pump photons by excited Er. These two effects, as well as several other parameters that are critical in the design of miniature optical waveguide amplifiers, are described in Chapter 2. A review of the most successful waveguide amplifiers and their characteristics is also presented. Chapter 3 describes measurements on Er doped Al_2O_3 waveguide amplifiers fabricated either by ion implantation or by $\text{Er}_2\text{O}_3/\text{Al}_2\text{O}_3$ co-sputtering. Although the Er concentration in the two waveguides is the same, the gain performance and photoluminescence behavior are completely different. This is attributed to a large difference in the upconversion coefficient, which is the result of a different atomic scale distribution of the Er ions. Miniature amplifiers show optimum gain performance if the Er is homogeneously distributed. This can be achieved using ion implantation.

Part II of this thesis discusses the energy transfer processes occurring in Er doped silicon. In Chapter 4 it is shown that Er in silicon can be excited by electron-hole pair recombination in an impurity-Auger effect. The thus excited luminescence at 1.54 μm is strongly quenched at temperatures above 100 K, mostly due to a non-radiative backtransfer process that quenches the Er transition itself, and partly due to a decrease in the Er excitation rate with increasing temperature. If the luminescence quenching could be reduced, e.g. by impurity co-doping, it would become possible to fabricate an electrically pumped Er doped waveguide amplifier. In Chapter 5 all rate constants, activation energies, and rate limiting steps in the Si:Er system are determined by fitting a rate equation model to three sets of

temperature dependent measurements. It is found that at temperatures above 100 K the backtransfer process generates a bound exciton in Si, which, if followed by exciton dissociation leads to the generation of electrical carriers that can be collected as a photocurrent. This process has an efficiency of 70% at room temperature. The backtransfer quenching process can therefore also be used in an advantageous way: it enables the fabrication of an Er doped photo-detector in a Si waveguide operating at 1.54 μm . In Chapter 6 it is shown that the performance of such a detector depends critically on the distribution of free carriers in the silicon waveguide, as they can cause unwanted optical absorption. It is shown that an infrared waveguide detector in Si based on an Er doped p - n junction can operate with an external quantum efficiency of 10^{-3} at room temperature, and suggestions for further improvement are given.

Part III of this thesis discusses the interaction between Er and silicon nanocrystals embedded in SiO_2 . Si nanocrystals efficiently absorb visible light, resulting in the generation of quantum confined electron-hole pairs. In Chapter 7 it is shown that the electron-hole pairs efficiently transfer energy to Er at a rate higher than 10^6 s^{-1} . No energy backtransfer is observed, due to the large mismatch between the nanocrystal bandgap energy and the Er transition energy. Due to the energy transfer, the effective Er absorption cross section is five orders of magnitude larger than for direct optical excitation. Silicon nanocrystals may thus be used to increase the pumping efficiency of an Er doped waveguide amplifier. In Chapter 8 it is shown that a single nanocrystal can excite only ~ 1 Er ion at a time and that an optical gain of 0.6 dB/cm may be achieved in a typical nanocrystal sensitized waveguide amplifier. Due to the broad absorption band of Si nanocrystals, a broad band light source can be used as pump source in such a nanocrystal sensitized Er doped waveguide amplifier. Transmission measurements on such a nanocrystal waveguide structure are presented in Chapter 9, and it is concluded that optical gain at 1.53 μm may be achieved in a 1 cm long nanocrystal doped waveguide amplifier at a pump power as low as 1 mW, provided that the Er concentration is kept below ~ 1 Er ion per nanocrystal.

Samenvatting

Vandaag de dag wordt meer en meer informatie verstuurd via internet. Het uitwisselen van muziek, foto's, programmatuur, wetenschappelijke artikelen en zelfs complete films wordt door steeds meer mensen gezien als een vanzelfsprekendheid. Door de ongeremde groei van het gebruik van internet neemt de belasting van telecommunicatie-netwerken sterk toe. Dit probleem wordt ondervangen door het gebruik van glasvezelverbindingen, waarmee informatie wordt overgedragen in de vorm van licht. Door de hoge frequentie van licht kunnen grote hoeveelheden informatie verzonden worden, tot boven de 10^{12} bits per seconde in één glasvezel.

Voor het benutten van deze techniek zijn diverse optische componenten nodig, zoals bijvoorbeeld lasers, detectoren, en lichtversterkers. Dit proefschrift beschrijft onderzoek naar materialen die gebruikt kunnen worden in geïntegreerde optische schakelingen voor licht met een golflengte van $1.5 \mu\text{m}$, een van de standaard golflengtes in de telecommunicatie. Daarbij is gekozen voor materialen die gebruikt kunnen worden in combinatie met silicium, het materiaal waaruit computer chips worden vervaardigd.

In deel I worden materialen besproken die kunnen worden gebruikt voor het versterken van licht. Dit kan worden bereikt door optisch actieve erbium (Er) ionen op te lossen in lichtgeleiders die gemaakt zijn van aluminium oxide. Erbium ionen kunnen in een aangeslagen toestand gebracht worden door ze optisch te 'pompen' met een laser. Het aangeslagen erbium kan vervolgens licht uitzenden met een golflengte van $1.54 \mu\text{m}$. Deze emissie wordt gebruikt voor lichtversterking. In hoofdstuk 2 worden alle parameters die van belang zijn voor het ontwerpen van miniatuur optische versterkers besproken. Ook wordt een overzicht gegeven van de tot op heden vervaardigde versterkers.

Om een zo groot mogelijke versterking te behalen, is het belangrijk om zoveel mogelijk erbium in de aangeslagen toestand te brengen. Wanneer de erbium concentratie te hoog is kunnen aangeslagen erbium ionen energie uitwisselen. In dit proces valt één erbium ion terug naar de grondtoestand, wat nadelig is voor de versterking. Om dit effect te minimaliseren is het essentieel dat de erbium ionen zo homogeen mogelijk over het materiaal verdeeld worden. Zoals in hoofdstuk 3 blijkt, is dit te realiseren met behulp van ionen implantatie. Een veel simpeler sputter proces leidt niet tot het gewenste resultaat.

In deel II wordt het oplossen van erbium in silicium bestudeerd. Silicium is een ideaal materiaal voor de fabricage van zeer kleine lichtsakelingen. In hoofdstuk 4 wordt aangetoond dat elektronen in silicium erbium kunnen aanslaan wanneer zij recombineren met gaten (onbezette elektron-toestanden). Dit effect zou kunnen worden gebruikt voor het vervaardigen van een elektrisch aangedreven lichtversterker in silicium. Helaas is dit proces alleen efficiënt bij temperaturen beneden de $-200 \text{ }^\circ\text{C}$. In Hoofdstuk 5 worden daarom alle processen die van belang zijn in de energie-overdracht tussen silicium en erbium in detail bestudeerd. Daarbij

blijkt zeer verrassend dat het omgekeerde proces ook mogelijk is: aangeslagen erbium kan energie overdragen aan silicium en een elektron vrij maken. Het rendement van dit proces is 70% bij 25 °C. Zo wordt het mogelijk in een silicium lichtgeleider een lichtdetector te maken die gevoelig is voor licht met een golflengte van 1.54 μm . In hoofdstuk 6 wordt een dergelijke detector beschreven, en berekeningen laten zien dat een rendement beter dan 10^{-3} haalbaar is.

Deel III focusteert op een samengesteld materiaal, dat eigenschappen van een isolerend materiaal (silicium oxide) en silicium combineert. In het silicium oxide worden met behulp van ionen implantatie silicium kristallen met een diameter van enkele nanometers (10^{-9} m) vervaardigd. Deze nanokristallen kunnen veel efficiënter licht absorberen dan erbium. In hoofdstukken 7 en 8 wordt aangetoond dat wanneer in dit materiaal materiaal erbium wordt opgelost, de nanokristallen efficiënt hun energie overdragen aan het erbium. Het omgekeerde proces, dat in puur silicium (deel II) het maken van een versterker bemoeilijkt, treedt in dit composiet materiaal niet op. Verder wordt aangetoond dat per nanokristal slechts één erbium ion kan worden aangeslagen, een belangrijk gegeven voor het realiseren van een lichtversterker. In hoofdstuk 9 wordt een lichtgeleider bestudeerd die gebaseerd is op dit materiaal. Het blijkt dat een dergelijke lichtversterker kan werken bij zeer lage pompvermogens, en dat voor het pompen een eenvoudige lichtbron gebruikt kan worden.

Dankwoord

Allereerst wil ik mijn promotor Albert Polman bedanken. Albert, je hebt van de afgelopen jaren een leuke en leerzame periode gemaakt. Ik heb veel profijt gehad van je kennis op het gebied van zowel het uitvoeren als het uitdragen van onderzoek. Op kritische momenten was je altijd bereid tot het uiterste te gaan, en met je grote besluitvaardigheid zorgde je ervoor dat de dingen steeds weer tot een goed einde gebracht werden.

Het werken in de opto-electronic materials groep is een geweldige ervaring geweest. Tijdens mijn stage op het Amolf heb ik veel geleerd van Edwin Snoeks en Gerlas van den Hoven, die met tomeloze energie de fysica bedreven, en Frans Saris, die altijd de kern van de zaak wist te raken. Uit die tijd wil ik ook Peter Stolk, Stefania Acco, Rosalía Serna, Bas Dorren, Liesbeth de Wit, Antonio Cacciato, Jung Shin, Henk Hopman, en Erik Radius bedanken voor een mooie tijd.

Tijdens mijn promotie heb ik vele goede momenten gehad met mijn groepsgenoten Mark Brongersma, Lenneke Slooff, Michiel de Dood, Christof Strohhöfer, Jan van der Elsken, Teun van Dillen, Freek Suyver, Dirk Vossen, Daniel Peters, Michaël Hensen, Mariëlle Ladevèze, Nicolas Hamelin, en José dos Santos. Daarnaast heb ik plezierig samengewerkt met Kostya Kikoin, Tadamasa Kimura, Salvo Coffa, Yingchao Yan, en Tom Gregorkiewicz. Mark wil ik speciaal bedanken voor alle heerlijke discussies over natuurkunde en de vele hilarische momenten die we hebben beleefd, zowel binnen als buiten het lab. Ook wil ik mijn labmaatje Astrid bedanken, die me in het laatste jaar van mijn promotie regelmatig het lab uit heeft gesleept om een partijtje te voetballen of te squashen. Ook wil ik hier graag alle Impuls redactieleden bedanken voor alle samenwerking, en vooral Henk Sodenkamp voor de mooie verhalen tijdens het drukken en afwerken van de Impuls.

Het werk dat beschreven staat in dit proefschrift zou niet mogelijk zijn geweest zonder de ondersteuning van vele mensen binnen en buiten het Amolf. Allereerst wil ik de groepstechnici Jan ter Beek en Johan Derks bedanken, die de meetapparatuur ondanks soms onorthodox gebruik in topconditie hebben weten te houden. Ook ben ik de mensen bij de Electronica en Informatica afdeling veel dank verschuldigd: Hans Alberda was mijn steun en toeverlaat bij het automatiseren van onze meetopstelling, Hans ter Horst was altijd bereid om zelfs de eenvoudigste schakelingen uit te leggen, Dennis Driessen en Richard Schaafsma hebben geholpen bij een onwaarschijnlijke Windows 95 transplantatie, en Ton Vijftigschild bouwde in no-time een stroomvoorversterker voor de metingen in Hoofdstuk 6. Koos van Uffelen van de TU Delft wil ik bedanken voor de prettige samenwerking en al het sputter- en etswerk aan de lichtgeleiders in Hoofdstukken 3 en 9, en René Koper van het *Surface Preparation Lab* voor het polijsten van diezelfde lichtgeleiders. Verder zou ik bij deze alle mensen binnen het Amolf willen bedanken die achter de schermen hebben gezorgd dat alles op rolletjes bleef lopen.

Naast een hoop kennis heb ik aan de afgelopen jaren ook een hoop leuke herinneringen overgehouden. De zomerschool *Silicon based microphotonics* aan het Como meer in Italië was ronduit fantastisch, en het beeld van Michiel die een steen van de bodem van het Como-meer probeert te tillen staat voor altijd in mijn geheugen gegrift. Ook aan het schrijven (en zingen!) van een slotlied voor de zomerschool met Lenneke denk ik nu al met weemoed terug. De metingen aan de detector waveguides met Salvo Coffa waren ontzettend spannend, en de aansluitende diners op een terrasje aan de Middenweg om half elf heerlijk. Behalve deze momenten zijn er nog talloze voorvallen die er allemaal voor zorgen dat ik met veel plezier aan mijn tijd op het Amolf terugdenk.

Als laatste wil ik hier mijn ouders bedanken voor de interesse die ze altijd hebben getoond en de steun die ze me de afgelopen jaren hebben gegeven.

Curriculum Vitae

Pieter Geert Kik werd geboren op 7 mei 1972 in "Openbaar Lichaam Zuidelijke IJsselmeerpolders", in wat later Lelystad zou heten. In 1990 behaalde hij *cum laude* het diploma Gymnasium β aan de Rijksscholengemeenschap West-Friesland in Hoorn. In datzelfde jaar begon hij met de studie Natuurkunde aan de Universiteit van Amsterdam. Na het behalen van zijn propaedeuse in 1991 studeerde hij naast natuurkunde één jaar hobo aan het Sweelinck Conservatorium in Amsterdam. In 1993 volgde hij een zes maanden durende stage in de groep van Prof. Dr. A. Polman aan het FOM Instituut voor Atoom- en Molecuulfysica in Amsterdam, waar hij de optische eigenschappen van Er gedoteerde silicaatglazen bestudeerde. Zijn afstudeerstage bracht hij door aan aan de Harvard Universiteit in Boston (USA) in de groep van Prof. F. Spaepen, waar hij onderzoek deed naar grensvlakspanningen in Cu-Ni multilagen. In 1995 studeerde hij af aan de Universiteit van Amsterdam met als specialisatie Technische Natuurkunde. Aansluitend begon hij zijn promotieonderzoek in de groep Opto-elektronische materialen van Prof. Dr. A. Polman aan het FOM Instituut voor Atoom- en Molecuulfysica. De resultaten van dit onderzoek staan beschreven in dit proefschrift.

List of publications

This thesis is based on the following articles:

- Chapter 2 *Erbium doped optical waveguide amplifiers on silicon*
P. G. Kik, and A. Polman
Mat. Res. Soc. Bull. **23**, 48 (1998)
- Chapter 3 *Co-operative upconversion as the gain limiting factor in ion implanted and co-sputtered Al₂O₃ optical waveguide amplifiers*
P. G. Kik, G. N. van den Hoven, A. Polman, J. W. M. van Uffelen, and M. K. Smit
In preparation for Appl. Opt.
- Chapter 4 *Excitation and de-excitation of Er³⁺ in crystalline silicon*
P. G. Kik, M. J. A. de Dood, K. Kikoin, and A. Polman
Appl. Phys. Lett. **70**, 1721 (1997)
- Incorporation, excitation, and de-excitation of erbium in crystal silicon*
M. J. A. de Dood, P. G. Kik, J. H. Shin, and A. Polman
Mat. Res. Soc. Symp. Proc. **422**, 219 (1996)
- Chapter 5 *Energy backtransfer and infrared photoresponse in erbium doped silicon p-n diodes*
N. Hamelin, P. G. Kik, and A. Polman,
J. Appl. Phys. **88**, in press (October 15, 2000)
- Infrared detector device of semiconductor material and manufacturing process thereof*
A. Polman, N. Hamelin, P. G. Kik, S. Coffa, M. Saggio, and F. Frisina
European Patent 98830592.6, US Patent 09/415,022
- Chapter 6 *Quantum efficiency of an Er doped waveguide detector in silicon operating at 1.54 μm*
P. G. Kik, S. Coffa, and A. Polman
In preparation for Appl. Phys. Lett.
- Chapter 7 *Strong exciton-erbium coupling in Si nanocrystal doped SiO₂*
P. G. Kik, M. L. Brongersma, and A. Polman
Appl. Phys. Lett. **76**, 2325 (2000)

- Chapter 8 *Exciton-erbium interactions in Si nanocrystal doped SiO₂*
P. G. Kik, and A. Polman
J. Appl. Phys. **88**, 1992 (2000)
- Chapter 9 *Gain limiting processes in Er doped Si nanocrystal waveguides in SiO₂*
P. G. Kik, and A. Polman
In preparation for Appl. Phys. Lett.

Articles to which the author also contributed:

Ion beam synthesis of planar opto-electronic devices

A. Polman, E. Snoeks, G. N. van den Hoven, M. L. Brongersma, R. Serna, J. H. Shin, P. G. Kik, and E. Radius
Nucl. Instrum. Meth. B **106**, 393 (1995)

Concentration quenching in erbium implanted alkali silicate glasses

E. Snoeks, P. G. Kik, and A. Polman
Opt. Mater. **5**, 159 (1996)

Erbium-doped phosphate glass waveguide on silicon with 4.1 dB/cm gain at 1.535 μm

Y. C. Yan, A. J. Faber, H. de Waal, P. G. Kik, and A. Polman
Appl. Phys. Lett. **71**, 2922 (1997)

Optical and electrical doping of silicon with holmium

J. F. Suyver, P. G. Kik, T. Kimura, A. Polman, G. Franzò, and S. Coffa
Nucl. Instrum. Meth. B **148**, 497 (1999)

Size-dependent electron-hole exchange interaction in Si nanocrystals

M. L. Brongersma, P. G. Kik, A. Polman, K. S. Min, and H. A. Atwater
Appl. Phys. Lett. **76**, 351 (2000)

Selective modification of the Er³⁺ ⁴I_{11/2} branching ratio by energy transfer to Eu³⁺

C. Strohhöfer, P. G. Kik, and A. Polman
J. Appl. Phys., in press (2000)

Pumping planar waveguide amplifiers using a coupled waveguide system

L. H. Slooff, P. G. Kik, A. Tip, and A. Polman
In preparation for J. Lightwave Technol.

Exciton-erbium energy transfer in Si nanocrystal-doped SiO₂

P. G. Kik, and A. Polman
Mat. Sc. Eng. B, in press (2000)